

PARAMETRIC INTERACTIONS OF SHORT OPTICAL PULSES  
IN QUASI-PHASE-MATCHED NONLINEAR DEVICES

A DISSERTATION  
SUBMITTED TO THE DEPARTMENT OF APPLIED PHYSICS  
AND THE COMMITTEE ON GRADUATE STUDIES  
OF STANFORD UNIVERSITY  
IN PARTIAL FULFILLMENT OF THE REQUIREMENTS  
FOR THE DEGREE OF  
DOCTOR OF PHILOSOPHY

Andrew Michael Schober

September 2005

© Copyright by Andrew Michael Schober 2005  
All Rights Reserved

I certify that I have read this dissertation and that, in my opinion, it is fully adequate in scope and quality as a dissertation for the degree of Doctor of Philosophy.

---

Martin M. Fejer Principal Adviser

I certify that I have read this dissertation and that, in my opinion, it is fully adequate in scope and quality as a dissertation for the degree of Doctor of Philosophy.

---

Robert L. Byer

I certify that I have read this dissertation and that, in my opinion, it is fully adequate in scope and quality as a dissertation for the degree of Doctor of Philosophy.

---

James S. Harris

Approved for the University Committee on Graduate Studies.



# Abstract

Broad applicability of ultrashort pulses has been demonstrated across many fields in science and technology. The short pulse duration enables the fastest known measurement techniques for chemical reactions and biological processes, as well as the delivery of communications data at ever increasing bit rates. Ultrashort pulses possess large bandwidths, useful in optical frequency metrology and optical coherence tomography. The high peak power available in ultrashort pulses enables athermal machining of metals and dielectrics, and has opened new doors to the study of physics in the presence of the largest-amplitude electric fields ever generated in a laboratory.

While the properties of short duration, broad bandwidth, and high peak power, make ultrashort pulses attractive for many applications, they pose unique challenges in the context of frequency conversion and amplification. This thesis addresses how quasi-phase-matching (QPM) technology is well suited to address these challenges through the engineering of devices by patterning nonlinear materials. QPM devices are shown to enable tunable control of the phase response of second-harmonic generation (SHG), engineering of broad-bandwidth SHG using spectral angular dispersion, and tailoring of spatial solitons that exist through nonlinear phase shifts present in cascaded frequency conversion.

In this dissertation, we show the tunable control of dispersion through lateral and longitudinal patterning of nonlinear materials in the 60-fold compression of pulses during SHG. We discuss both the conditioning of ultrashort pulses and the engineering of nonlinear devices for broadband frequency conversion with high conversion efficiency and low peak intensity using spectral angular dispersion in second-harmonic generation; including the optimization of conversion efficiency enabled by QPM technology.

We show the tailoring of multicolor spatial solitons through the use of chirped-period QPM gratings for enhanced conversion to signal and idler in an optical parametric amplifier. Additionally, we discuss the fundamental limitations to spatial soliton generation and propagation caused by the amplification of parametric noise, which is shown experimentally to affect both the spatial confinement and frequency content of multicolor solitons. Experiments are conducted using periodically-poled lithium niobate (PPLN), but all are generally applicable to any QPM material system.

# Acknowledgements

As much as I am proud of the body of work represented in this thesis, none of my endeavors would have been successful without the support of colleagues, friends, and family. I am continually amazed at how lucky I have been to be surrounded by wonderful people who have fostered an environment built for scientific discovery, personal growth, and simple enjoyment. Although this thesis focuses overwhelmingly on the first of these, the importance of the others cannot be overestimated.

Firstly, I must thank my advisor: Prof. Marty Fejer. Marty not only has an astounding breadth of knowledge on all things scientific, but also has an uncanny ability to ask the most pertinent question for those topics on the forefront of research. More important than his abilities (which are many and great) is his generosity with his time. Like most Stanford professors, Marty has many time commitments. It has not always been easy to find him, but once found, he makes himself incredibly available – day, evening, or weekend. I am very grateful for the opportunity to learn from his outstanding example, and for his advice and encouragement.

The Byer-Fejer Group has provided a fantastic environment in which to work. Prof. Byer's optimism is contagious, and his vision in pursuing very ambitious research projects (from LIGO to LISA to LEAP...) fuels the enthusiasm for discovery and innovation that makes research fun. Vivian Drew, and all the Byer-Fejer Group administrators who preceded her (Kellie Koucky, Tami Reynolds, Annie Tran...) are such essential and underappreciated parts of this research group; I fear things would fall apart without them. From the rest of the research staff (Roger Route, Norna Robertson, Brian Lantz, Konstantin Vodopyanov, and Shiela Rowan) through all the students, it's been a pleasure to work in this group.

I thank Prof. James Harris, with whom I started my graduate research in the growth of GaAs for quasi-phase-matching applications. Although I found myself more suited for device rather than materials development, I had a lot of fun and gained a great respect for those who solve materials problems. I also appreciate Prof. Harris's continued support and encouragement as he served on both my qualifying exam and thesis defense committees.

The Fejer students are a uniquely talented and generous group who have made work both productive and enjoyable. I should thank first Gena Imeshev, with whom I began my investigation into ultrafast nonlinear optics. He had a knack for extracting the essentials of complicated theoretical problems, and I am grateful for the time he spent helping to get me started. Xiuping Xie also deserves a special thanks, as his talent for numerical methods was invaluable in the development of beam propagation software used in the simulation of ultrafast problems without which much of this work would have been impossible. I have enjoyed many great discussions, on topics from science to sports, with all of my fellow Fejer students, including Loren Eyres, Krishnan Parameswaran, Gena Imeshev, Jonathan Kurz, Rosti Roussev, Xiuping Xie, Paulina Kuo, Mathieu Charbonneau-Lefort, Carsten Langrock, David Hum, Jie Huang, Joe Schaar, and Scott Sifferman. I could not have asked for better co-workers.

In addition to the students, staff, and researchers in our group, the Ginzton Laboratory contains a broader group of people who collectively form a scientific community with a worldwide reputation. While the research groups deserve much of the accolades for this reputation, the efforts of the Ginzton Lab staff are behind every successful experiment. Many thanks to the technical staff, including Tom Carver and Tim Brand; as well as the administrative staff who keeps things running smoothly, including Darla LeGrand-Sawyer, Jenny Kienitz, Rene Bulan, Amy Hornibrook, Pete Cruz, Mike Schlimmer, John Coggins, and especially Larry Randall and Fayden Holmboe.

Paula Perron in the Applied Physics Department office does an amazing job of keeping the students, faculty, and staff on course with all the University regulations, and we are incredibly lucky to have her and Claire Nicholas on top of things.

One of the perks of being in Marty Fejer's group is the extended network of connections he has in the professional community. Each of his students benefits from

his reputation and the relationships he has forged. Most important to my work has been Silvia Carrasco (formerly of Universitat Politecnica de Catalunya, Barcelona, Spain and currently at Harvard University) and her advisor Lluís Torner of Universitat Politecnica de Catalunya. Silvia is an expert in the theory of solitons in quasi-phase-matched nonlinear interactions, and I have called upon her expertise countless times in the course of my research. Working with Silvia was not only professionally productive and intellectually enlightening, but her pleasant outlook and positive disposition were particularly refreshing.

I am also grateful for the support of other collaborators who have joined me, in ways great and small, in the course of this research. Not all of these efforts have been successful; but without those willing to gamble on unproven technology, innovation cannot move forward. Many thanks to Almantas Galvanauskas (and his students) of the University of Michigan; Don Harter of IMRA America; Len Marabella, Rob Waarts and Jean-Philippe Fève of JDS Uniphase; and Bedros Afeyan of Polymath Research.

In addition to an outstanding group of colleagues and co-workers, I have been blessed in finding amazing friends. At the top of this list are Ueyn Block, Joe Matteo, and Mark Peterman – whom I met very soon after arriving at Stanford. In addition to being great study partners through our first years of coursework, these three have been better friends than I ever hoped to find. They have made these years so much fun and have provided a welcome distraction from life in the lab. I should especially thank Joe, with whom I spent countless hours in the gym getting stronger than I thought possible and having a blast doing it. Thanks to all my friends who have made these years fun, including Cliff Wall, Kyle Hammerick, Kusai Merchant, Roy Zeighami, Jesse Armiger, Big Joe Fairchild, Chuck Booten, Greg Shaver, Heather Harding, Chris and Jenny Deeb, and Jake and Jean Showalter.

The most important people in the world to me, and those to whom I owe the most gratitude, are my family. They are the most talented, caring, and fun group of people I have ever known. They have taught me to work hard, but not to take life too seriously; to be independent, but also to appreciate the support of others; and to be practical, but also unafraid of risk. Thank you to the Schober family: Mom, Dad,

Ed, Jim, Teresa, Pablo, Carlos, Jenn, Jason, John, Heather, Natalie, Will, and Jake. Thank you to the Hills (Carl, Vicki, Kate, and Jon), who have welcomed me into their family, and have been very supportive during the last two years of my graduate study. Thanks also to my Grandma and Grandpa Schober – who always took a special interest in the education of their grandchildren, and along with my parents, helped to make sure we were never limited in our opportunities. I especially remember my Grandpa, Edward Schober Sr., who passed away during my second year at Stanford.

Last, and most of all, I must thank my most supportive colleague, my best friend, and the closest member of my ever-growing family: my wife, Kelly. She came into my life at the lowest point in my graduate study, when progress in research seemed slowed to a stop and frustration was at its peak. Her enthusiasm for her own career as a reporter reminded me of what it is I love about science, and sparked newfound motivation and enthusiasm for my research. Through no coincidence, what followed were my most productive and happiest years at Stanford, if not in my entire life.

# Contents

<b>Abstract</b>	<b>v</b>
<b>Acknowledgements</b>	<b>vii</b>
<b>1 Introduction</b>	<b>1</b>
1.1 Motivation . . . . .	1
1.2 QPM Nonlinear Optical Frequency Conversion . . . . .	3
1.3 Frequency conversion of short pulses . . . . .	8
1.4 OPA of short pulses . . . . .	12
1.5 Overview . . . . .	15
<b>2 Theory of three-wave mixing in QPM materials</b>	<b>17</b>
2.1 Introduction . . . . .	17
2.2 The coupled wave equations . . . . .	18
2.3 Characteristic Length Scales . . . . .	20
2.4 Monochromatic, plane-wave SHG . . . . .	22
2.5 Monochromatic, plane-wave OPA . . . . .	23
2.6 QPM-SHG transfer function . . . . .	24
2.7 Solitons in three-wave mixing . . . . .	28
2.8 Summary of Chapter 2 . . . . .	34
<b>3 Tunable-chirp pulse compression in quasi-phase-matched second harmonic generation</b>	<b>35</b>
3.1 Introduction . . . . .	35

3.2	Tunable SHG pulse compression . . . . .	36
3.3	Experimental Results . . . . .	39
3.4	Summary of Chapter 3 . . . . .	43
<b>4</b>	<b>Group-velocity mismatch compensation in quasi-phase-matched second-harmonic generation of pulses with spectral angular dispersion</b>	<b>44</b>
4.1	Introduction . . . . .	44
4.2	Frequency domain description . . . . .	48
4.3	Time domain description . . . . .	50
4.4	Experiment . . . . .	52
4.5	Theoretical model . . . . .	57
4.6	General solutions . . . . .	64
4.7	Solution for a Gaussian FH field envelope . . . . .	66
4.8	Effects of GVD and walkoff . . . . .	71
4.9	Efficiency in the absence of walkoff and GVD . . . . .	76
4.10	Efficiency with walkoff and GVD . . . . .	78
4.11	Generalized three-wave description . . . . .	87
4.12	Summary of Chapter 4 . . . . .	92
<b>5</b>	<b>Engineering of multi-color spatial solitons with chirped-period quasi-phase-matching gratings in optical parametric amplification</b>	<b>94</b>
5.1	Introduction . . . . .	94
5.2	Efficient parametric amplification with solitons . . . . .	95
5.3	Experimental results . . . . .	97
5.4	Summary of Chapter 5 . . . . .	104
<b>6</b>	<b>Excitation of quadratic spatial solitons in the presence of parametric noise</b>	<b>105</b>
6.1	Introduction . . . . .	105
6.2	Noise in soliton OPA . . . . .	108
6.3	Noise in nonlinear interactions . . . . .	111
6.4	Experimental results . . . . .	115

6.5	Scaling with signal power . . . . .	124
6.6	Soliton propagation with noise . . . . .	126
6.7	Implications for soliton OPA . . . . .	132
6.8	Summary of Chapter 6 . . . . .	134
<b>7</b>	<b>Summary</b>	<b>137</b>
7.1	Summary of research contributions . . . . .	137
7.2	Future Directions . . . . .	140
	<b>Bibliography</b>	<b>142</b>

# List of Tables

2.1	Characteristic lengths in three-wave mixing. . . . .	21
4.1	Characteristic lengths in non-collinear SHG with spectral angular dispersion. . . . .	61
4.2	Comparison of techniques for ultrashort-pulse SHG: efficiency and effective area. . . . .	86

# List of Figures

1.1	SHG power growth versus distance. . . . .	5
1.2	Lithographic fabrication of periodically poled lithium niobate. . . . .	6
1.3	Non-uniform QPM patterns resulting from lithographic QPM fabrication. . . . .	7
1.4	Time-domain schematic of group-velocity mismatch in SHG. . . . .	8
1.5	Second-harmonic amplitude versus frequency detuning in a uniform nonlinear crystal. . . . .	9
1.6	Schematic diagram of the chirped-pulse optical parametric amplification technique for the amplification of ultrashort pulses. . . . .	13
1.7	Pump and Signal intensity envelopes in a saturated parametric amplifier. . . . .	14
2.1	SHG transfer function of a strongly chirped QPM grating. . . . .	26
2.2	Beam narrowing in nonlinear frequency conversion. . . . .	29
2.3	Three-wave soliton field envelopes for several different values of the normalized wavevector mismatch. . . . .	32
2.4	Fractional power of component waves in spatial solitons versus wavevector mismatch. . . . .	33
3.1	Diagram of fanned QPM-SHG pulse-compression grating. . . . .	38
3.2	Tuning behavior of fanned grating device. . . . .	40
3.3	Reconstructed electric field and autocorrelation from fanned grating device. . . . .	41
4.1	Frequency-domain picture of plane-wave non-collinear QPM-SHG . . . . .	48
4.2	Angular dispersion and pulse-front tilt resulting from grating diffraction . . . . .	50

4.3	Time-domain picture of tilted pulse-front SHG . . . . .	52
4.4	Schematic diagram of broadband QPM-SHG experiment . . . . .	53
4.5	Autocorrelation and spectrum of QPM-SHG with angular dispersion.	55
4.6	Diffraction of an optical pulse with a tilted pulse-front. . . . .	58
4.7	SHG amplitude reduction factor versus normalized dispersion parameter.	69
4.8	Noncollinear SHG response function. . . . .	70
4.9	Diagram of reduced FH intensity and increased duration due to GVD.	72
4.10	Diagram of mismatched GVD between FH and SH waves in SHG. . .	73
4.11	SHG acceptance bandwidth versus effective GVD parameter. . . . .	73
4.12	Diagram of spatial walkoff in noncollinear interactions. . . . .	74
4.13	Spatial beam profiles for several values of normalized walkoff parameter.	75
4.14	Efficiency reduction factor versus spatial walkoff parameter and effective GVD parameter. . . . .	80
4.15	Normalized SH amplitude versus effective GVD parameter. . . . .	82
4.16	Conversion efficiency and beam size and quality versus spatial walkoff parameter. . . . .	84
4.17	Diagram of three-wave mixing with tilted pulse fronts for group-velocity mismatch compensation. . . . .	88
4.18	Angle of signal and idler beams in tilted pulse-front optical parametric amplification versus wavelength. . . . .	89
4.19	Pulse-front tilt of signal and idler pulses for group-velocity mismatch compensated OPA. . . . .	90
5.1	Soliton parametric amplification with chirped gratings. . . . .	96
5.2	Diagram of the experimental setup for the measurement of quadratic spatial solitons in optical parametric amplification. . . . .	98
5.3	Images of soliton formation in optical parametric amplification in PPLN.	99
5.4	Measured spatial intensity plots of engineered solitons. . . . .	100
5.5	Measured properties of spatial solitons in chirped QPM gratings. . . .	102
6.1	Wavevector diagram illustrating the difference between positive and negative wavevector mismatch for spatially-confined CW OPA. . . . .	110

6.2	Measured and calculated spectra of the signal wave at the exit of a soliton parametric amplifier . . . . .	119
6.3	Spatial mode profiles for OPA soliton experiments at various signal wavelengths. . . . .	120
6.4	Excitation efficiency and noise content for solitons in uniform gratings.	122
6.5	Excitation efficiency and noise content for solitons in chirped gratings.	123
6.6	Dependence of excitation efficiency and noise content on input signal power . . . . .	125
6.7	Propagation of near-stationary state fields at negative wavevector mismatch in the presence of noise . . . . .	127
6.8	Propagation of near-stationary state fields at zero wavevector mismatch in the presence of noise . . . . .	128
6.9	Gain of noise content versus normalized distance . . . . .	129
6.10	Noise content and soliton content in near-ideal soliton propagation with noise . . . . .	131
6.11	Simulation of low gain efficiency-enhanced soliton parametric amplifier with low noise. . . . .	133



# Chapter 1

## Introduction

### 1.1 Motivation

“Ultrafast” is a term commonly used to describe optical pulses with a duration of less than 1 picosecond ( $10^{-12}$  seconds). The shortest laser pulses in the optical regime have been demonstrated with a duration of only a few femtoseconds ( $10^{-15}$  seconds), approaching a duration equal to the period of visible electromagnetic waves. Such short-duration pulses also possess large bandwidth; for the shortest optical pulses the bandwidth exceeds the entire visible portion of the electromagnetic spectrum. Recent advances in the applications of ultrashort pulses take advantage of the broad bandwidth for optical-frequency metrology [1] and medical imaging techniques such as optical coherence tomography [2]. The short duration enables the measurement of fast processes in chemistry and biology, and the rapid transmission of data through optical fiber links. The largest achievable laboratory electric fields are generated in ultrashort pulses[3], and the delivery of high peak power in a short temporal duration makes possible the precise laser machining of materials without associated heating [4].

The workhorse of ultrafast lasers is currently the Ti:Sapphire laser, operating in the near-infrared spectral region and capable of generating pulses as short as a few femtoseconds in duration. Recent advances in semiconductor saturable-absorber mirror (SESAM) and double-chirped, dispersion-compensating mirrors have enabled

simpler, cheaper, and more compact designs of the Ti:Sapphire laser [5]. Ultrafast lasers have been demonstrated in laser gain media other than Ti:Sapphire (organic dye, Nd:YAG, Yb:YAG, Cr:LiSAF, Er:fiber, and semiconductor diodes, to name a few) from the visible to the mid-infrared. Despite the broad spectral range over which ultrafast lasers have been demonstrated, there are yet limitations of efficiency, peak power, average power and pulse duration; as well as more practical limitations of size, cost, and complexity that determine the usefulness of each laser technology with regard to any particular application.

Since the first demonstration of nonlinear optical frequency conversion[6], nonlinear optics has developed with the primary goal of extending the utility of established laser technology through frequency conversion. This dissertation is concerned with second-order nonlinear frequency conversion processes, such as second-harmonic generation (SHG), sum-frequency generation (SFG), difference-frequency generation (DFG), and optical parametric amplification (OPA).

Dispersion in the refractive index most often results in a mismatch between the phase velocities of interacting frequencies in nonlinear optics. If the mismatch in phase velocities is not compensated, accumulated growth of generated waves over long interaction lengths is prohibited. It is possible to perfectly match the phase velocities through birefringence; choosing the polarization and propagation directions of interacting waves appropriately to result in a phase-matched interaction and efficient nonlinear conversion. This technique, however, has limitations. The resultant nonlinear drive relies on off-diagonal elements of the nonlinear susceptibility, which are usually smaller than their diagonal counterparts. In addition, birefringent phase matching is only possible over a limited portion of the transparency window for a given nonlinear material.

Quasi-phase-matching is a technique for compensating phase-velocity mismatch through periodic inversion of the nonlinear coefficient. First proposed in 1962[7], QPM has emerged as an important technology in nonlinear optics. It has been widely adopted for use in every second-order nonlinear interaction, and has been demonstrated in a variety of materials including quartz[8], KTP[9], RTA[10], GaAs[11], LiTaO<sub>3</sub>[12], and LiNbO<sub>3</sub>[13]. All the experiments in this work have been performed

in periodically-poled lithium niobate (PPLN), but the demonstrated engineering is directly applicable to any QPM material system.

QPM allows for the use of the largest element of the nonlinear susceptibility tensor, and is applicable across the entire transparency window of a given nonlinear material; limited only by the ability to fabricate the requisite inversion of the nonlinear coefficient. Most commonly, modulation of the nonlinear susceptibility is accomplished in ferroelectric materials through application of a patterned electric field which facilitates the inversion of ferroelectric domains[14]; however, diffusion-bonded stacks, as-grown QPM materials[11], and mechanically-induced twins[8] have also been applied for periodic modulation of the nonlinear coefficient.

Just as impressive as the broad applicability of uniform QPM materials has been the emergence of QPM engineering. The patterning of QPM domains lateral to the beam propagation direction can enable tunable nonlinear devices[15, 16], spatial Fourier engineering [17], and the construction of nonlinear photonic crystals [18]. Longitudinal patterning has resulted in demonstrated ability to compensate dispersion [19, 20, 21] and engineer the frequency-domain response function [22, 23]. These are but a few of the proposed and demonstrated applications of QPM engineering – all made possible through spatial modulation of the sign of the nonlinear susceptibility.

In this dissertation, we expand the scope of QPM domain engineering as applied to the frequency conversion of short optical pulses.

## 1.2 QPM Nonlinear Optical Frequency Conversion

The generation of new frequencies is made possible by the nonlinear part of the polarization resulting from an applied electric field  $\mathbf{E}$ :

$$\mathbf{P} = \varepsilon_0 \left( \chi^{(1)} \mathbf{E} + \chi^{(2)} \mathbf{E}^2 + \chi^{(3)} \mathbf{E}^3 + \dots \right) \quad (1.1)$$

where  $\chi^{(j)}$  is the  $j^{th}$ -order susceptibility tensor. The polarization resulting from an applied field drives an electric field at same frequency as that of the driving polarization. The first-order term is responsible for linear optical effects such as refraction,

dispersion, and diffraction.

The non-linear terms ( $j > 1$ ) are responsible for the generation of new frequencies. Second-order ( $\chi^{(2)}$ ) effects such as mentioned in the previous section are the topic of this thesis. The elements of the second-order susceptibility tensor depend on the interacting frequencies, and which element or combination of elements is applicable to a particular interaction depends on the interaction geometry (i.e. the propagation direction and field polarizations). In the time domain we typically speak of the nonlinear coefficient  $d$ , which is twice the appropriate  $\chi^{(2)}$  element for a particular interaction geometry evaluated at the carrier frequencies of the interacting fields. (Although  $\chi^{(2)}$  is defined in the frequency domain, the time-domain nonlinear coefficient  $d$  may be related to  $\chi^{(2)}$  as  $d = 2\chi^{(2)}$  for frequencies far from material resonant frequencies, where the nonlinear susceptibility  $\chi^{(2)}$  is only very weakly dispersive. For all discussions in this thesis  $\chi^{(2)}$  is considered nondispersive. For further discussion on the nonlinear susceptibility and the nonlinear coefficient  $d$ , see Ref. [24].)

Third-order ( $\chi^{(3)}$ ) effects will be neglected for much of this work, but are the leading nonlinear effects in materials with inversion symmetry, for which  $\chi^{(2)} = 0$ . Third-order nonlinear effects include self-phase modulation, self-focusing, phase conjugation, and general four-wave mixing.

The simplest second-order nonlinear process is second-harmonic generation, where an electric field at the first-harmonic (FH) frequency  $\omega_1$  results in a nonlinear polarization at the second-harmonic (SH) frequency  $\omega_2 = 2\omega_1$ . The polarization wave travels at the phase-velocity of the FH wave ( $c/n_1$ ), while the generated SH field travels at the phase velocity  $c/n_2$ , where  $c$  is the speed of light, and  $n_i$  is the refractive index of the nonlinear material for the FH ( $i = 1$ ) and SH ( $i = 2$ ) waves.

If  $n_1 \neq n_2$  two freely propagating waves at the FH and SH frequencies will be  $\pi$  out of phase after a coherence length, defined as  $L_c = c/(\pi\omega|n_1 - n_2|)$ . Since the polarization wave travels at the phase velocity of the FH wave, at a distance equal to  $L_c$  the phase difference between the SH wave and the generating polarization wave slips by  $\pi$ . This phase slip occurs periodically and limits the growth of the generated SH field, as shown in Fig. 1.1. If  $n_1 = n_2$ , the SH wave and the polarization wave have a

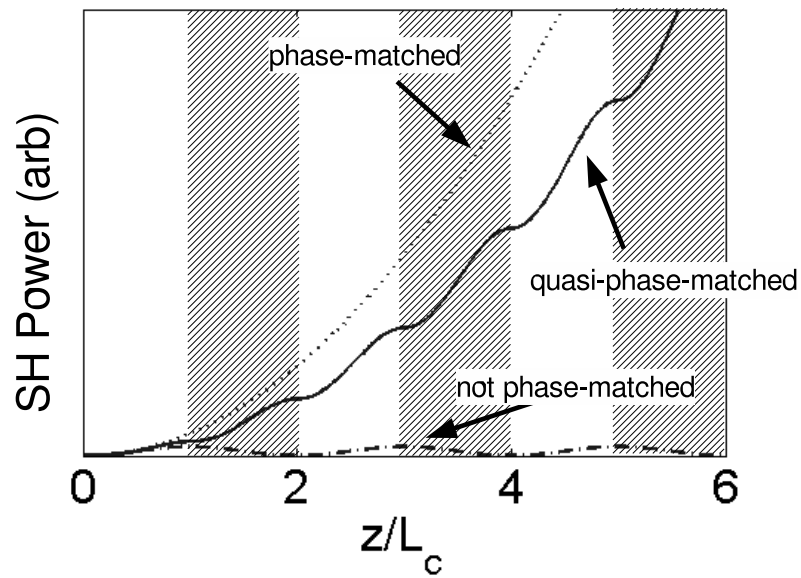


Figure 1.1: SHG output power versus distance  $z$  normalized to the coherence length  $L_c$ . SHG grows quadratically if there is no mismatch in phase velocities. In the presence of phase-velocity mismatch, SHG power oscillates between zero and a maximum value reached at odd values of the coherence length. If the sign of the nonlinear coefficient is reversed periodically, as indicated by the shaded region, quasi-phase-matching allows for monotonic growth of nonlinear output in the presence of a phase-velocity mismatch between interacting waves.

fixed phase relationship with propagation, and SH power grows monotonically; however, this condition is only satisfied at specific frequencies for a particular geometry in a given nonlinear material. The alternative technique of quasi-phase-matching is realized through periodic modulation of sign of the nonlinear coefficient, at a period of  $\Lambda = 2mL_c$ , where  $m$  is an integer, and indicates the QPM order. Such modulation periodically resets the phase between interacting waves, allowing for monotonic growth of generated frequencies, as shown in Fig. 1.1.

QPM may also be described in terms of the terms of the wavevectors  $k_i = 2\pi n_i/\lambda_i$ , where  $i = 1$  for the FH, and  $i = 2$  for the SH;  $\lambda_i$  represents the wavelength in vacuum. The wavevector mismatch is defined as  $\Delta k_0 = 2k_1 - k_2$ . (Note with this definition,  $\Delta k_0$  is often negative.) The effective wavevector mismatch is  $\Delta k = \Delta k_0 + K_g$ , where  $K_g = 2\pi m/\Lambda$  is the magnitude of the QPM grating vector.

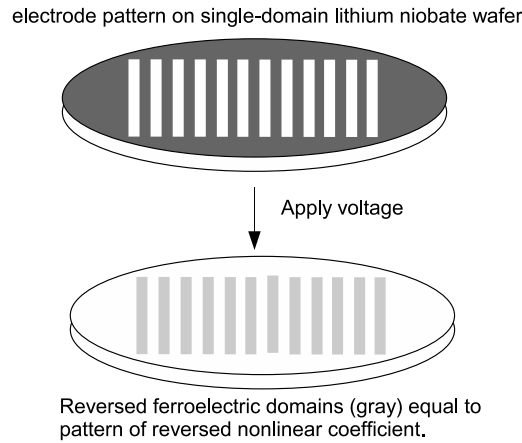


Figure 1.2: Lithographic fabrication of periodically-poled lithium niobate. An electrode pattern is defined on the surface of a single-domain lithium niobate wafer (top). Application of an electric field above the coercive field results in reversal of the ferroelectric domains beneath the patterned electrodes (bottom). Reversal of the ferroelectric domain corresponds to reversal of the sign of the nonlinear coefficient necessary for quasi-phase-matching.

Fig. 1.2 illustrates schematically the fabrication of periodically-poled lithium niobate (PPLN), the QPM material used in all experiments discussed in this dissertation. QPM is achieved through the inversion of ferroelectric domains that occurs when an

electric field is applied to a pattern of electrodes on the surface of a single-domain lithium niobate wafer. This is similar to the fabrication process of other poled ferroelectric crystals, the most common variety of QPM materials in use. Other processes that also result in QPM devices take advantage of similar lithographic processing[11], where a lithographic pattern results in an identical pattern of QPM domains.

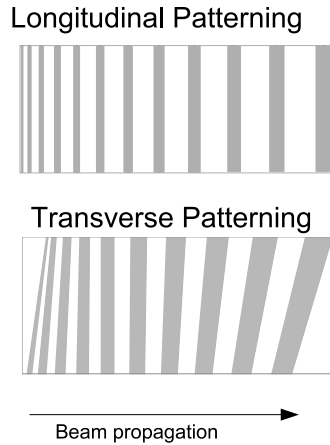


Figure 1.3: Non-uniform QPM patterns resulting from lithographic QPM fabrication. Alternating signs of the nonlinear coefficient (shown in gray and white) may be patterned non-uniformly along the direction of beam propagation (top) or transverse to the direction of propagation (bottom). The ability to spatially pattern QPM domains enables engineering of QPM devices.

Lithographic patterning can be used to generate not only periodic patterns, but also aperiodic patterns through the use of aperiodic lithographic masks, as shown in Fig. 1.3. Non-uniform QPM enables a class of engineered devices for nonlinear frequency conversion not possible before the advent of quasi-phase-matching. Periodic modulation of the sign of the nonlinear coefficient enables efficient frequency conversion through QPM; non-uniform modulation enables the engineering of QPM frequency conversion devices.

There are many published works on engineered QPM devices made possible through longitudinal and/or transverse patterning (shown in Fig. 1.3) of QPM materials. Longitudinally non-uniform (or aperiodic) QPM gratings have broader conversion bandwidths than uniform QPM materials of equivalent length [25, 26]. Engineered

superstructures can be designed to have phase-matching peaks at multiple chosen frequencies [22, 27, 18]. Furthermore, aperiodic QPM gratings have been used for the demonstration of nonlinear crystals with engineered phase responses suitable for pulse compression and dispersion management in single-pass nonlinear frequency conversion [28, 29, 30]. Aperiodic gratings have also been used for pulse compression in ultrafast synchronously-pumped parametric oscillators [31]. Transverse patterning has been used for tunable devices [15, 16] as well as a tool for tailoring frequency conversion in the spatial-frequency domain [18, 17].

### 1.3 Nonlinear frequency conversion of short optical pulses

To understand the application of QPM engineering in ultrafast frequency conversion, we first review some of the challenges to the efficient conversion of ultrashort pulses in uniform (or uniformly periodic) nonlinear materials.

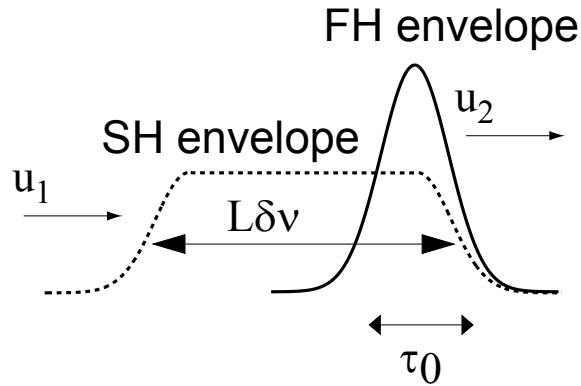


Figure 1.4: Time-domain schematic of group-velocity mismatch in SHG. The diagram shows the temporal walkoff between interacting waves resulting from the different group velocities ( $u_1$  and  $u_2$ ) of the FH and SH interacting waves. If the net group delay  $L\delta\nu$  is greater than the FH pulse duration  $\tau_0$  then the generated SH envelope is longer than the FH pulse.

If the phase-matching (or quasi-phase-matching) condition is met for the carrier frequencies of interacting fields, efficient frequency conversion of short optical pulses in a uniform (or uniformly periodic) nonlinear crystal is typically limited by the difference in group velocities, as illustrated in Fig. 1.4. As the FH and SH waves propagate, the generated SH envelope walks off the generating polarization envelope in a distance equal to the walkoff length  $L_g = \tau_0/\delta\nu$ , where  $\tau_0$  is the width of the FH temporal envelope. The group-velocity mismatch (GVM) parameter  $\delta\nu = (u_1^{-1} - u_2^{-1})$  is defined as the difference in reciprocal group velocities, where  $u_1$  and  $u_2$  are the group velocities of the FH and SH pulses, respectively. For interactions longer than  $L_g$ , the generated SH pulse will be limited in peak amplitude and will be longer in duration than the FH pulse.

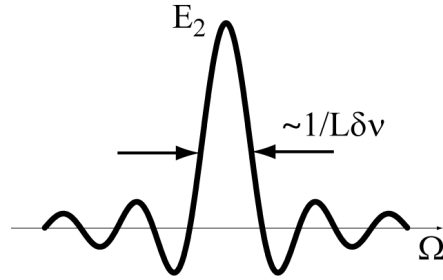


Figure 1.5: Second-harmonic amplitude versus frequency detuning in a uniform nonlinear crystal. The SH amplitude decreases with frequency detuning due to accumulating frequency-dependent wavevector mismatch. The width of this tuning curve is inversely proportional to the interaction length  $L$  and the GVM parameter  $\delta\nu = (\partial\Delta k/\partial\omega)^{-1}$ .

The extended temporal duration of the SH pulse in a crystal longer than the walkoff length is a result of limited frequency conversion bandwidth, since wavevector mismatch  $\Delta k$  changes with frequency detuning. Consider SHG at SH frequency  $\omega_2$  that is quasi-phase-matched ( $\Delta k(\omega_2) = 0$ ). A nearby frequency at  $\omega = \omega_2 + \Omega$  will have a non-zero wavevector mismatch  $\Delta k(\Omega) \approx \delta\nu\Omega$ , where  $\delta\nu = (\partial\Delta k/\partial\omega)^{-1}$  is

the same GVM parameter defined in the previous paragraph for the time-domain description. The amplitude of the SH field  $E_2$  generated by a continuous-wave FH input to a uniform nonlinear crystal versus frequency detuning is shown in Fig. 1.5. The width of the response function is inversely proportional to the interaction length  $L$  and the GVM parameter  $\delta\nu$ .

If, instead of a tunable CW first-harmonic input the SHG interaction is pumped by a broadband FH waveform such as a short optical pulse, then the broad bandwidth of the FH signal will be converted to a similarly broadband SH signal if the bandwidth of the response function (shown in Fig. 1.5) is broader than the bandwidth of the FH signal; i.e. if  $L < L_g$ , where  $L_g = \tau_0/\delta\nu$  is the same walkoff length used in the time-domain description.

The frequency-domain SHG response function shown in Fig. 1.5, also known as the SHG tuning curve, represents the basic idea of the SHG transfer function. The shape of the SHG transfer function depends on the nonlinear coefficient distribution, and while Fig. 1.5 shows the transfer function for a uniform nonlinear crystal, non-uniform crystals have transfer functions which may be engineered through manipulation of the nonlinear coefficient distribution. In Chapter 2 I re-derive the QPM-SHG transfer function presented by Imeshev *et. al* in Refs. [32, 23], and review the key result that a non-uniform QPM grating can be designed with nearly arbitrary conversion bandwidth as well as an engineered phase response through the use of chirped-period QPM gratings.

Engineering of the SHG transfer function is not the only way to achieve a broader SHG frequency response and compensate for GVM. Choosing a material with low GVM parameter at the interacting frequencies is the most straightforward solution to the limitations of group-velocity walkoff. However, this solution is typically applicable in only a small portion of the transparency window of a particular nonlinear material. For quasi-phase-matched materials, if QPM can be used to compensate the mismatch in phase velocities, it is possible to use birefringence to match the group velocities[33, 34, 35, 36, 37, 38]. This approach also has its drawbacks, as it necessitates the use of off-diagonal elements of the susceptibility tensor often resulting in a reduced nonlinear response.

Conditioning the input field can also be used to effectively broaden the nonlinear response function. In a critically phase-matched (or quasi-phase-matched) interaction the phase-matched frequency varies linearly with the incident angle to the nonlinear crystal. If the angular dispersion of a broadband incident field is arranged to match the angular dependence of phase-matching, all frequencies can be simultaneously phase-matched in a single crystal, even if it is much longer than the group-velocity walkoff length as defined above. This technique has been used in birefringent materials to achieve broadband CW tuning of nonlinear interactions [39, 40, 41, 42, 43, 44, 45].

In the time-domain, spectral angular dispersion of the frequency components in a short optical pulse results in a pulse amplitude front that is tilted with respect to the direction of propagation. Broadband phase-matching using spectral angular dispersion is equivalent to matching the group-velocity of the FH pulse to the projection of the group-velocity of the SH pulse along the direction of FH propagation using a non-collinear geometry. A tilted pulse-front is necessary to maximize the overlap of field envelopes during propagation. This technique has been demonstrated in birefringent materials [46, 47, 48] and proposed in QPM nonlinear devices [26]. Chapter 4 describes the first demonstration of this technique in QPM devices. One important difference between applying this technique to QPM and birefringent materials is that the phase-matching angle is dictated entirely by the material dispersion in birefringent materials, whereas in QPM devices the angle between the interacting first-harmonic and second-harmonic waves may be chosen by appropriate choice of the QPM period. Chapter 4 also contains the first calculation of the conversion efficiency for this class of devices, as well as optimization of the energy conversion efficiency through proper choice of the phase-matching angles and focusing condition.

In addition to broad conversion bandwidth, longitudinally-patterned QPM devices have enabled the demonstration of pulse compression during SHG [28]. QPM-SHG pulse compression (described in detail in Refs. [49, 32, 23]) results from the interplay of group velocity mismatch and localized frequency conversion along the propagation direction in a non-uniform QPM device. Complete pulse compression, i.e. flat spectral phase, results when the chirp of a QPM grating is matched to the chirp of a stretched FH pulse. In Chapter 3 we combine longitudinal patterning with transverse

patterning to create a tunable device which can accept a range of FH pulse chirps for complete compression during SHG in a single, monolithic QPM device.

## 1.4 Optical Parametric Amplification of Short Optical Pulses

In addition to the generation of new optical frequencies, nonlinear optical techniques can be used to amplify small signals through optical parametric amplification (OPA). OPA involves the transfer of energy from a high-power pump wave to a low-power signal wave at a lower frequency through nonlinear frequency mixing. The difference frequency, called the idler, is generated in the process.

Ultrashort optical pulses may be amplified using the technique of chirped-pulse optical parametric amplification (CPOPA), illustrated schematically in Fig. 1.6. This technique was first suggested in Ref. [50]. Ultrashort pulses are first stretched (chirped) to a much longer duration in an optical element with large group-delay dispersion, then amplified in an optical parametric amplifier before compression in a dispersive element with dispersion opposite to the group-delay dispersion of the chirped, amplified pulses. This is distinguished from the technique of chirped pulse (laser) amplification (CPA) introduced in Ref. [51] only by the choice of gain medium: parametric amplification as compared with laser amplification. Both chirped-pulse amplification techniques were developed to mitigate the effects of high-peak-intensity fields generated during the direct (un-chirped) amplification of short pulses, since high peak intensity can result in optical damage and parasitic nonlinearities. Using CPA (or CPOPA) ultrashort pulses can be amplified to high energy with comparatively low peak intensity.

OPA offers several advantages when compared with conventional laser amplification: there is no inherent thermal loading, as poses engineering challenges in the design of laser amplifiers; the frequency and bandwidth are not constrained by quantum transitions inside the amplifier medium, making OPA suitable for the amplification over a broad tuning range; and OPA is capable of extremely large gain, in excess of

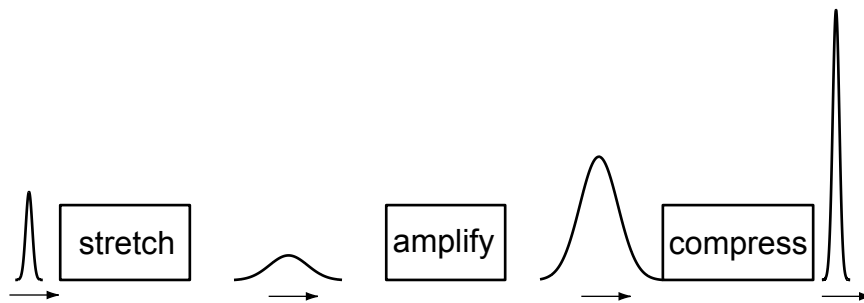


Figure 1.6: Schematic diagram of the chirped-pulse optical parametric amplification (CPOPA) technique for the amplification of ultrashort pulses. The CPOPA system is shown schematically from left to right, where short pulses are first stretched using a dispersive element (typically a pair of diffraction gratings) before amplification. After the amplification stage, the chirped pulses have high energy, but low peak intensity to avoid optical damage and parasitic nonlinearities inside the gain medium. Finally, pulses are compressed (typically with another grating pair), resulting in amplified ultrashort pulses.

100 dB, eliminating the need for regenerative amplifiers in the chirped-pulse amplification of ultrashort pulses. With a time-dependent pump, OPA can also eliminate the amplification of satellite pulses present in ultrafast laser amplifiers.

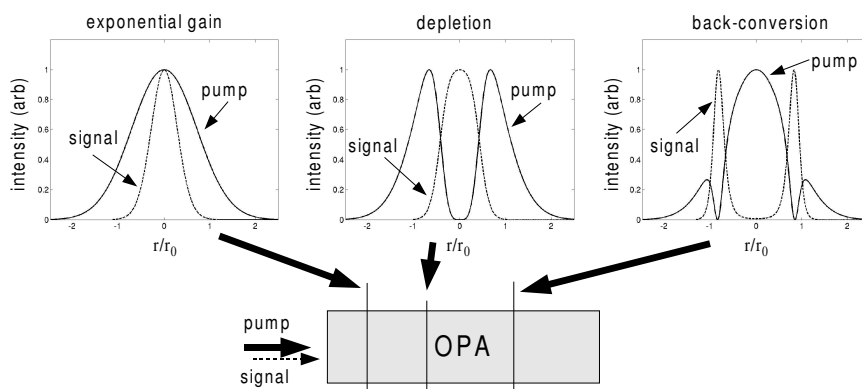


Figure 1.7: Pump and Signal intensity envelopes in a saturated parametric amplifier. Ignoring the effects of diffraction, we plot the spatial intensity envelopes of pump and signal beams along the propagation coordinate of a parametric amplifier. Graphs show three regimes. LEFT: In the growth regime, the signal intensity envelope is narrower than the pump envelope due to the nonlinear nature of OPA. CENTER: When depletion is reached, it is reached first in the center of the pump beam, leaving unconverted energy in the periphery. RIGHT: Further driving of the amplifier results in back-conversion in the center of the beam, resulting in no net increase in conversion efficiency.

Although a plane-wave pump can be driven to complete depletion[52] (100% conversion to signal-idler pairs), it is difficult to achieve total conversion in CPOPA with Gaussian (or otherwise spatially nonuniform) beams. Fig. 1.7 illustrates this point more clearly, plotting the depletion of a non-uniform Gaussian pump beam in a parametric amplifier when diffraction may be neglected. In this figure, it's clear

that non-uniform saturation and back conversion limit the total conversion efficiency of parametric amplification with Gaussian (or otherwise non-uniform) pump beams. When diffraction is considered, cascaded conversion and diffraction result in more complicated dynamics but similarly limited conversion efficiency.

High photon conversion efficiency (58%) has been achieved through spatial and temporal flattening of the pump intensity [53]; however, lower photon conversion efficiency ( $\leq 10\%$ ) is typical when using commercially available pump sources[54], and has been reported as high as 38% when the pump beam has a super-Gaussian spatial intensity envelope[55]. Flattening of the pump intensity profile often requires complicated optical systems to achieve substantial increase in conversion efficiency. Moreover, the magnitude of parametric gain (which depends on the pump intensity, the material nonlinearity, and the interaction length) must be carefully controlled to avoid back-conversion.

In Chapter 5 we present an alternative solution to this problem, which takes advantage of the properties of solitons formed in nonlinear frequency conversion. In this approach, nonlinear eigenstates of nonlinear frequency mixing are manipulated through the use of engineered nonlinear materials to result in enhanced conversion to signal-idler pairs. The properties of spatial solitons are discussed in more detail in Chapter 2, which lays the foundation for applications to efficient parametric amplification in Chapter 5. In the experiments of Chapter 5 we find that the utility of spatial solitons for improving the efficiency of a parametric amplifier is somewhat limited by the presence of parametric noise, and so we discuss parametric noise and its influence on the excitation of solitons in Chapter 6.

## 1.5 Overview

Sections 1.2 through 1.4 give a brief glimpse into the potential of QPM in regard to the properties that distinguish short optical pulses from CW fields: broad bandwidth, well-controlled optical phase, and large amplitude. We have introduced a few of the challenges of frequency conversion associated with these particular properties: the finite acceptance bandwidth of SHG, and back-conversion which limits the conversion

efficiency of parametric amplifiers. In addition, we have posed several solutions to these challenges that arise from QPM, suggesting that engineered QPM devices can be used to broaden the conversion bandwidth, provide optical phase control, and improve the conversion efficiency of a parametric amplifier. The remainder of this thesis elaborates on these concepts, and in a series of experiments expands the scope of QPM applied to ultrafast nonlinear optics.

In Chapter 2 we review the derivation of equations that describe general three-wave mixing in QPM nonlinear materials, and discusses a few important cases relevant to later chapters in this thesis.

In Chapter 3 we discuss the use of both lateral and longitudinal patterning to extend the application of QPM pulse shaping to tunable devices and demonstrates tunable-chirp pulse compression in a chirped, fanned QPM nonlinear device.

Chapter 4 contains the demonstration of group-velocity mismatch compensation in noncollinear SHG with spectral angular dispersion. A comprehensive analytical theory is presented, including the effects of dispersion, diffraction, and spatial walkoff. The theoretical analysis is applied to the optimization of conversion efficiency in similar devices, and is compared with other known techniques for ultrafast frequency conversion.

The later chapters of this thesis focus on the properties of multi-color spatial solitons. Chapter 5 demonstrates the use of chirped QPM gratings for the tailoring of quasi-CW spatial solitons. Enhanced content of signal-idler pairs in multi-color spatial solitons is shown through the use of chirped QPM gratings. Although the signal-idler content of spatial solitons may be enhanced through the use of a chirped grating the net conversion efficiency in such a soliton parametric amplifier is limited by poor soliton excitation efficiency, which is influenced by the presence of amplified parametric noise. Chapter 6 discusses the influence of parametric noise on the generation and propagation of spatial solitons. Parametric noise is shown to grow and disrupt the spatial confinement of propagating solitons and both experimental results and numerical simulation suggest that spatial solitons may be unstable in the presence of parametric noise.

Chapter 7 summarizes this dissertation.

# Chapter 2

## Theory of three-wave mixing in QPM materials

### 2.1 Introduction

In this chapter we discuss the theoretical foundation for second-order nonlinear optics. In Section 2.2 we derive the coupled wave equations that govern collinear three-wave mixing. In Section 2.3 we cast these equations in terms of characteristic lengths corresponding to the effects of diffraction, group-velocity mismatch, and group-velocity dispersion. Such normalization makes transparent the scaling of these effects when compared with the interaction length.

Two simple cases of plane-wave CW nonlinear mixing give some basic insight into the scaling of nonlinear mixing in the cases of SHG, discussed in Section 2.4 and OPA discussed in Section 2.5. In addition, these cases clarify the parameter space for which the assumption of an undepleted pump is valid.

Section 2.6 discusses the transfer function interpretation for ultrafast frequency conversion. This section lays the mathematical foundation for the understanding of engineered QPM structures used in Chapters 3 and 4 to tailor the frequency conversion of ultrashort optical pulses.

Section 2.7 concerns the definition and properties of spatial solitons in three-wave mixing. Such formalism will be useful when reading Chapters 5 and 6, which concern

the engineering of solitons using chirped QPM gratings, as well as the influence of noise on soliton excitation and propagation.

## 2.2 The coupled wave equations

The wave equation, which can be derived directly from Maxwell's equations[56], describing the propagation of an electric field  $\mathbf{E}$  in a nonlinear, nonmagnetic dielectric is

$$\nabla^2 \mathbf{E} - \frac{\partial^2}{\partial t^2} \left( \frac{n^2}{c^2} \mathbf{E} \right) = \mu_0 \frac{\partial^2 \mathbf{P}_{NL}}{\partial t^2} \quad (2.1)$$

where  $\mathbf{P}_{NL}$  is the nonlinear part of the induced polarization  $\mathbf{P}$  given in Eq. 1.1, and  $n$  is the (frequency-dependent) refractive index. If we consider only the second-order nonlinear term of the induced polarization, then  $\mathbf{P}_{NL} = 2\epsilon_0 d \mathbf{E}^2$ .

To properly consider the effects of dispersion in the refractive index, it is more convenient to write this equation in the frequency domain:

$$\nabla^2 \hat{\mathbf{E}} + k^2(\omega) \hat{\mathbf{E}} = -\mu_0 \omega^2 \hat{\mathbf{P}}_{NL}. \quad (2.2)$$

Consider collinear propagation of electric fields with non-overlapping spectra, centered at frequencies  $\omega_j$ , where the indices  $j = 1, 2, 3$  represent signal, idler, and pump waves, respectively. By convention, the pump wave is the highest-frequency wave, such that  $\omega_3 = \omega_2 + \omega_1$ . With field-polarization unit vectors  $\hat{e}_j$ , the normalized electric field envelopes  $B_j$  for fields propagating along the  $z$ -direction are defined according to

$$\mathbf{E}_j(\mathbf{r}, t) = \hat{e}_j E_0 B_j(\mathbf{r}, t) \exp(i\omega_j t - ik_j z), \quad (2.3)$$

where  $E_0$  is the characteristic field amplitude, typically defined as the amplitude of the strongest input field (the FH field in SHG, or the pump field in OPA). The Fourier transform of this time-domain envelope is

$$\hat{\mathbf{E}}_j(\mathbf{r}, \omega) = \hat{e}_j E_0 \hat{B}_j(\mathbf{r}, \Omega_j) \exp(-ik_j z), \quad (2.4)$$

where  $\Omega_j = \omega - \omega_j$  is the deviation from the carrier frequency  $\omega_j$ .

Substitution of the total electric field  $\Sigma_j \hat{\mathbf{E}}_j$  into Eq. 2.2 results in three coupled equations for the frequency-domain electric field envelopes  $\hat{A}_j$ :

$$\nabla^2 \hat{B}_1 + k^2(\omega) \hat{B}_1 = -\frac{\mu_0 \omega_1^2}{E_0} \hat{P}_{NL}^{(1)} \exp ik_1 z \quad (2.5)$$

$$\nabla^2 \hat{B}_2 + k^2(\omega) \hat{B}_2 = -\frac{\mu_0 \omega_2^2}{E_0} \hat{P}_{NL}^{(2)} \exp ik_2 z \quad (2.6)$$

$$\nabla^2 \hat{B}_3 + k^2(\omega) \hat{B}_3 = -\frac{\mu_0 \omega_3^2}{E_0} \hat{P}_{NL}^{(3)} \exp ik_3 z, \quad (2.7)$$

where  $\hat{P}_{NL}^{(j)}$  is the frequency-domain nonlinear polarization at frequency  $\omega_j$ . The time-domain nonlinear polarization is given as

$$P_{NL}^{(1)} = 2\epsilon_0 d E_0^2 B_2^* B_3 \exp(i\omega_1 t + ik_2 z - ik_3 z), \quad (2.8)$$

$$P_{NL}^{(2)} = 2\epsilon_0 d E_0^2 B_1^* B_3 \exp(i\omega_2 t + ik_1 z - ik_3 z), \quad (2.9)$$

$$P_{NL}^{(3)} = 2\epsilon_0 d E_0^2 B_1 B_2 \exp(i\omega_3 t - ik_1 z - ik_2 z). \quad (2.10)$$

For the specific case of type I (or type 0) SHG, where the signal and idler waves are degenerate, the nonlinear polarization at the SH frequency ( $j = 3$ ) is  $(1/2)P_{NL}^{(3)}$  as given above.

The dispersion relation  $k(\omega)$  can be expanded around the appropriate frequency for each of the coupled wave equations:

$$k^2(\omega) \approx k_j^2 + 2\frac{k_j}{u_j} \Omega_j + \frac{1}{u_j^2} \Omega_j^2 + k_j \beta_j \Omega_j^2, \quad (2.11)$$

where  $\Omega_j = \omega - \omega_j$  is the frequency detuning, and  $k_j = k(\omega_j)$ . The group velocity is defined as

$$u_j = \left. \frac{\partial k}{\partial \omega} \right|_{\omega_j}, \quad (2.12)$$

and the group-velocity dispersion coefficient is

$$\beta_j = \left. \frac{\partial^2 k}{\partial \omega^2} \right|_{\omega_j}. \quad (2.13)$$

In the limit of paraxial waves and with time  $T = t - z/u_3$  measured in a coordinate frame travelling at the group velocity of the pump wave, the time-domain coupled-wave equations for three-wave mixing are

$$-2ik_1 \frac{\partial B_1}{\partial z} + \nabla_{\perp}^2 B_1 - 2ik_1 \delta \nu_{1,3} \frac{\partial B_1}{\partial T} - k_1 \beta_1 \frac{\partial^2 B_1}{\partial T^2} = -E_0 K_1 B_2^* B_3 \exp(i\Delta k z) \quad (2.14)$$

$$-2ik_2 \frac{\partial B_2}{\partial z} + \nabla_{\perp}^2 B_2 - 2ik_2 \delta \nu_{2,3} \frac{\partial B_2}{\partial T} - k_2 \beta_2 \frac{\partial^2 B_2}{\partial T^2} = -E_0 K_2 B_1^* B_3 \exp(i\Delta k z) \quad (2.15)$$

$$-2ik_3 \frac{\partial B_3}{\partial z} + \nabla_{\perp}^2 B_3 - k_3 \beta_3 \frac{\partial^2 B_3}{\partial T^2} = -E_0 K_3 B_1 B_2 \exp(-i\Delta k z). \quad (2.16)$$

In Eqs. 2.14 through 2.16, the nonlinear coefficient is assumed to have a dominant grating vector of magnitude  $K_g$  such that

$$d \approx d_m \exp(iK_g z), \quad (2.17)$$

so that  $\Delta k = k_1 + k_2 - k_3 + K_g$  (see Ref. [14]). The nonlinear coupling constants are given as  $K_j = 2d_m \omega_j^2 / c^2$ .

## 2.3 Characteristic Length Scales

The coupled scalar equations for the evolution of space-time envelopes in collinear three-wave mixing given by Eqs. 2.14 through 2.16 are valid in the presence of diffraction, group-velocity mismatch, group-velocity dispersion, and pump depletion. For many physically interesting boundary conditions no analytical solution exists to Eqs. 2.14 through 2.16. It is important, therefore, to recognize when certain terms may be neglected such that the equations may be simplified for the purposes of analytical or numerical analysis. Generally, terms may be neglected when the associated characteristic length is much longer than the interaction length.

To make apparent the appropriate length scales for three-wave mixing, we recast Eqs. 2.14 through 2.16 in terms of normalized variables: propagation coordinate  $\bar{z} = z/L$  given in terms of the interaction length, transverse distance  $\bar{r} = r/r_0$  given in terms of the beam width  $r_0$ , and time  $\bar{T} = T/\tau_0$  defined as normalized to the characteristic pulse duration  $\tau_0$ .

Interaction Length	$L$
Rayleigh Length	$L_{R,j} = k_j r_0^2$
Group-Velocity Walkoff Length	$L_{g,j} = \frac{\tau_0}{\delta\nu_{j,3}}$
Group-Velocity Dispersion Length	$L_{D,j} = \frac{2\tau_0^2}{\beta_j}$
Nonlinear Mixing Length	$L_G = \frac{c}{d_m E_0} \sqrt{\frac{n_1 n_2}{\omega_1 \omega_2}}$

Table 2.1: Characteristic lengths in three-wave mixing.

In normalized units, the coupled equations are

$$-i \frac{\partial B_1}{\partial \bar{z}} + \frac{L}{L_{R,1}} \bar{\nabla}_\perp^2 B_1 - i \frac{L}{L_{g,1}} \frac{\partial B_1}{\partial \bar{T}} - \frac{L}{L_{D,1}} \frac{\partial^2 B_1}{\partial \bar{T}^2} = -\sqrt{\frac{n_2 \omega_1}{n_1 \omega_2}} \frac{L}{L_G} B_2^* B_3 \exp(i\delta k \bar{z}) \quad (2.18)$$

$$-i \frac{\partial B_2}{\partial \bar{z}} + \frac{L}{L_{R,2}} \bar{\nabla}_\perp^2 B_2 - i \frac{L}{L_{g,2}} \frac{\partial B_2}{\partial \bar{T}} - \frac{L}{L_{D,2}} \frac{\partial^2 B_2}{\partial \bar{T}^2} = -\sqrt{\frac{n_1 \omega_2}{n_2 \omega_1}} \frac{L}{L_G} B_1^* B_3 \exp(i\delta k \bar{z}) \quad (2.19)$$

$$-i \frac{\partial B_3}{\partial \bar{z}} + \frac{L}{L_{R,3}} \bar{\nabla}_\perp^2 B_3 - \frac{L}{L_{D,3}} \frac{\partial^2 B_3}{\partial \bar{T}^2} = -\frac{\omega_3}{n_3} \sqrt{\frac{n_1 n_2}{\omega_1 \omega_2}} \frac{L}{L_G} B_1 B_2 \exp(i\delta k \bar{z}), \quad (2.20)$$

with characteristic lengths defined in Table 2.1. The normalized wavevector mismatch is  $\delta k = \Delta k L$ , and represents the total amount of accumulated phase mismatch. The nonlinear mixing length is equal to the parametric gain length in the case of optical parametric amplification.

The mathematical and physical utility of characteristic lengths is most evident in Chapter 4 where we discuss the effects of all of the above terms, and include spatial walkoff (not included above) which is present in noncollinear interactions (or

in materials where Poynting vector walkoff must be considered). In Chapter 5, we discuss simplified scaling of the properties of quadratic spatial solitons (stationary solutions to the coupled equations which most often have no analytical representation) in terms of characteristic lengths. Moreover, in Chapter 6 we show that the definition of the characteristic lengths must be evaluated carefully; and that length over which GVM and GVD have an influence on the evolution of the nonlinear coupled equations may be determined more by the interaction bandwidth than by the pulse duration when parametric noise is included.

Each term on the left-hand side of Eqs. 2.18 through 2.20 may be ignored if the interaction length is much less than the associated characteristic length, or, equivalently, if the coefficient is much less than unity. The right-hand side contains the nonlinear driving terms, and consequently the characteristic nonlinear mixing length determines the length over which field amplitudes change as well as the pump-depletion length. To examine this more closely, we look separately at cases of quasi-phase-matched SHG and OPA, in the limit that diffraction and the dispersive effects of both GVM and GVD may be neglected.

## 2.4 Monochromatic, plane-wave SHG

The conventional notation for second-harmonic generation is to drop the idler equation (Eq. (2.19)) from Eqs. (2.18) through (2.20), and to use the indices  $j = 1, 2$  for the first-harmonic (FH, at frequency  $\omega_1$ ) and second-harmonic (SH, at frequency  $\omega_2 = 2\omega_1$ ) waves, respectively. As compared to the general three-wave mixing notation ( $j = 1, 2, 3$  for signal, idler, and pump), the highest index in both cases refers to the wave with the largest frequency.

With this change in notational convention, the CW, plane-wave coupled equations for phase-matched SHG are

$$i \frac{\partial B_1}{\partial z} = \frac{L}{L_G} B_1^* B_2 \quad (2.21)$$

and

$$i \frac{\partial B_2}{\partial z} = \frac{n_1}{n_2} \frac{L}{L_G} B_1^2, \quad (2.22)$$

where fields are normalized to the FH field amplitude  $E_0 = |E_1(\bar{z} = 0)|$ , and we assume that there is no SH input:  $B_2(\bar{z} = 0) = 0$ . If we ignore depletion of the FH wave, the solution for the SH amplitude is trivial:

$$B_2(L) = -i\sqrt{\frac{n_1^2}{n_2^2}} \left(\frac{L}{L_G}\right), \quad (2.23)$$

and the intensity conversion efficiency is

$$\eta_{SHG} = \frac{n_2|E_2|^2}{n_1|E_1|^2} = \frac{n_1}{n_2} \left(\frac{L}{L_G}\right)^2 = \frac{d_m^2 \omega_1^2}{n_1 n_2 c^2} L^2 |E_0|^2. \quad (2.24)$$

The undepleted-pump approximation implies low conversion efficiency, and is therefore valid in SHG when  $L \ll L_G$ .

## 2.5 Monochromatic, plane-wave OPA

In OPA, the fields are commonly normalized to the amplitude of a strong pump field ( $B_j = |E_j|/E_0$ , where  $E_0 = |E_3(\bar{z} = 0)|$ ), and the coupled equations in the limit of monochromatic plane waves are written as

$$i\frac{\partial B_1}{\partial \bar{z}} = \sqrt{\frac{n_2 \omega_1}{n_1 \omega_2}} \frac{L}{L_G} B_2^* B_3 \quad (2.25)$$

$$i\frac{\partial B_2}{\partial \bar{z}} = \sqrt{\frac{n_1 \omega_2}{n_2 \omega_1}} \frac{L}{L_G} B_1^* B_3 \quad (2.26)$$

$$i\frac{\partial B_3}{\partial \bar{z}} = \frac{\omega_3}{n_3} \sqrt{\frac{n_1 n_2}{\omega_1 \omega_2}} \frac{L}{L_G} B_1 B_2. \quad (2.27)$$

Considering an input at the signal frequency with initial level  $B_1(\bar{z} = 0) = B_1^0$ , the solutions are exponentially growing for the signal and idler waves in the limit of high gain ( $B_1^0 \ll 1$  and  $L \gg L_G$ ):

$$\frac{B_1(L)}{B_1^0} \approx \exp(\Gamma L), \quad (2.28)$$

$$\frac{B_2(L)}{B_1^0} \approx \exp(\Gamma L), \quad (2.29)$$

where  $\Gamma = 1/L_G$  is the parametric gain coefficient. The validity of assuming an undepleted pump, therefore, depends on the level of the input signal field, and is valid as long as  $B_1^0 \exp(\Gamma L) \ll 1$ .

## 2.6 Ultrafast SHG and the QPM-SHG transfer function

The frequency-domain SHG response function has long been used to explain the tuning behavior and acceptance bandwidth of nonlinear interactions. As mentioned in Section 1.3, the width of the SHG response function determines the duration of the shortest pulse which may be converted in a uniform nonlinear crystal. The limited pulse duration is due to group-velocity walkoff, or equivalently, the frequency-dependent wavevector mismatch. The transfer function description of SHG is even more powerful when considering non-uniform QPM devices. For a complete derivation and description of the frequency-domain transfer function, see Ref. [32]. Here, I summarize the results of that theory.

In the limit of an undepleted pump and a plane-wave interaction, and including the effects of dispersion, the frequency-domain coupled equations for SHG derived from Eq. (2.1) are

$$\frac{\partial^2}{\partial z^2} \hat{E}_1(z, \omega) + k^2(\omega) \hat{E}_1(z, \omega) = 0 \quad (2.30)$$

$$\frac{\partial^2}{\partial z^2} \hat{E}_2(z, \omega) + k^2(\omega) \hat{E}_2(z, \omega) = -\frac{\mu_0 \omega^2}{2} \hat{P}_{NL}^{(SHG)}(z, \omega), \quad (2.31)$$

where  $\hat{P}_{NL}^{(SHG)}$  is the frequency-domain nonlinear polarization for second-harmonic generation, equal to the Fourier transform of  $(1/2)P_{NL}^{(3)}$  given in Eq. (2.10).

Defining the frequency-domain field envelope as

$$\hat{A}_j(z, \Omega_j) = \hat{E}_j(z, \omega) \exp[(ik(\omega_j + \Omega_j))z], \quad (2.32)$$

the frequency-domain nonlinear polarization is

$$\begin{aligned} \hat{P}_{NL}^{(SHG)}(z, \Omega_2) &= \epsilon_0 d(z) \int_{-\infty}^{\infty} \hat{A}_1(z, \Omega') \hat{A}_1(z, \Omega_2 - \Omega') \\ &\times \exp \{ -i [k(\omega_1 + \Omega') + k(\omega_1 + \Omega_2 - \Omega')] z \} dz \end{aligned} \quad (2.33)$$

Substituting Eqs. (2.32) and (2.33) into Eq. (2.31), the solution for the second-harmonic frequency-domain envelope in the limit of slowly varying envelopes at the output of a crystal of length  $L$  including group-velocity mismatch, but neglecting group-velocity dispersion, is written as

$$\hat{A}_2(L, \Omega_2) = \int_{-\infty}^{\infty} \hat{A}_1(0, \Omega') \hat{A}_1(0, \Omega_2 - \Omega') \hat{d}(\Delta k) d\Omega', \quad (2.34)$$

where  $\hat{d}(\Delta k)$  is proportional to the Fourier Transform of the nonlinear coefficient distribution  $d(z)$ , and is given by

$$\hat{d}(\Delta k) = -i \frac{2\pi}{\lambda_1 n_2} \int_{-\infty}^{\infty} d(z) \exp(-i\Delta k z) dz. \quad (2.35)$$

The wavevector mismatch  $\Delta k$  is frequency dependent and can be expanded around the deviation from the SH carrier frequency such that

$$\Delta k \approx \Delta k_0 + \delta\nu\Omega_2. \quad (2.36)$$

Substitution of Eqs. (2.36) and (2.35) into Eq. (2.34) results in a simple transfer function relation for the frequency-domain SH field at the output of a general QPM-SHG device:

$$\hat{A}_2(L, \Omega_2) = \hat{D}(\Omega_2) \hat{A}_1^2(\Omega_2), \quad (2.37)$$

where  $\hat{A}_1^2(\Omega_2)$  is the Fourier-Transform of the square of the input FH field, or equivalently, the self-convolution of the frequency-domain envelope:

$$\hat{A}_1^2(\Omega_2) = \int_{-\infty}^{\infty} \hat{A}_1(0, \Omega') \hat{A}_1(0, \Omega_2 - \Omega') d\Omega'. \quad (2.38)$$

The SHG transfer function  $\hat{D}(\Omega)$  is the Fourier transform of the nonlinear coefficient

distribution:

$$\hat{D}(\Omega) = -i \frac{2\pi}{n_2 \lambda_1} \int_{-\infty}^{\infty} d(z) \exp[-i(\Delta k_0 + \delta\nu\Omega)z] dz. \quad (2.39)$$

If the nonlinear coefficient distribution  $d(z)$  is uniform and periodic, as in Eq. (2.17), with a grating wavevector of magnitude  $K_g = \Delta k_0$  such that the interaction at the carrier frequencies is quasi-phase-matched, then the transfer function takes the familiar  $\sin(x)/x$  form, with  $x = \delta\nu\Omega L/2$ . With a CW first-harmonic input, the FH frequency-domain envelope is proportional to the Dirac delta function:  $\hat{A}_1(0, \Omega) \propto \delta(\Omega)$ . On substitution into Eqs. (2.38) and (2.37) we find that the SH frequency domain amplitude is proportional to the the SHG transfer function  $\hat{D}(\Omega)$ . The SHG transfer function is identical to the frequency-dependent tuning curve shown in Fig. 1.5 for a uniform nonlinear crystal.

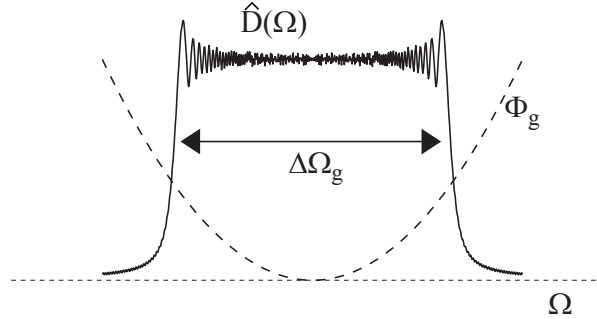


Figure 2.1: SHG transfer function of a strongly-chirped QPM grating. The amplitude function takes the form of a Fresnel integral with bandwidth  $\Delta\Omega_g \approx 2D_g L/\delta\nu$ . The phase of the chirped-grating SHG transfer function,  $\Phi_g(\Omega) = \delta\nu^2\Omega^2/4D_g$ , is predominantly quadratic and determined by the grating chirp  $D_g$ .

Through manipulation of the local QPM period and/or duty-cycle,  $d(z)$  may take nearly arbitrary functional form. From Eq. (2.39) the frequency-domain transfer function may be engineered through design of the nonlinear coefficient distribution. To illustrate the engineering capability in this concept, we examine one particularly

interesting case: that of a linearly chirped QPM grating with optimum duty cycle (50% for a first-order QPM grating), where

$$d(z) \approx d_m \exp [i (K_0 + 2D_g z) z], \quad (2.40)$$

and the local grating vector has magnitude  $K_g(z) = K_0 + 2D_g z$  which is set by a  $z$ -dependent QPM period  $\Lambda(z) = 2\pi/K_g(z)$ . The transfer function for a strongly-chirped grating ( $D_g L^2 \gg 1$ ) has the functional form shown in Fig. 2.1; such that  $\hat{D}(\Omega)$  has approximately flat amplitude over a bandwidth  $\Delta\Omega_g = 2D_g L/\delta\nu$ , and quadratic phase  $\Phi_g(\Omega) = \delta\nu^2 \Omega^2/4D_g$ , such that the transfer function is approximated as

$$\hat{D}(\Omega) \approx \frac{2\pi}{n_2 \lambda_1} |d_m| \sqrt{\frac{\pi}{D_g}} \exp \left( -i \frac{\delta\nu^2 \Omega^2}{4D_g} \right) \quad (2.41)$$

for  $|\Omega| < \Delta\Omega_g/2$ .

This example demonstrates that longitudinally non-uniform patterning of QPM-nonlinear devices allows engineering of the bandwidth of nonlinear devices [25, 22]; as well as engineering of the phase response, which enables the compression of chirped FH pulses during SHG in devices much longer than  $L_g$  [19, 20]. In Chapter 3 we demonstrate the use of transverse patterning to produce a QPM-SHG device with a tunable phase response, allowing for tunable compensation of dispersion and the ability to completely compress chirped FH pulses over a range of chirp values. We also discuss the engineered bandwidth in more detail in Chapter 4, where we compare this technique for broadband SHG to the use of tilted pulse-fronts for matching the group-velocities of interacting waves.

Similar frequency-response engineering can be used even when group-velocity dispersion is present in a nonlinear material[57], or extended to optical parametric amplification [30]. For a more thorough discussion of QPM-SHG pulse compression, see Refs. [49] and [32]. A general theory of non-uniform QPM devices has also been presented for SHG and DFG interactions, allowing nearly arbitrary engineering of the amplitude and phase response in a QPM device through manipulation of the local period and duty-cycle of a QPM grating function[23, 58].

## 2.7 Monochromatic three-wave mixing and diffraction: the soliton regime

Simply put, spatial solitons are solutions to the wave equation for which the electric field amplitude does not change with propagation over distances which are long compared to both the characteristic diffraction length  $L_{R,j}$  and the nonlinear mixing length  $L_G$ , such that

$$\frac{\partial}{\partial z} |B_j(\mathbf{r}, z)| = 0. \quad (2.42)$$

In Chapter 5 we discuss the engineering of soliton states with chirped QPM gratings for more efficient parametric amplification. In order to more clearly see how solitons may be useful for improving the efficiency of a parametric amplifier it is important to understand the nature of spatial solitons in three-wave mixing. In this section, we review the physical and mathematical properties of solitons in quadratic nonlinear interactions.

Continuous-wave three-wave mixing in a second-order nonlinear medium is represented by the following coupled equations in the limit of paraxial waves (see Eqs. 2.14 through 2.16):

$$-2ik_1 \frac{\partial B_1}{\partial z} + \nabla_{\perp}^2 B_1 + E_0 K_1 B_2^* B_3 \exp(i\Delta k z) = 0 \quad (2.43)$$

$$-2ik_2 \frac{\partial B_2}{\partial z} + \nabla_{\perp}^2 B_2 + E_0 K_2 B_1^* B_3 \exp(i\Delta k z) = 0 \quad (2.44)$$

$$-2ik_3 \frac{\partial B_3}{\partial z} + \nabla_{\perp}^2 B_3 + E_0 K_3 B_1 B_2 \exp(-i\Delta k z) = 0 \quad (2.45)$$

We notice that there are three terms in each of the above equations. The first is the propagation term, a  $z$ -dependent derivative. The second is a diffractive term, which leads to beam spreading on propagation due to the wave nature of light. The third is a nonlinear term, describing the nonlinear coupling between waves. In cascaded interactions (when signal, idler, and pump waves have comparable magnitudes and the coupling between them is strong, i.e.  $L_G \leq L$ ), nonlinear mixing can result in significant beam-narrowing or self-focusing effects.

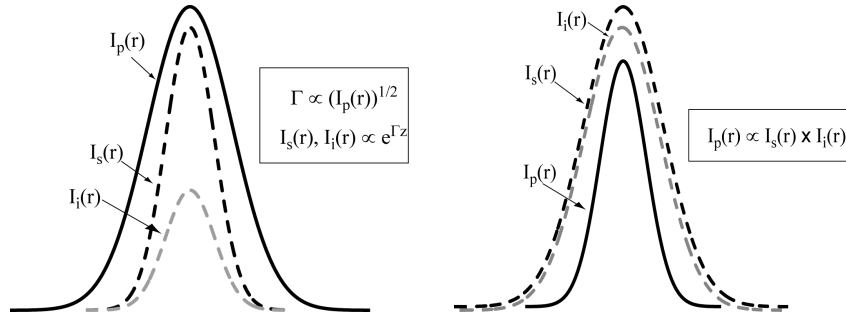


Figure 2.2: Beam narrowing in nonlinear frequency conversion. LEFT: OPA results in signal, idler radial intensity envelopes that are narrower than the pump beam due to the exponential nature of parametric amplification. RIGHT: Sum frequency generation, the back-conversion process in parametric amplification, results in a pump beam that is narrower than both the signal and idler since the pump intensity is proportional to the product of signal and idler intensities.

Nonlinear self focusing is diagrammed in Fig. 2.2. Section 2.5 showed that in the high-gain limit signal and idler intensities are exponential in the pump field amplitude. If the pump intensity is radially dependent, then the generated signal and amplified idler are therefore narrower than the pump in a high gain system. In fact, even for low gain OPA (difference frequency generation), the nonlinear nature of three-wave mixing suggests that the generated idler and amplified signal will be narrowed by the radially varying pump. The back-conversion process (sum frequency generation) also results in beam narrowing effects, since the generated pump intensity is proportional to the product of signal and idler intensities.

The simplified description of beam narrowing illustrated in Fig. 2.2 does not completely describe the three-wave mixing process since it ignores the diffractive terms in Eqs. (2.43) through (2.45). Nevertheless, it illustrates that nonlinear frequency mixing results in beam-narrowing effects. Diffraction acts to cause beam spreading, and a stable equilibrium with no such spreading or focusing may result when these two effects are perfectly balanced, resulting in field envelopes which satisfy Eq. (2.42). Such conditions are met approximately when the characteristic length for frequency mixing is approximately equal to the characteristic length for diffraction:  $L_G \approx L_{R,3}$ .

For a more mathematical description, we return to the coupled equations (Eqs. (2.43) through (2.45)). It is convenient to normalize the propagation coordinate to the characteristic diffraction length  $L_{R,3}$ . The interaction length is typically much longer than this characteristic length scale which determines the dynamics of soliton formation. In addition, we normalize the field amplitudes not to the peak amplitude, but so that the coupling constants for the normalized fields are of unit magnitude.

With a spot size ( $1/e$  intensity radius) defined as  $r_0$ , we normalize the propagation distance to the diffraction length  $L_{R,3} = k_3 r_0^2$  of a Gaussian pump beam with width  $r_0$ . Since solitons represent non-diffracting solutions, this characteristic length is better termed the soliton length, and denoted as  $Z_R$  such that the normalized propagation distance is  $\xi = z/Z_R$ . Radial distance is normalized to  $r_0$  such that the normalized transverse Laplacian operator is  $\bar{\nabla}_\perp^2 = r_0^2 \nabla_\perp^2$  with normalized radial distance  $\bar{r} = r/r_0$ .

The field envelopes are also normalized according to

$$B_i = \frac{1}{E_0 r_0^2} \sqrt{\frac{K_i}{K_1 K_2 K_3}} a_i \quad (2.46)$$

and  $\sigma_i = 2k_i/k_3$ , such that the coupled equations may be written as

$$-i\sigma_1 \frac{\partial a_1}{\partial \xi} + \bar{\nabla}_\perp^2 a_1 + a_2^* a_3 \exp i\bar{\Delta}k\xi = 0 \quad (2.47)$$

$$-i\sigma_2 \frac{\partial a_2}{\partial \xi} + \bar{\nabla}_\perp^2 a_2 + a_1^* a_3 \exp i\bar{\Delta}k\xi = 0 \quad (2.48)$$

$$-i\sigma_3 \frac{\partial a_3}{\partial \xi} + \bar{\nabla}_\perp^2 a_3 + a_1 a_2 \exp -i\bar{\Delta}k\xi = 0, \quad (2.49)$$

where the normalized wavevector mismatch is defined as  $\bar{\Delta}k = \Delta k Z_R$ . With the approximation  $\sigma_i = 2k_i/k_3 \approx 2\omega_i/\omega_3$  (valid in the limit of small dispersion, or near-degenerate operation), the normalized power in each wave can be defined as

$$\bar{P}_i = \int_0^\infty \sigma_i^2 |a_i|^2 d^2\bar{r} = \frac{32d_m^2 \omega_1^2 \omega_2^2 r_0^2 n_i}{\varepsilon_0 c^5 n_3^2} P_i \quad (2.50)$$

where  $\bar{r} = r/r_0$  is the normalized radial distance, and  $P_i$  is the optical power at frequency  $\omega_i$ .

Quadratic spatial solitons (also called similtions) are multiple-frequency stationary solutions to the above coupled wave equations. The solutions and their properties may be computed numerically or approximated with a variational technique[59, 60, 61, 62, 63]. Solitons exist when the parametric gain length  $L_G$  and the Rayleigh length  $L_{R,3}$  are approximately equal. Soliton solutions for the electric field are the products of a (real) amplitude function which depends only on the radius and a  $\xi$ -dependent phase function:

$$a_i(\xi, \rho) = a_i^0(\rho) e^{-iq_i \xi} \quad (2.51)$$

where  $a_i^0(\rho)$  is a bell-shaped (for the zero-order bright solitons) field amplitude function depending only on  $\bar{r} = r/r_0$ , and  $q_i$  is a nonlinear propagation constant. The propagation constant of the pump wave  $q_3$  is related to that of the signal and idler

waves through

$$q_3 = q_1 + q_2 + \bar{\Delta}k. \quad (2.52)$$

With given values of the wavevector ratios  $\sigma_i$ , the field envelopes  $a_i(\xi, \rho)$  are determined uniquely by the normalized wavevector mismatch  $\bar{\Delta}k$ , the difference in photon number of signal and idler fields (usually approximated as zero in a high-gain parametric amplifier), and the soliton radius. The soliton radius may be exchanged for the total soliton power in this three-parameter model as they are related to each other. For more complete discussions of the properties of CW spatial solitons, see Refs. [60], [62], and [64].

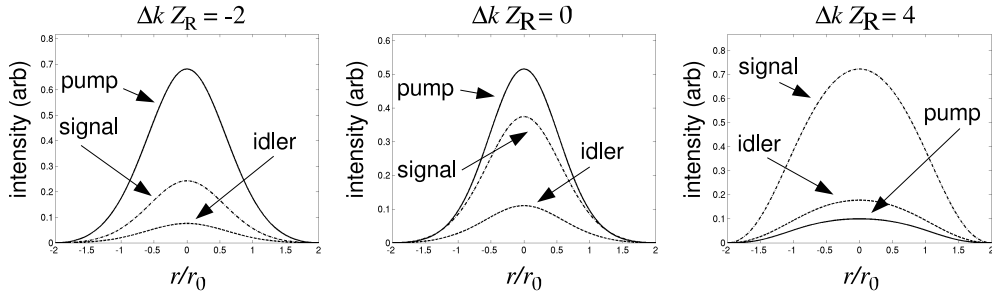


Figure 2.3: Three-wave soliton field envelopes for several different values of the normalized wavevector mismatch. From left to right, the normalized wavevector mismatch is  $\Delta k Z_R = -2, 0, 4$ . Note the marked change in relative intensity of pump, signal, and idler as  $\Delta k$  changes. These plots were created assuming  $\sigma_1 \approx 1.36$  ( $\sigma_2 \approx 2 - \sigma_1 = 0.64$ ).

If  $\sigma_1 \approx 1.36$  ( $\sigma_2 \approx 2 - \sigma_1 = 0.64$ ), (appropriate for a signal wavelength of 1550 nm and a pump wavelength of 1064 nm), the total normalized power of a soliton at  $\Delta k = 0$  is  $P_{norm,tot} = \sum_i P_{norm,i} \approx 212$ . This number changes slightly for different values of

$\sigma_1$ . Relating this soliton power to Eq. (2.50) results in an important scaling relation for multi-color solitons: the product of the total power and the square of the soliton radius  $r_0$  is constant for a fixed set of interacting frequencies at  $\Delta k = 0$ . Calculated soliton fields at  $P_{norm,tot} = \sum_i P_{norm,i} \approx 212$  for different values of the normalized wavevector mismatch are plotted in Fig. 2.3.

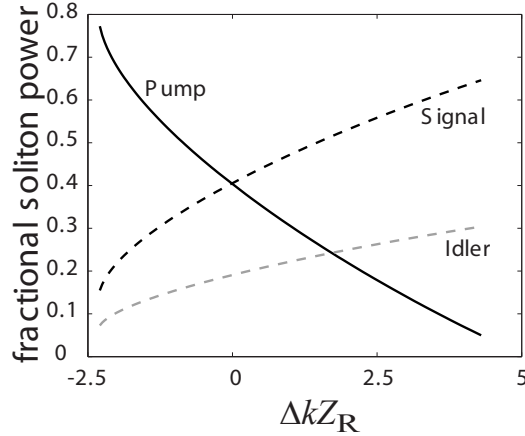


Figure 2.4: Fraction of total soliton power carried in each of the component (signal, idler, and pump) waves in CW quadratic spatial soliton solutions versus normalized wavevector mismatch, assuming  $\sigma_1 = 1.36$  ( $\sigma_2 = 0.64$ ). The wavevector mismatch  $\Delta k$  is normalized to  $Z_R = k_3 r_0^2$  where  $r_0$  is defined as the  $1/e$  intensity radius of the pump wave for the soliton at  $\Delta k = 0$ . In our experiment,  $r_0 = 20 \mu\text{m}$  so that with a pump wavelength of 1064 nm  $Z_R = 5$  mm.

Solitons exist for values of  $\bar{\Delta k}$  approximately between -2.5 and 5, and the balance of power between signal, idler, and pump waves changes, as shown in Fig. 2.4, as  $\bar{\Delta k} = \Delta k Z_R$  is varied. Solitons may be excited through frequency up-conversion (sum-frequency generation or second-harmonic generation), or frequency down-conversion (seeded parametric amplification, or spontaneous parametric generation). In Chapter 5 we discuss in more detail the influence of wavevector mismatch on the properties of spatial solitons, which holds promise for the tailoring of solitons for increased efficiency in parametric amplification.

A more complete discussion of the simple physics of solitons in nonlinear interactions is found in Ref. [64], and a comprehensive overview of recent research in this

field is given in Ref. [65].

## 2.8 Summary of Chapter 2

In this chapter, we have discussed some of the basic theory of three-wave mixing in second-order nonlinear interactions. Nonlinear polarization in the equation that describes electromagnetic wave propagation results in coupling between electric fields at different frequencies. In Section 2.2 we derived the coupled wave equations that describe the evolution of electric field envelopes at different interaction frequencies, taking into consideration effects of dispersion (GVM and GVD) and diffraction in addition to nonlinear frequency mixing. In Section 2.3 we cast these coupled wave equations in terms of characteristic lengths for the effects of GVD, GVM, diffraction, and nonlinear mixing. In this form, terms in the differential equations may be dropped when the associated characteristic length is much larger than the interaction length.

Several examples were discussed in detail. In Sections 2.4 and 2.5 we discussed SHG and OPA in the limit of plane monochromatic waves. Simple solutions give some insight into scaling of these effects, as well as define the limit when pump depletion may be neglected.

In Section 2.6 we discussed the transfer function interpretation of ultrafast SHG. This concept will be useful in Chapters 3 and 4 as we discuss QPM engineering techniques to manipulate the phase and amplitude response of frequency conversion devices.

In Section 2.7 we discussed the properties of spatial solitons in three-wave mixing: that when the CW coupled equations are driven to the cascading limit, self-focusing effects can balance diffraction resulting in stable spatial field envelopes which propagate without change in amplitude. Spatial solitons are discussed in more detail in Chapter 5 where we discuss the tailoring of soliton states with chirped QPM gratings in order to achieve more efficient parametric amplification. In Chapter 6 we discuss the effects of parametric noise on soliton generation and propagation, which explains data presented in Chapter 5 that is not consistent with a CW model.

# Chapter 3

## Tunable-chirp pulse compression in quasi-phase-matched second harmonic generation

### 3.1 Introduction

Shaping of the temporal profile of optical pulses is an important tool for ultrafast optics. Longitudinally nonuniform patterning of QPM devices has been used to demonstrate impressive flexibility in designing the frequency response of nonlinear frequency conversion devices – not only for producing broad-bandwidth frequency conversion, but also to take advantage of the frequency-dependent phase of the SHG transfer function discussed in Section 2.6. Recently, linearly-chirped gratings in quasi-phase-matched (QPM) nonlinear media have been demonstrated as a means for compensating the quadratic [19, 66, 19] and higher-order phases [29, 67] of chirped optical pulses during second harmonic generation (SHG). More generally, theory has been presented demonstrating the potential for nearly arbitrary engineering of the amplitude and phase of short optical pulses with proper variation of the period and duty-cycle of aperiodic QPM gratings during SHG [23, 57] and difference-frequency generation (DFG) [58].

Experiments with longitudinally patterned crystals have shown QPM devices to

have the advantages of a compact monolithic design with no critical alignment necessary, but have the disadvantage of a fixed set of grating parameters with no continuous adjustability. Previously, fanned gratings have been demonstrated to provide continuous tuning of the QPM period in a periodically poled lithium niobate (PPLN) optical parametric oscillator[16]. Here, we demonstrate the fanned QPM grating as a means of achieving continuous tunability of grating chirp during QPM SHG pulse compression, specifically the compression of 140-fs-long  $1.554\text{-}\mu\text{m}$  pulses stretched up to 8 ps-long to near-transform-limited 140-fs-pulses at 777 nm. Using a chirped PPLN QPM grating with grating chirp tunable from  $0.36\text{ mm}^{-2}$  to  $0.21\text{ mm}^{-2}$ , capable of compensating FH pulse chirps from  $-0.271\text{ ps}^2$  to  $-0.464\text{ ps}^2$ , we demonstrate pulse compression at a ratio (first harmonic pulsewidth to second harmonic pulsewidth) of 63, and the capability to achieve ratios between 50 and 90 with our single tunable device.

## 3.2 Tunable SHG pulse compression with fanned QPM gratings

While the use of a fanned grating is directly applicable to tuning more complicated grating structures, and in other second-order nonlinear interactions such as DFG, the experiment in this chapter is restricted to pulse compression in QPM SHG. Theory for QPM-SHG pulse compression has been described in detail in Refs. [23, 32], here we summarize pertinent results of that work.

The effective group velocity dispersion (GVD) in a QPM pulse shaping device is the result of the interplay between the mismatch in group velocities of the FH and SH fields, and the spatial localization of the conversion of different frequency components at different locations in the QPM device. In general, for a chirped QPM grating the maximum achievable group delay between FH and SH envelopes,  $\tau_g = \delta\nu L$ , (where  $\delta\nu$  is the group velocity mismatch (GVM) parameter  $\delta\nu = (u_1^{-1} - u_2^{-1})$ , and  $u_1$  and  $u_2$  are the group velocities of the FH and SH fields, and  $L$  is the interaction length) determines the longest chirped pulse that can be compressed with a given device. For

a 5-cm-long PPLN grating designed for QPM SHG at a wavelength of  $1.55 \mu\text{m}$  ( $\delta\nu = 0.31 \text{ ps/mm}$ ), this maximum group delay is 15 ps.

The local grating  $k$ -vector for a linearly-chirped QPM device is

$$K_g(z) = K_m + 2D_g z \quad (3.1)$$

where  $K_m$  is set by the phase-matching condition,  $K_m = \Delta k_0$  with  $\Delta k_0 = 2k_1 - k_2$ , and  $z$  is the propagation direction;  $D_g$  is the grating chirp parameter, and the local QPM period is  $\Lambda(z) = 2\pi/K_g(z)$ . A properly designed QPM-SHG pulse compression device has an SHG bandwidth of  $\Delta\Omega_g = |2D_g L/\delta\nu|$  chosen to be roughly 3 times the FH bandwidth so as to reduce the effects of bandwidth truncation[23].

Consider a chirped FH pulse, with chirp parameter  $C_1 = \partial^2\Phi_1/\partial\omega^2$  evaluated at the FH carrier frequency  $\omega_1$ , where  $\Phi_1$  is the FH frequency-domain phase function. For a linearly chirped FH pulse the frequency-domain phase function is quadratic,  $\Phi_1 = (1/2)C_1\Omega_1^2$ . (Components of the frequency-domain phase that are linear in  $\Omega_1$  can generally be ignored as they simply represent a linear group delay in the time domain.) The effect of the chirped QPM grating in SHG results in the following chirp parameter which describes the quadratic phase of the SH pulse:

$$C_2 = \frac{1}{2} \left( C_1 + \frac{\delta\nu^2}{D_g} \right). \quad (3.2)$$

The SH chirp parameter  $C_2$  can be calculated knowing the quadratic phase of the FH envelope characterized by  $C_1$  and the chirped-grating transfer function, given in Eq. (2.41). The result is zero SH chirp when the chirp of the QPM grating is matched to the chirp of the FH field:  $D_g = -\delta\nu^2/C_1$ , indicating a transform-limited SH pulse and complete pulse compression. For a more thorough discussion of QPM SHG pulse compression, see Ref. [23].

A schematic of the fanned chirped grating design is shown in Fig. 3.1. At one edge of the sample, the grating  $k$ -vector is patterned with chirp  $D_a$ , and at the other edge the chirp is  $D_b$ . The domains are simply connected from one side of the device to the other, so that the grating chirp as a function of lateral position  $x$  is the weighted

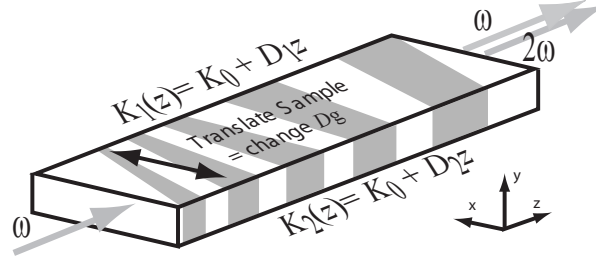


Figure 3.1: Fanned QPM-SHG pulse-compression grating. Translation of the sample transverse ( $x$ ) to the direction of propagation ( $z$ ) produces continuous tuning of the grating chirp.

average of the two defined chirps:

$$D_g(x) = \left(\frac{1}{2} - \frac{x}{W}\right) D_a + \left(\frac{1}{2} + \frac{x}{W}\right) D_b, \quad (3.3)$$

where  $W$  is the sample width, and  $x$  is defined as zero in the center of the sample. In this manner, translation of the sample offers continuous tuning of  $D_g$  from  $D_a$  to  $D_b$ . Note that propagating through the sample in the reverse direction reverses the sign of the grating chirp, enabling continuous tuning from  $-D_a$  to  $-D_b$  as well, with the same device.

While the grating chirp at the ends of the sample ( $x = \pm W/2$ ) is defined to be strictly linear, this is not in general true for all lateral positions  $x$ . Because of the geometry of our design it is the period, and not the  $k$ -vector that is a weighted average of that at the  $x = \pm W/2$  ends of the device. The next-order phase contribution can be calculated from the design geometry; the higher-order phase should be less than  $\pi/2$  for all positions  $y$  and all domains along the sample length to minimize the importance of the resultant higher-order phase on the SH pulse. This requirement

imposes the following constraint on the chirp tuning range:

$$(D_a - D_b)^2 < \frac{24\pi^2}{\Lambda_0 L^3}. \quad (3.4)$$

It should be noted that modified design geometries with slightly curved domain walls can eliminate the higher-order phase contribution.

Eq. (3.4) in turn restricts the maximum fan angle (relative to the crystal axis) to less than  $\phi_{max} = (3\Lambda_0 L/8W^2)^{1/2}$ ; limiting the fan angle for our devices ( $L = 4.7$  cm,  $W = 1$  cm,  $\Lambda_0 = 18.6$   $\mu\text{m}$ ) to less than 4 degrees. However, in practice fabrication proves to be a tighter angular constraint in congruent PPLN using current fabrication techniques. Because the domain walls have a preferred orientation along the crystallographic  $y$ -axis (the laboratory  $x$ -axis, as drawn in Fig. 3.1), additional domain spreading results for patterns fabricated with other orientations, requiring the use of correspondingly narrowed poling electrodes to maintain the desired 50% duty cycle. Although fanned domains have been demonstrated up to angles of 20 degrees[68], we found experimentally that beyond 2 degrees it becomes difficult to maintain the desired duty cycle for QPM gratings with periods near 19  $\mu\text{m}$  in congruent lithium niobate.

### 3.3 Experimental Results

Experiments were carried out to demonstrate QPM-SHG tunable pulse compression at a FH wavelength of 1.554  $\mu\text{m}$  with a PPLN grating measuring 4.7-cm long and 1-cm wide, and a nominal QPM period  $\Lambda_0 = 18.6$   $\mu\text{m}$ . The grating length is chosen according to guidelines in Ref. [23] so that the grating bandwidth is roughly three times the  $1/e$  spectral width of the pulse. Grating chirps range from  $D_a = 0.21$   $\text{mm}^{-2}$  (QPM periods between 18.1  $\mu\text{m}$  and 19.2  $\mu\text{m}$ ) to  $D_b = 0.36$   $\text{mm}^{-2}$  (QPM periods between 17.8  $\mu\text{m}$  and 19.7  $\mu\text{m}$ ). With a GVM parameter of  $\delta\nu = 0.31$  ps/mm, this implies the QPM grating is capable of compensating FH pulse chirps ranging from -0.46  $\text{ps}^2$  to -0.27  $\text{ps}^2$ .

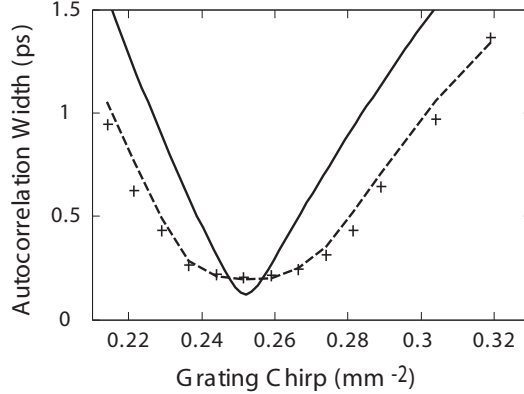


Figure 3.2: Tuning behavior of fanned grating device. Measured autocorrelation width is plotted (crosses) versus grating chirp. Calculated theoretical curves are plotted for comparison; the solid line is calculated for a FH pulse with only quadratic phase, while the dotted line includes the cubic phase calculated for the grating-pair stretcher used in our experiment.

Transform-limited pulses 140 fs (intensity FWHM) in duration, at a carrier wavelength of 1.554  $\mu\text{m}$  from a Spectra-Physics OPAL synchronously-pumped optical parametric oscillator are chirped by double-passing a grating pair pulse stretcher in the Treacy configuration[69] to 8.2 ps ( $C_1 = -0.375 \text{ ps}^2$ ) FWHM duration. The spectrum and autocorrelation of the FH pulses are measured after the pulse stretcher. The FH autocorrelation measures 12.7 ps in duration, and the bandwidth is measured to support 140 fs FH pulses, and so is capable of generating SH pulses as short as 100 fs at the transform-limit for the approximately Gaussian pulse shape. The resultant 1 nJ pulses are then focused into the PPLN crystal which is housed in a temperature-controlled oven held at 120 C. The average power of both the FH and SH beams are measured after the PPLN sample, as well as the autocorrelation and the power spectrum of the SH field.

The tuning behavior is shown in Fig. 3.2. The dotted theoretical curve is calculated including the second and third-order dispersion ( $C_{cubic} = \partial^3\Phi_1/\partial\omega^3$  has a value of  $1.5 \times 10^{-3} \text{ ps}^3$ ) for the grating-pair pulse stretcher[70], showing good agreement between theory and experiment.

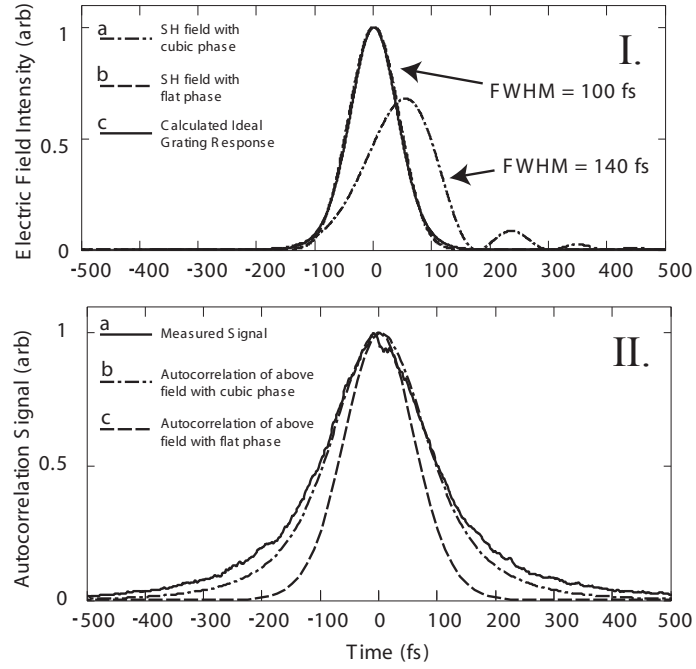


Figure 3.3: Electric field amplitude and autocorrelation from fanned grating device, reconstructed using the measured power spectrum with calculated spectral phase functions. Top: The ideal grating response (solid) would compensate both the quadratic and cubic phases that result from a grating pair stretcher, resulting in a time-domain electric field with flat phase (dashed). Our fanned grating device was not designed to correct the cubic phase, resulting in a longer-than-transform-limited pulse (dash-dot). Bottom: The measured autocorrelation (solid) is compared with the calculated autocorrelation assuming cubic phase (dash-dot) and with flat phase (dash).

Electric-field envelopes calculated using the measured power spectrum and the calculated spectral-phase function are shown in Fig. 3.3. Fig. 3.3 shows that the calculated uncompensated cubic spectral phase from the grating-pair stretcher, when applied to the measured SH power spectrum, results in an autocorrelation trace that matches well to our experimental data.

This PPLN device is designed with a linearly chirped grating, and therefore compensates only the linear chirp (quadratic phase) of the FH pulse. The minimum autocorrelation width is 200 fs; 1.4 times the autocorrelation width of 140 fs for transform-limited pulses. A simple modification of the grating design from the linear chirp given in Eq. (3.1) to

$$K_g(z) = 2\pi/\Lambda(z) = K_m + 2D_g z + 3Gz^2 \quad (3.5)$$

which would allow complete compensation of the cubic phase as well, a significant advantage of QPM designs[29, 67]. In order to compensate a cubic phase (assumed here much less than the quadratic phase component),  $G$  should be chosen such that  $G = C_{cubic}\delta\nu^3/3C_1^3$ . Appropriately chosen  $G_a$  and  $G_b$  coefficients would lead to the construction of a tunable grating design analogous to Eq. 3.3 where the linear and quadratic grating chirp tune together.

The experiment was conducted with confocal focusing ( $w_0 = 75 \mu\text{m}$ ). Power-normalized conversion efficiency ( $U_1/U_2^2$ , where  $U_1$  and  $U_2$  are the pulses energies of the FH and SH fields, respectively) is observed to be 0.97 %/nJ (pulse energies  $U_1 = 0.88 \text{ nJ}$ ,  $U_2 = 7.58 \text{ pJ}$ ). Ref. [23] predicts the conversion efficiency for a chirped QPM PPLN device to be  $0.59(\tau_0/\tau_1)\eta_0$ , where  $\eta_0$  (162 %/nJ at a FH wavelength of  $1.55 \mu\text{m}$ ) is the efficiency for an unchirped FH pulse and a uniform grating at the optimum length of  $2\tau_0/\delta\nu$ . Our measured efficiency is 63 % of the calculated theoretical value of 1.54 % / nJ.

### 3.4 Summary of Chapter 3

In this chapter, we have demonstrated QPM-SHG pulse compression with tunable dispersion through the use of a fanned grating design. This demonstrates how the engineered transfer function of a longitudinally patterned QPM device can be made tunable through combination with lateral patterning of QPM domains. The demonstrated compression ratio of 63 (variable between 50 and 90) with our stretcher and QPM-SHG compressor can be improved with a slight modification of the QPM design to include cubic phase, easily achievable with standard lithographic processing. Straightforward extension of this method to implement tunable general pulse shaping in QPM SHG [23] and QPM DFG [58] is possible.

# Chapter 4

## Group-velocity mismatch compensation in quasi-phase-matched second-harmonic generation of pulses with spectral angular dispersion

### 4.1 Introduction

Laser gain media capable of short pulse generation are available over only a small portion of the optical spectrum, while applications from spectroscopy to high-field science and optical communications often require pulses in inaccessible spectral regions. Nonlinear frequency conversion of short pulses can fill these spectral regions. To preserve the short pulse duration, the acceptance bandwidth of a nonlinear interaction must match or exceed the bandwidth of the input pulse. In this chapter, we discuss how the combination of spectral angular dispersion with noncollinear SHG in

a tilted QPM grating can result in a broadened acceptance bandwidth compared to collinear SHG in a uniform crystal of the same length. This technique will be compared with the alternative technique of collinear QPM SHG with aperiodic gratings which may also be designed with broad acceptance bandwidths.

In addition to a broad bandwidth, high conversion efficiency is also desired. The conversion efficiency of conventional collinear SHG in uniform nonlinear materials is proportional to the square of the interaction length, but the bandwidth is inversely proportional to the same interaction length, resulting in a trade-off between conversion efficiency and bandwidth. Several methods have been demonstrated to reduce or eliminate this trade-off. In this chapter we also present theoretical calculations of the conversion efficiency for noncollinear SHG with spectral angular dispersion, and compare the results to other known techniques for ultrafast frequency conversion.

In the simplest collinear interactions (type 0 quasi-phase-matched SHG or type I and type II birefringent phase-matched SHG), the bandwidth of SHG is limited by the difference in group velocity between the first harmonic (FH) and second harmonic (SH) wave [14, 23]. A FH wave packet travelling through a nonlinear medium will lead or lag (depending on the shape of the dispersion curve) the generated SH wave which travels at a different group velocity due to dispersion in the group index of the nonlinear medium. In a crystal longer than a walkoff length (the crystal length which results in a difference in group delay between FH and SH envelopes that is equal to the FH pulsewidth) this velocity mismatch results in a SH pulse that is significantly longer than the FH input, or in the frequency domain, has a bandwidth which is significantly narrower than the FH bandwidth. Consequently, to preserve the bandwidth of the SH wave the maximum crystal length is limited approximately to the walkoff length. A reduced mismatch between group velocities of the interacting waves results in a longer maximum interaction length[23].

Occasionally, nature provides perfect matching of the group velocities of FH and SH waves for a particular pair of frequencies in a nonlinear medium. This is not, in general, the same frequency for which the phase velocities are matched, but with quasi-phase-matching (QPM) it is often possible to simultaneously quasi-phase-match and group-velocity match an SHG interaction at a particular FH frequency in a given

nonlinear material. For example, in lithium niobate, the FH and SH group velocities are matched in a type 0 ( $e + e \rightarrow e$ ) interaction at a FH wavelength near  $2.6 \mu\text{m}$  [71]. This method for group-velocity matching is available only at specific frequencies determined by the dispersion of the nonlinear material, and may not be generally applicable across the material's transparency window. Nevertheless, group-velocity-matched second-harmonic generation has been demonstrated in a variety of materials utilizing both birefringent phase-matching and quasi-phase-matching.[33, 34, 35, 36, 37, 38].

A more general technique for broadband SHG has been demonstrated through longitudinal patterning of a QPM grating, as discussed in the previous chapter[25, 19]. Longitudinal variation of the QPM period provides for localized conversion of the different frequency components of a short pulse at different positions along the propagation axis of a nonlinear device. A distribution of QPM periods allows for a broader distribution of phase-matched frequencies and an increased bandwidth compared to a uniform grating of the same length. The localized frequency conversion in the presence of a difference in group velocity between FH and SH waves results in a chirped SHG transfer function [23]. Consequently, while the SHG of a transform-limited FH pulse using a chirped QPM grating may preserve the bandwidth, the pulsewidth will not be preserved. The resulting chirped SH pulse may, however, be compressed to the transform limit using a dispersive element.

A fourth technique, the topic of this chapter, makes use of spectral angular dispersion in a non-collinear geometry to broaden the bandwidth of ultrashort-pulse SHG. In a critically phase-matched continuous-wave (CW) interaction, the phase-matching wavelength depends linearly on the angular detuning of the nonlinear crystal. Angular dispersion programs frequency-dependent angular detuning into the plane-wave components of a broadband FH field, effectively broadening the acceptance bandwidth. The idea of using spectral angular dispersion to broaden the phase-matching bandwidth was first proposed in the 1970's for broadening the bandwidth of continuous-wave SHG[39, 40, 41], and later suggested for short-pulse applications[72, 46]. Variations of this technique have been discussed theoretically[42, 43] and verified experimentally for both broadly tunable CW SHG [44, 45] and for ultrashort pulse

generation [46, 47, 48] in birefringently phase-matched nonlinear materials. Angular dispersion applied to pulsed SHG in quasi-phase-matched materials was first presented in Ref. [26], including calculations for the device configuration specific to PPLN, which we experimentally verify in Section 4.4. In addition, we expand on established theory to include a detailed discussion of the conversion efficiency and limitations imposed by diffraction and spatial walkoff.

The remainder of this chapter is devoted to the demonstration and analysis of broadband SHG of ultrashort optical pulses in the presence of spectral angular dispersion. Section 4.2 is a frequency-domain description of the technique of using spectral angular dispersion in a non-collinear geometry to compensate for material dispersion in second-harmonic generation. This technique is equivalent to the matching of the FH and SH group-velocities in the time-domain using a tilted pulse-front, as illustrated in Section 4.3. In Section 4.4 we present an experimental demonstration of broadband SHG with spectral angular dispersion. Section 4.4 demonstrates group-velocity matched SHG in periodically-poled lithium niobate (PPLN), motivating the development of a deeper theoretical understanding of the conversion efficiency in this non-collinear geometry. It is this theoretical treatment that occupies the later sections of this paper.

In Section 4.5 we derive the scalar wave equations for non-collinear second-harmonic generation assuming an undepleted pump, and including the effects of dispersion, diffraction, and spatial walkoff. In Section 4.6 we present a general solution to these equations, and in Section 4.7 we discuss the solution in the particular case of a Gaussian FH field envelope. Section 4.8 is a description of the effects that group-velocity dispersion (GVD) and spatial walkoff have on the SH field predicted by the results presented in Section 4.7. Section 4.8 presents the conversion efficiency in the limit of negligible spatial walkoff and diffractive effects, and compares the resulting expression to the efficiency for other techniques for ultrashort-pulse SHG. In Section 4.9 we discuss the scaling of conversion efficiency with regard to focusing and spatial walkoff, and trade-offs between beam quality and size and conversion efficiency that result from tight focusing and/or increased phase-matching angle. Finally, in Section 4.10 we summarize this chapter.

## 4.2 Frequency domain description

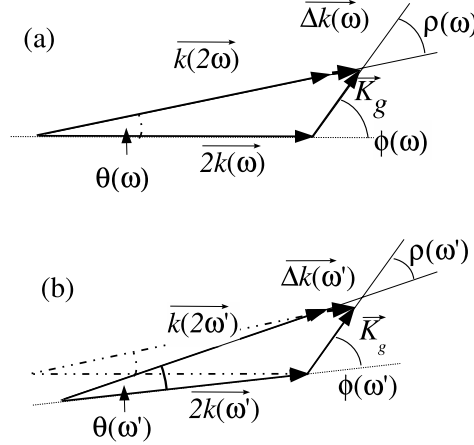


Figure 4.1: Frequency-domain picture of plane-wave non-collinear QPM-SHG. (a) Quasi-phase-matching condition at frequency  $\omega$ . (b) Quasi-phase-matching condition at frequency  $\omega'$  (solid lines), where the dotted lines indicate the QPM condition at  $\omega$ . If  $\theta'$  and  $\phi'$  are chosen appropriately,  $\Delta\mathbf{k}(\omega) = \Delta\mathbf{k}(\omega')$  and angular dispersion compensates material dispersion to maintain a constant phase mismatch for all spectral components of the pulse.

Consider a FH plane wave with wavevector  $\mathbf{k}(\omega)$  and frequency  $\omega$  generating a SH plane wave with wavevector  $\mathbf{k}(2\omega)$  and frequency  $2\omega$  inside a quasi-phase-matching grating with grating vector  $\mathbf{K}_g$ . The grating vector is in a direction normal to the QPM grating lines, and has magnitude  $K_g = 2\pi/\Lambda$  where  $\Lambda$  is the QPM period [14]. This geometry is shown schematically in Fig. 4.1. The angle  $\phi$  is measured between  $\mathbf{k}(\omega)$  and  $\mathbf{K}_g$ , and  $\theta$  is measured between  $\mathbf{k}(\omega)$  and  $\mathbf{k}(2\omega)$ . The wave-vector mismatch is defined as the vector sum  $\Delta\mathbf{k}(\omega) = 2\mathbf{k}(\omega) - \mathbf{k}(2\omega) + \mathbf{K}_g$ . The interaction is quasi-phase-matched at frequency  $\omega$  when  $\Delta\mathbf{k}(\omega) = 0$ . Quasi-phase-matching provides more flexibility than birefringent phase matching since the magnitude and direction of  $\mathbf{K}_g$  may be engineered for a variety of applications[14]. When a collinear geometry is used  $\mathbf{k}(\omega)$ ,  $\mathbf{k}(2\omega)$ , and  $\mathbf{K}_g$  are parallel vectors; quasi-phase-matching has similar engineering advantages regarding non-collinear interactions.

The magnitudes of  $\mathbf{k}(\omega)$  and  $\mathbf{k}(2\omega)$  change with frequency due to dispersion in

the refractive index of the nonlinear material. In the presence of spectral angular dispersion, the directions of the FH and SH wavevectors may also vary with frequency, and the angles  $\phi$  and  $\theta$  are frequency-dependent. If the angles  $\phi$  and  $\theta$  are appropriate functions of frequency, the spectral angular dispersion may offset the effects of material dispersion, broadening the acceptance bandwidth of a nonlinear device.

The SHG interaction is quasi-phase-matched when  $\Delta\mathbf{k}(\omega) = 0$ , or the triangle formed by the vectors  $2\mathbf{k}(\omega)$ ,  $\mathbf{k}(2\omega)$  and  $\mathbf{K}_g$  is closed. Using the law of cosines, this condition may be written as [26]

$$\cos \phi = -\frac{K_g^2 + 4[k(\omega)]^2 - [k(2\omega)]^2}{4K_g k(\omega)} \quad (4.1)$$

where  $k(\omega)$  is the magnitude of  $\mathbf{k}(\omega)$ , and similar notation is used for the SH wavevector and the QPM grating wavevector. Suppose the phase-matching condition in Eq. (4.1) is met at the FH carrier frequency  $\omega_1$  with angles  $\phi_0$  and  $\theta_0$ . Differentiating Eq. (4.1) with respect to frequency, to first order in  $\omega$ , the spectral angular dispersion required to maintain quasi-phase-matching is

$$\left. \frac{\partial \phi}{\partial \omega} \right|_{\omega_1} = \frac{\delta \nu}{k(\omega_1)\theta_0} \quad (4.2)$$

where  $\delta \nu$  is the group velocity mismatch parameter defined as

$$\delta \nu = \left. \frac{\partial k(\omega)}{\partial \omega} \right|_{\omega_1} - \left. \frac{\partial k(\omega)}{\partial \omega} \right|_{\omega_2}, \quad (4.3)$$

and we have assumed that  $\theta_0 \ll 1$  (an exact expression for all angles may be found in Ref. [26]). A similar analysis gives the resulting angular dispersion of the SH wave in this dispersion-compensated geometry

$$\left. \frac{\partial \rho}{\partial \omega} \right|_{\omega_2} = \frac{\delta \nu}{k(2\omega_1)\theta_0} \quad (4.4)$$

where  $\rho = \pi - \theta - \phi$  is the angle measured between vectors  $\mathbf{k}(2\omega)$  and  $\mathbf{K}_g$ .

### 4.3 Time domain description

In the previous section, we showed that for plane waves quasi-phase-matching can be maintained over a broad tuning range by introducing spectral angular dispersion as the frequency of a FH plane wave changes. Since an ultrashort pulse is a coherent superposition of monochromatic plane waves with a broad optical spectrum, spectral angular dispersion can also broaden the bandwidth for the SHG of a short optical pulse.

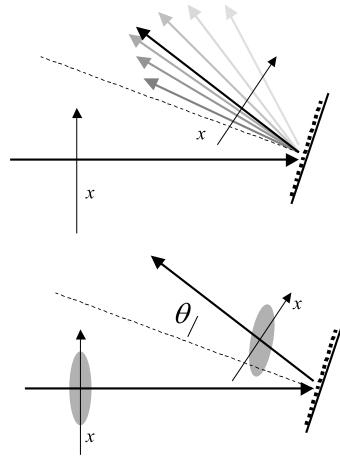


Figure 4.2: Angular dispersion and pulse-front tilt resulting from grating diffraction. TOP: Frequency-domain picture shows different frequencies dispersed in angle. BOTTOM: Time-domain picture shows the tilted pulse-front resulting from angular dispersion.

In the time domain, angular dispersion manifests itself as a tilted pulse front[73]. In order to see this more clearly, we examine the transformation that results when a field  $\hat{B}_i(x, \Omega_i)$  meets a device (e.g. reflects from a diffraction grating or passes through a prism) that disperses its frequency components in angle  $\theta$ , as shown in Fig. 4.2. Such a dispersive device results in the following transformation of the field (ignoring changes in the propagation direction of the carrier frequency):

$$\hat{B}_i(x, \Omega_i) \rightarrow \hat{B}_i(x, \Omega_i) \exp(-ik_i\theta'\Omega_i x), \quad (4.5)$$

where  $x$  is defined as the coordinate transverse to the propagation direction of the carrier frequency, and  $\theta' = \partial\theta/\partial\omega$  is the angular dispersion evaluated at the carrier frequency. The frequency-domain spatial phase is linear in  $\Omega$  and  $x$ . A spatial Fourier Transform results in a field envelope with frequency-dependent angle as represented by the transverse wavevector  $k_{x,i}$ , since the Fourier Shift Theorem applied to the right-hand side of Eq. 4.5 results in a shift in the angular components of the field that depends on the frequency  $\Omega_i$ :

$$\hat{B}_i(k_{x,i}, \Omega_i) \rightarrow \hat{B}_i(k_{x,i} + k_i\theta'\Omega_i, \Omega_i). \quad (4.6)$$

Alternatively, an inverse Fourier Transform also utilizes the Fourier Shift Theorem, resulting in a time-domain envelope with a spatially-dependent time delay shown schematically in Fig. 4.2:

$$B_i(x, t) \rightarrow B_i(x, t - k_i\theta'x). \quad (4.7)$$

The spatially-dependent time delay of the field envelope means that the pulse envelope front is tilted with respect to the propagation direction. For a more complete description of angular dispersion in ultrafast optics see Ref. [73].

Second-harmonic generation with tilted pulses for GVM compensation is shown schematically in Fig. 4.3. Consider at time  $t = 0$ , a FH field (solid outline) at the origin in the  $x - z$  plane, and propagating in the  $z$  direction. It generates some SH field (shaded gray) with approximately the same spatio-temporal envelope. After a time  $t$ , the FH field envelope has traveled a distance  $u_1t$  in the  $z$  direction, where  $u_1$  is the FH group velocity, and  $u_i$  is defined as

$$\frac{1}{u_i} = \left. \frac{\partial k}{\partial \omega} \right|_{\omega_i} \quad (4.8)$$

for the FH ( $i = 1$ ) and SH ( $i = 2$ ) fields. The SH field envelope moves a distance  $u_2t$  at a small angle  $\theta_0$  (determined by the phase matching condition) relative to the FH field direction, with  $u_2 = (\partial k_2/\partial \omega_2)^{-1}$  equal to the SH group velocity. Taking the tilt angle of the pulse front to be  $\psi$ , then the two fields have maximum overlap if  $\theta_0$  is

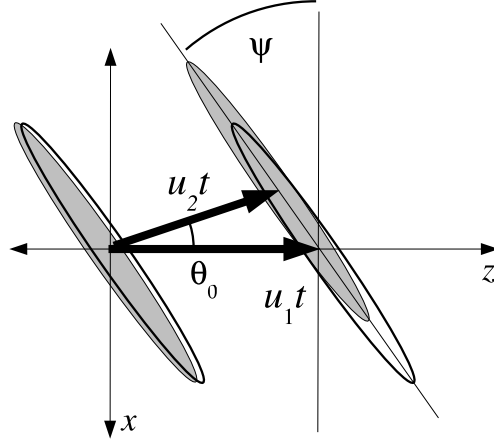


Figure 4.3: Time-domain picture of tilted pulse-front group-velocity matched second-harmonic generation. Solid outline indicates FH envelope, gray shaded area indicates SH envelope. With appropriately chosen pulse-front tilt angle  $\psi$ , the field overlap is maintained with propagation and the group velocities are effectively matched. The angle  $\psi$  is related to the spectral angular dispersion through Eq. (4.9).

chosen such that the position of the centroid of the SH field lies along the tilted pulse front of the SH field. Since the pulse front tilt is related to the angular dispersion according to [73]

$$\psi = -\arctan\left(k_1 u_1 \left.\frac{\partial\phi}{\partial\omega}\right|_{\omega_1}\right), \quad (4.9)$$

a simple geometrical analysis returns the same result as in Eq. (4.2).

## 4.4 Experiment

We demonstrate here type 0 quasi-phase-matched SHG using spectral angular dispersion to compensate for group velocity mismatch. Fig. 4.4(a) shows a schematic diagram of the experimental setup. FH radiation is incident on a diffraction grating which imposes the requisite spectral angular dispersion. The diffraction grating is then imaged into the center of a PPLN crystal so that the different frequency components of the FH field overlap in space inside the nonlinear crystal. The residual FH is dumped, and the SH is collected and re-imaged onto a second diffraction grating

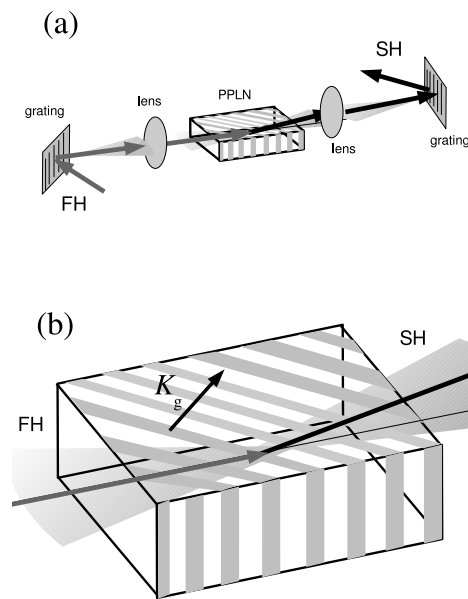


Figure 4.4: Schematic diagram of PPLN experiment with spectral angular dispersion. (a) FH light, incident on a diffraction grating acquires spectral angular dispersion. A lens images this spot into the PPLN crystal where SH light is generated. This SH is then re-imaged onto an output diffraction grating where the spectral angular dispersion is compensated. (b) A close-up view of the SHG interaction illustrating the non-collinear interaction in a tilted QPM grating.

which compensates the spectral angular dispersion of the SH light. Fig. 4.4(b) shows a more detailed view of the SHG interaction, where the poling lines of the QPM grating and the non-collinear interaction can be more clearly visualized.

This experiment uses transform-limited FH pulses 138 fs in full-width at half-maximum (FWHM) duration at a wavelength of 1550 nm in a 1-cm-long PPLN crystal, with 25 nm of FH bandwidth. At 1550 nm, the walkoff parameter has a value of  $\delta\nu = -0.314$  ps/mm, and the collinear SHG bandwidth of a 1-cm-long grating is 0.56 nm (FWHM) at the SH wavelength. The FH pulses are generated with a Spectra-Physics Opal synchronously-pumped optical parametric oscillator operating at a wavelength of 1550 nm, pumped by a Spectra-Physics Tsunami mode-locked Ti:Sapphire laser. Pulses are 0.58 nJ in energy and are delivered at a repetition frequency of 82 MHz. The FH is dispersed using a diffraction grating with 400 lines/mm at an incident angle of 21 degrees to give an angular dispersion of 1.84 rad/ $\mu\text{m}$  in free space. When the beam is imaged into the PPLN crystal with unit magnification, the angular dispersion is 0.86 rad/ $\mu\text{m}$  inside the crystal.

The PPLN crystal is 1 cm in length, with a poling period of 9.256  $\mu\text{m}$ , or 50% of the collinear phase-matching period. The duty cycle was measured to be 25.5% (as compared to the ideal 50%), resulting in an effective nonlinear coefficient[23] of 12.15 pm/V. The vector phase-matching condition requires an angle of 60.96 degrees between the FH beam and the grating wavevector. The poling lines of the PPLN device are at 60 degrees relative to the input facet, allowing near-normal incidence to the PPLN crystal. The phase-matching condition calls for an angle between FH and SH waves of 1.92 degrees, which, according to Eq. (4.32), matches the spectral angular dispersion required for group-velocity matching.

The diffraction grating is re-imaged at the center of the PPLN crystal so that the spectral components of the FH beam, though propagating at different angles, overlap in space inside the nonlinear crystal. The beam is focused elliptically using cylindrical lenses to achieve a spot 530- $\mu\text{m}$  wide ( $1/e^2$  intensity full-width) in the  $x$  (dispersed) dimension, and 180  $\mu\text{m}$  in the  $y$  dimension. The second harmonic is then collected and the beam waist (located in the center of the PPLN crystal) is re-imaged onto a diffraction grating with 830 lines/mm at an incident angle of 76.6 degrees where the

spectral angular dispersion of the SH field is compensated. Using the simple imaging system shown in Fig. 4.4, care must be taken to minimize spatial phase distortions due to the imaging system[72], which can result in spatial chirp. We use lenses with a 15-cm-long focal length, placed 30 cm from the diffraction grating and 30 cm from the PPLN crystal. The use of a telescope as described in Ref. [72] would eliminate the spatial phase distortions present in a single-lens system.

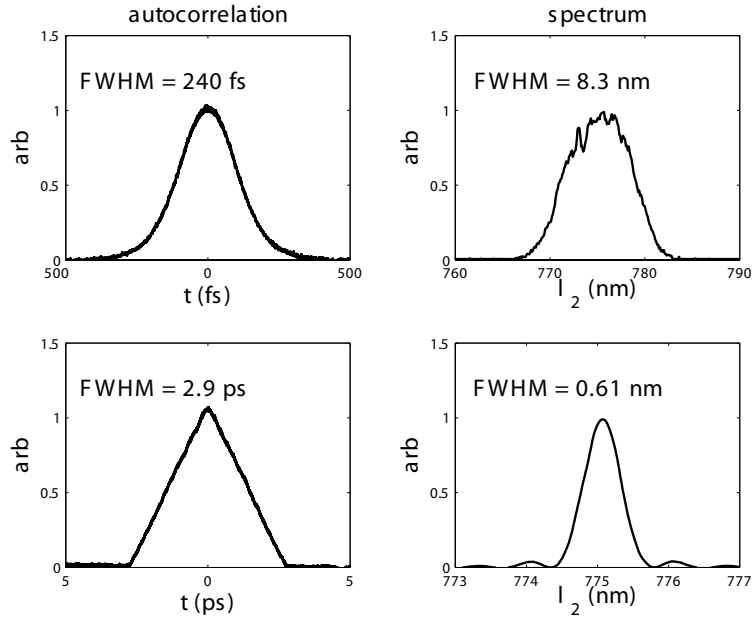


Figure 4.5: Results of SHG with spectral angular dispersion in PPLN. Autocorrelation (left) and spectrum (right) of tilted pulse-front SHG (top) and collinear SHG in identical-length crystals in the presence of group-velocity walkoff (bottom). Note the different scales in the two cases. With spectral angular dispersion, the measured autocorrelation has a full-width at half maximum (FWHM) of 240 fs and a spectral FWHM of 8.3 nm, nearly 14 times broader than the spectrum of collinear SHG in a crystal of identical length.

The resulting SH is then analyzed using an autocorrelator and an optical spectrum analyzer. The measurement results are displayed in Fig. 4.5. For comparison, we also show the measured spectrum and autocorrelation for an identical-length

crystal in a traditional collinear orientation, in which the effects of group-velocity mismatch dominate the SHG output. The bandwidth in the non-collinear case is 8.3 nm (FWHM), and is more than 14 times the group-velocity-limited bandwidth of the collinear interaction. Ignoring any bandwidth limitations from SHG, the expected SH bandwidth from FH pulses with a bandwidth of 25 nm is calculated to be 9.3 nm (assuming Gaussian FH pulses), while the experiment demonstrates 89% of this maximum bandwidth.

The output SH pulse is 170 fs (FWHM, calculated from the autocorrelation assuming a Gaussian pulse shape) in duration, approximately 1.5-times transform-limited indicating some residual spectral phase on the SH pulses. Diffraction gratings impose not only linear spectral angular dispersion, but higher-order angular dispersion as well onto the FH and SH fields. When the linear spectral angular dispersion is compensated, the higher-order dispersion is not necessarily compensated simultaneously, resulting in second-harmonic output with spatially varying frequency chirp. (A discussion of the first-order angular dispersion resulting from the reflection of a short optical pulse from a diffraction grating may be found in Ref. [73] section 1.5., and a generalization to higher-order dispersion is straightforward.) The magnitude of the higher order spectral angular dispersion can readily be calculated knowing the diffraction grating line spacing and the incident angles. For the experiment reported in Section 4.4, the quadratic phase difference across the bandwidth of the SH pulse evaluated at the beam waist is approximately equal to  $\pi$  and is of the correct magnitude to approximately account for the measured difference in pulse duration from the ideal transform-limited case. It is likely that both the higher-order phase from the diffraction gratings and spatial chirp resulting from the simple imaging system contribute to the observed longer-than-transform-limited pulse duration.

The measured conversion efficiency with a FH pulse energy of 0.58 nJ is 6.7% (SH energy of 38.7 pJ). The undepleted-pump conversion efficiency for near-field Gaussian beams with FH pulse energy  $U_1$  and a nonlinear coefficient  $d_m$  is given by[23]

$$\eta = \frac{2\sqrt{2\pi}d_m^2}{\epsilon_0cn_2n_1^2\lambda_1^2} \frac{U_1L^2}{w_xw_y\tau_0} \quad (4.10)$$

where  $n_i$  is the refractive index at the FH ( $i = 1$ ) and SH ( $i = 2$ ) wavelengths,  $\lambda_1$  is the FH vacuum wavelength and  $L$  is the interaction length. The FH field is assumed to be a Gaussian field in space and time, with  $1/e$  intensity half-width duration of  $\tau_0$  and beam width equal to  $w_x$  and  $w_y$  (also  $1/e$  intensity half-width) in the transverse  $x$  and  $y$  dimensions, respectively. Using the measured beam size of  $w_x = 187\mu\text{m}$  ( $1/e^2$  full-width =  $530\mu\text{m}$ ) and  $w_y = 64\mu\text{m}$  ( $1/e^2$  full-width =  $180\mu\text{m}$ ) and pulse duration of 138 fs ( $\tau_0 = 84$  fs) in this experiment, the estimated normalized conversion efficiency is  $\eta_0/U_1L^2 = 108\text{ \%}/(\text{nJ}\cdot\text{cm}^2)$ . With a 1-cm crystal length and 0.58 nJ of pump energy, the predicted conversion efficiency is well into the pump depletion regime ( $\gg 10\%$ ).

It is clear that the simplified near-field Gaussian beam analysis does not accurately predict the conversion efficiency of non-collinear SHG with angular dispersion; in the following sections we discuss a theory which more accurately predicts the conversion efficiency. In addition, this model includes the effects of group-velocity dispersion, diffraction, and spatial walkoff. The influence of these effects on non-collinear, group-velocity matched SHG is discussed in detail.

## 4.5 Theoretical Model

Second-harmonic generation of a strongly tilted pulse in a non-collinear geometry departs from a plane-wave description in several ways. Perhaps the most obvious is the influence of spatial walkoff, where the generated SH field envelope walks off of the generating FH beam due to the non-collinear nature of the interaction. In a more subtle way, the pulse-front tilt also has a profound influence; as a tilted pulse is affected by diffraction more than an untilted pulse of the same beam width.

As illustrated in Fig. 4.6, a field with beam width  $w_0$  and temporal pulsewidth  $\tau_0$  subject to a large pulse tilt has a crosssection  $\Delta x \ll w_0$ . Fig. 4.6 shows field envelopes for a tilted pulse with tilt angle  $\psi$  (a) and an untilted pulse (b). In both cases, the envelope propagates normal to the  $x$  axis. The diffraction length for a beam of width  $w_0$  is  $L_R = kw_0^2$  where  $k = 2\pi n/\lambda$  is the magnitude of the wavevector, given in terms of the refractive index  $n$  and the vacuum wavelength  $\lambda$ . However, diffraction of a

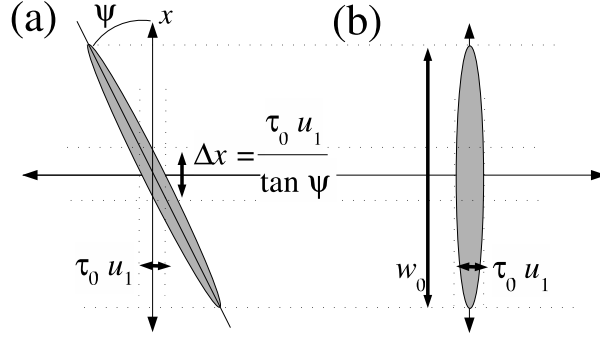


Figure 4.6: (a) Field envelope of a tilted pulse with tilt angle  $\psi$ , and (b) an untilted pulse. The width  $\Delta x$  that determines the importance of diffraction may be much less than the beam width  $w_0$  for a tilted pulse. Such a tilted field will experience diffractive effects with a characteristic length  $L'_R = k_0 \Delta x^2$  rather than the diffraction length  $L_R = k_0 w_0^2$  determined by the beam width  $w_0$ .

tilted optical pulse has a characteristic length of  $L'_R = k \Delta x^2 \ll L_R$ . Here we present a model that accounts for this difference and examine its effects on the generation of strongly tilted pulses.

To derive the equations that govern non-collinear SHG with spectral angular dispersion, we follow the conventions of Chapter 2, and consider undepleted-pump second-harmonic generation in a nonlinear, nonmagnetic dielectric with propagation direction  $z$  and variation in one transverse dimension  $x$ . The major difference between this derivation and that presented in Chapter 2 is the consideration of a non-collinear geometry.

The frequency-domain coupled scalar wave equations are

$$\frac{\partial^2 \hat{E}_1(z, x, \omega)}{\partial z^2} + \frac{\partial^2 \hat{E}_1(z, x, \omega)}{\partial x^2} + k^2(\omega) \hat{E}_1(z, x, \omega) = 0 \quad (4.11)$$

$$\frac{\partial^2 \hat{E}_2(z, x, \omega)}{\partial z^2} + \frac{\partial^2 \hat{E}_2(z, x, \omega)}{\partial x^2} + k^2(\omega) \hat{E}_2(z, x, \omega) = -\mu_0 \omega_2^2 \hat{P}_{NL}(z, x, \omega). \quad (4.12)$$

where  $k^2(\omega) = \omega^2 \epsilon(\omega) / c^2$  and  $\hat{P}_{NL}(z, x, \omega)$  is the nonlinear polarization. Subscripts 1

and 2 refer to the first harmonic (FH) and second harmonic (SH) field, respectively. It is convenient to define an electric-field envelope function  $B_i(z, x, t)$  in similar fashion to Chapter 2, but including non-collinear propagation:

$$E_i(z, x, t) = E_0 B_i(z, x, t) \exp(i\omega_i t - ik_{z,i}z - ik_{x,i}x). \quad (4.13)$$

where  $k_{z,i}$  and  $k_{x,i}$  are the  $z$  and  $x$  components, respectively, of the wavevector  $\mathbf{k}(\omega_i)$  evaluated at the carrier frequency  $\omega_i$ . We have explicitly factored out the first-harmonic field amplitude  $E_0$ , so that  $B_i(z, x, t)$  is dimensionless, and the FH envelope has unit amplitude. The magnitude of the wavevector at the carrier frequency is  $k_i$ , and is related to the components by  $k_i^2 = k_{z,i}^2 + k_{x,i}^2$ . The corresponding frequency-domain electric field  $\hat{E}_i(z, x, \omega)$  is related to the Fourier transform  $\hat{B}_i(z, x, \Omega_i)$  of this time-domain envelope as

$$\hat{E}_i(z, x, \omega) = E_0 \hat{B}_i(z, x, \Omega_i) \exp(-ik_{z,i}z - ik_{x,i}x), \quad (4.14)$$

where  $\Omega_i = \omega - \omega_i$  is the frequency detuning. To examine the effect of dispersive terms, we expand  $k^2(\omega)$  in a Taylor series around the carrier frequency for the respective fields:

$$k^2(\omega) \approx k_i^2 + 2k_i \frac{1}{u_i} \Omega_i + \frac{1}{u_i^2} \Omega_i^2 + k_i \beta_i \Omega_i^2, \quad (4.15)$$

where  $k_i$  is the magnitude of the wavevector at the carrier frequency  $\omega_i$ ;  $u_i$  is the group velocity defined in Eq. (4.8), and  $\beta_i$  is the group-velocity dispersion defined as

$$\beta_i = \left. \frac{\partial^2 k}{\partial \omega^2} \right|_{\omega_i}. \quad (4.16)$$

For uniformly periodic nonlinear media, we assume that the nonlinear coefficient distribution  $d(z, x)$  is dominated by a uniform grating vector with  $z$  and  $x$  components designated by  $K_{g,z}$  and  $K_{g,x}$ , respectively, and the nonlinear coefficient distribution is given by

$$d(z, x) \approx d_m \exp(iK_{g,z}z + iK_{g,x}x), \quad (4.17)$$

where  $d_m$  is the Fourier component of an QPM grating of order  $m$ . The nonlinear

polarization is defined as

$$P_{NL}(z, x, t) = \epsilon_0 d(z, x) E_1^2(z, x, t). \quad (4.18)$$

Substituting the above expansions and envelope definitions into the coupled equations and Fourier transforming returns the time-domain form of the coupled envelope equations including dispersive terms to second-order. In the equations to follow, for simplicity, we drop the arguments from the field envelopes  $B_i = B_i(z, x, t)$ , and orient the coordinate system along the direction of propagation of the FH wave, such that  $k_{x,1} = 0$  and  $k_{z,1} = k_1$ .

$$\frac{\partial^2 B_1}{\partial z^2} - 2ik_1 \frac{\partial B_1}{\partial z} + \frac{\partial^2 B_1}{\partial x^2} - 2i \frac{k_1}{u_1} \frac{\partial B_1}{\partial t} - \frac{1}{u_1^2} \frac{\partial^2 B_1}{\partial t^2} - k_1 \beta_1 \frac{\partial^2 B_1}{\partial t^2} = 0 \quad (4.19)$$

$$\begin{aligned} \frac{\partial^2 B_2}{\partial z^2} - 2ik_{z,2} \frac{\partial B_2}{\partial z} + \frac{\partial^2 B_2}{\partial x^2} - 2ik_{x,2} \frac{\partial B_2}{\partial x} - 2i \frac{k_{z,2}}{u_2} \frac{\partial B_2}{\partial t} \\ - \frac{1}{u_2^2} \frac{\partial^2 B_2}{\partial t^2} - k_2 \beta_2 \frac{\partial^2 B_2}{\partial t^2} = - \frac{4\omega_1^2 d_m E_0}{c^2} B_1^2 \exp(-i\Delta k_z z - i\Delta k_x x) \end{aligned} \quad (4.20)$$

The  $z$ -component of the wavevector mismatch  $\Delta \mathbf{k} = 2\mathbf{k}_1 - \mathbf{k}_2 + \mathbf{K}_g$  is defined as  $\Delta k_z = 2k_1 - k_{z,2} + K_{g,z}$  and  $x$ -component is  $\Delta k_x = -k_{x,2} + K_{g,x}$ . Hereafter, the interaction is assumed to be quasi-phase-matched at the carrier frequencies, i.e.  $\Delta k_z = 0$  and  $\Delta k_x = 0$ .

It is convenient to change coordinate systems to a reference frame that moves along with the FH field at the group velocity  $u_1$ . A new time coordinate  $T = t - z/u_1$  is defined, which is the time-delay relative to the center of a freely-propagating field envelope at the FH group velocity. The resulting coupled equations, in the limit of a slowly-varying field envelope are

$$i \frac{\partial B_1}{\partial \bar{z}} - \frac{1}{2} \frac{L}{L_{R,1}} \frac{\partial^2 B_1}{\partial \bar{x}^2} + \frac{L}{L_{D,1}} \frac{\partial^2 B_1}{\partial \bar{T}^2} = 0 \quad (4.21)$$

$$i \frac{\partial B_2}{\partial \bar{z}} - i \frac{L}{L_g} \frac{\partial B_2}{\partial \bar{T}} + i \frac{L}{L_a} \frac{\partial B_2}{\partial \bar{x}} - \frac{1}{2} \frac{L}{L_{R,2}} \frac{\partial^2 B_2}{\partial \bar{x}^2} + \frac{L}{L_{D,2}} \frac{\partial^2 B_2}{\partial \bar{T}^2} - \frac{n_1}{n_2} \frac{L}{L_G} B_1^2 = 0 \quad (4.22)$$

where the normalized coordinates  $\bar{z} = z/L$ ,  $\bar{x} = x/w_0$ , and  $\bar{T} = T/\tau_0$  are defined relative to the interaction length  $L$ , the characteristic beam size  $w_0$ , and the temporal pulsewidth  $\tau_0$ . Note that both spatial and temporal walkoff terms appear only in the equation for the SH field, indicating that the chosen reference frame is along the direction of propagation of the FH field ( $k_{x,1} = 0$ ) and moves at the FH group velocity.

Interaction Length	$L$
Aperture Length	$L_a = \frac{w_0}{\tan(\theta_0)}$
Rayleigh Length	$L_{R,j} = k_j r_0^2$
Group-Velocity Walkoff Length	$L_g = \frac{\tau_0}{\delta\nu}$
Group-Velocity Dispersion Length	$L_{D,j} = \frac{2\tau_0^2}{\beta_j}$
Nonlinear Mixing Length	$L_G = \frac{c}{d_m E_0} \sqrt{\frac{n_1 n_2}{\omega_1 \omega_2}}$
Effective Dispersion Length	$L'_{D,j} = \left( \frac{1}{L_{D,j}} - \frac{1}{2} \frac{\gamma_1^2}{L_{R,j}} \right)^{-1}$

Table 4.1: Characteristic lengths in non-collinear SHG with spectral angular dispersion. The aperture length is defined in terms of the phase-matching angle  $\theta_0 = k_{x,2}/k_{z,2}$ . The effective dispersion length combines the effects of group-velocity dispersion and the effective dispersion resulting from the diffraction of a pulse-front characterized by the tilt parameter  $\gamma_1$ .

The coupled equations are now clearly cast in terms of characteristic lengths listed in Table 4.1. Eqs. (4.21) and (4.22) are normalized coupled equations for the second-harmonic generation of short pulses in a non-collinear geometry, allowing for spatial walkoff, diffraction, temporal walkoff and group-velocity dispersion. To include the effects of spectral angular dispersion, the angular dispersion parameter for the FH wave[73] is defined as

$$\gamma_1 = \frac{k_1 w_0}{\tau_0} \left. \frac{\partial \phi(\omega)}{\partial \omega} \right|_{\omega_1} \quad (4.23)$$

which is also related to the pulse front tilt angle  $\psi$  through

$$\tan \psi = -\frac{\tau_0 u_1}{w_0} \gamma_1, \quad (4.24)$$

according to Eq. (4.9).

A field envelope  $B_i(\bar{z}, \bar{x}, \bar{T})$  that acquires spectral angular dispersion  $\gamma_1$  undergoes a transformation to a tilted pulse-front envelope where the time delay of the field at transverse position  $\bar{x}$  is advanced or retarded by an amount  $\gamma_1 \bar{x}$ , and the field transforms accordingly:  $B_i(\bar{z}, \bar{x}, \bar{T}) \rightarrow B_i(\bar{z}, \bar{x}, \bar{T} - \gamma_1 \bar{x})$  [73].

A strongly tilted ( $|\gamma_1| \gg 1$ ) field envelope diffracts quite differently than an untilted field envelope. As illustrated in Fig. 4.6, a tilted pulse may be influenced by diffraction even over distances much smaller than the Rayleigh length set by the beam width  $w_0$ . A tilted field envelope in a Cartesian coordinate system can be represented by an untilted field in a tilted coordinate system. We show that this transformation introduces an angular dispersion term into the coupled equations, which, while physically nonintuitive, allows a simple mathematical treatment. The advantage of such a transformation becomes apparent as intuition returns for effects such as diffraction and dispersion. In this transformation, diffraction is separated into beam diffraction (determined by the beam width  $w_0$ ) and diffraction due to pulse-front tilt which is treated as an effective GVD. In this formulation, only the new *effective* GVD, group-velocity walkoff, and diffraction coefficients must be considered.

A transformation of Eqs. (4.21) and (4.22) from coordinates  $(\bar{z}, \bar{x}, \bar{T})$  to the tilted coordinates  $(\bar{z}, \bar{x}, \bar{\tau} = \bar{T} - \gamma_1 \bar{x})$  involves a transformation of the differential operators

$$\frac{\partial}{\partial \bar{x}} \rightarrow \frac{\partial}{\partial \bar{x}} - \gamma_1 \frac{\partial}{\partial \bar{\tau}} \quad (4.25)$$

$$\frac{\partial}{\partial \bar{T}} \rightarrow \frac{\partial}{\partial \bar{\tau}} \quad (4.26)$$

$$\frac{\partial^2}{\partial \bar{x}^2} \rightarrow \frac{\partial^2}{\partial \bar{x}^2} + \gamma_1^2 \frac{\partial^2}{\partial \bar{\tau}^2} - 2\gamma_1 \frac{\partial^2}{\partial \bar{x} \partial \bar{\tau}} \quad (4.27)$$

$$\frac{\partial^2}{\partial \bar{T}^2} \rightarrow \frac{\partial^2}{\partial \bar{\tau}^2}, \quad (4.28)$$

and results in the coupled wave equations

$$i \frac{\partial B_1}{\partial \bar{z}} - \frac{1}{2} \frac{L}{L_{R,1}} \frac{\partial^2 B_1}{\partial \bar{x}^2} + \frac{L}{L'_{D,1}} \frac{\partial^2 B_1}{\partial \bar{\tau}^2} + \gamma_1 \frac{L}{L_{R,1}} \frac{\partial^2 B_1}{\partial \bar{x} \partial \bar{\tau}} = 0 \quad (4.29)$$

$$\begin{aligned} i \frac{\partial B_2}{\partial \bar{z}} - i \left( \frac{L}{L_g} + \gamma_1 \frac{L}{L_a} \right) \frac{\partial B_2}{\partial \bar{\tau}} + i \frac{L}{L_a} \frac{\partial B_2}{\partial \bar{x}} - \frac{1}{2} \frac{L}{L_{R,2}} \frac{\partial^2 B_2}{\partial \bar{x}^2} \\ + \frac{L}{L'_{D,2}} \frac{\partial^2 B_2}{\partial \bar{\tau}^2} + \gamma_1 \frac{L}{L_{R,2}} \frac{\partial^2 B_2}{\partial \bar{x} \partial \bar{\tau}} - \frac{n_1}{n_2} \frac{L}{L_G} B_1^2 = 0. \end{aligned} \quad (4.30)$$

The time variable  $\bar{\tau}$  may be understood as the normalized time delay relative to the time delay of the envelope center ( $\gamma_1 \bar{x}$ ) for each position  $\bar{x}$ . The coefficients for the  $\bar{x}$  derivatives do not change, but the coefficients for time derivatives do change, and there appears a mixed angular dispersion term with coefficients  $2\gamma_1 L/L_{R,i}$ . The diffraction of tilted pulses in this transformation results in an effective dispersion length, from the second term in Eq. (4.30), given by

$$\frac{1}{L'_{D,i}} = \frac{1}{L_{D,i}} - \frac{1}{2} \frac{\gamma_1^2}{L_{R,i}}. \quad (4.31)$$

Effective dispersion is a combination of GVD and effective temporal dispersion introduced by the diffraction of a tilted pulse front. The diffraction of the tilted pulse front as shown in Fig. 4.6 may be treated using the effective GVD, and is now separated from the diffraction of the beam which is characterized by the Rayleigh length  $L_{R,i}$  determined by the time-averaged beam width  $w_0$ . The field envelopes in this tilted coordinate system, represented in Eqs. (4.29) and (4.30), are untilted. Intuition again returns regarding diffraction and dispersion, and the effects in these equations can be ignored term-by-term when the interaction length  $L$  is much less than the corresponding characteristic length. The added complication introduced by the mixed angular dispersion term ( $\partial^2/\partial \bar{x} \partial \bar{\tau}$ ) poses little difficulty in the analysis.

If the pulse-front tilt is chosen so that  $\gamma_1 = -L_a/L_g$ , the group-velocity mismatch (GVM) term is eliminated from Eq. (4.30). Recalling the definition of  $\gamma_1$  from Eq. (4.23) a simple relation is found between the spectral angular dispersion and the

phase-matching angle between the FH and SH waves:

$$\left. \frac{\partial \phi(\omega)}{\partial \omega} \right|_{\omega_1} = \frac{\delta \nu}{k_1 \theta_0}, \quad (4.32)$$

identical to that given in Eq. (4.2). For the remainder of this chapter, we assume that  $\gamma_1 = -L_a/L_g$ , and thus that the effects of group-velocity mismatch may be neglected.

For a particular QPM grating and choice of FH and SH wavelengths, the phase-matching angle  $\theta_0$  is fixed, and through Eq. (4.32), so is the required spectral angular dispersion. If the collinear limit is approached ( $\theta_0 \rightarrow 0$ ), the spectral angular dispersion required for group-velocity matching becomes very large. Conversely, if the untilted limit is approached ( $\partial \phi / \partial \omega \rightarrow 0$ ), the phase-matching angle required for group-velocity matching must also be very large, and the result will be that a large beam or a short interaction length will be required to avoid the effects of spatial walkoff.

To take advantage of a long interaction length, a small phase matching angle is typically desired, and  $\gamma_1$  is large. Consequently, the dispersive terms in Eqs. (4.29) and (4.30) cannot, in general, be ignored even if the crystal is shorter than the material dispersion length, since an effective dispersion arises that may be many times the magnitude of the conventional group velocity dispersion.

## 4.6 General Solutions

In this section we solve Eqs. (4.29) and (4.30) in the limit of an undepleted pump and ignoring beam diffraction but allowing for diffraction of the tilted pulse front which manifests itself as an effective GVD according to Eq. (4.31). The coupled equations can be more easily solved in the temporal- and spatial-frequency domains, so the coupled equations are transformed using the Fourier transform pair

$$F(x, \tau) = \frac{1}{2\pi} \int_{-\infty}^{\infty} \int_{-\infty}^{\infty} \hat{F}(\xi, \Omega) \exp(i\Omega\tau - i\xi x) d\xi d\Omega \quad (4.33)$$

$$\hat{F}(\xi, \Omega) = \frac{1}{2\pi} \int_{-\infty}^{\infty} \int_{-\infty}^{\infty} F(x, \tau) \exp(-i\Omega\tau + i\xi x) dx d\tau. \quad (4.34)$$

The temporal- and spatial-frequency domain coupled equations corresponding to Eqs. (4.29) and (4.30) are:

$$i \frac{\partial \hat{B}_1}{\partial \bar{z}} - \frac{L}{L'_{D,1}} \bar{\Omega}_1^2 \hat{B}_1 + \gamma_1 \frac{L}{L_{R,1}} \bar{\Omega}_1 \bar{\xi}_1 \hat{B}_1 = 0 \quad (4.35)$$

$$i \frac{\partial \hat{B}_2}{\partial \bar{z}} + \frac{L}{L_a} \bar{\xi}_2 \hat{B}_2 - \frac{L}{L'_{D,2}} \bar{\Omega}_2^2 \hat{B}_2 + \gamma_1 \frac{L}{L_{R,2}} \bar{\Omega}_2 \bar{\xi}_2 \hat{B}_2 = \frac{n_1}{n_2} \frac{L}{L_G} \hat{F}_2(z, \bar{\xi}_2, \bar{\Omega}_2) \quad (4.36)$$

where  $\bar{\Omega}_i = \tau_0(\omega - \omega_i)$  is the normalized frequency detuning, and  $\bar{\xi}_i = w_0(k_x - k_{x,i})$  is the normalized spatial frequency detuning. The transform of the square of the FH field envelope is written as the self-convolution of the transform of the FH envelope:

$$\hat{F}_2(\bar{z}, \bar{\xi}_2, \bar{\Omega}_2) = \frac{1}{2\pi} \int_{-\infty}^{\infty} \int_{-\infty}^{\infty} \hat{B}_1(\bar{z}, \bar{\xi}', \bar{\Omega}') \hat{B}_1(\bar{z}, \bar{\xi}_2 - \bar{\xi}', \bar{\Omega}_2 - \bar{\Omega}') d\bar{\xi}' d\bar{\Omega}'. \quad (4.37)$$

The solution to Eq. (4.35) is

$$\hat{B}_1(\bar{z}, \bar{\xi}_1, \bar{\Omega}_1) = \hat{B}_0(\bar{\xi}_1, \bar{\Omega}_1) \exp \left[ -i \left( \frac{L}{L'_{D,1}} \bar{\Omega}_1^2 - \gamma_1 \frac{L}{L_{R,1}} \bar{\Omega}_1 \bar{\xi}_1 \right) \bar{z} \right] \quad (4.38)$$

where  $\hat{B}_0(\bar{\xi}_1, \bar{\Omega}_1)$  is the input FH field envelope, defined at  $\bar{z} = 0$ . The input FH envelope is defined at  $\bar{z} = 0$  in the center of the crystal, instead of at the incident face ( $\bar{z} = -1/2$ ) since the former is typically the location where the dispersed field is re-imaged from the diffraction grating and where the effective GVD due to pulse-front dispersion is arranged to vanish. Of course, the total effective GVD is only zero at this point if material GVD may be ignored, so in the case where material GVD is non-negligible one must take care to include the material GVD from the first half of the nonlinear crystal into this definition of the field envelope.

According to Eq. (4.38), the spectral amplitude of the FH field does not change, consistent with the assumption of an undepleted pump, but it acquires a spectral phase resulting from effective dispersion and spectral angular dispersion. To obtain

the solution for the second harmonic, it is convenient to define

$$\hat{G}_2(\bar{z}, \bar{\xi}_2, \bar{\Omega}_2) = \hat{B}_2(\bar{z}, \bar{\xi}_2, \bar{\Omega}_2) \exp \left[ -i \left( \frac{L}{L_a} \bar{\xi}_2 - \frac{L}{L'_{D,2}} \bar{\Omega}_2^2 + \gamma_1 \frac{L}{L_{R,2}} \bar{\Omega}_2 \bar{\xi}_2 \right) \bar{z} \right]. \quad (4.39)$$

The field  $\hat{G}_2$  has the same spectral amplitude as  $\hat{B}_2$ , but explicitly factors out the spectral phase of a freely-propagating SH field so that the effects of frequency conversion can more easily be seen.

On substitution of the definition in Eq. (4.39) into Eq. (4.36), the solution for the field  $\hat{G}_2(\bar{z}, \bar{\xi}_2, \bar{\Omega}_2)$  is

$$\begin{aligned} \hat{G}_2(\bar{z}, \bar{\xi}_2, \bar{\Omega}_2) &= \int_{-1/2}^{1/2} -i \frac{n_1}{n_2} \frac{L}{L_G} \hat{F}_2(z, \bar{\xi}_2, \bar{\Omega}_2) \\ &\times \exp \left[ -i \left( \frac{L}{L_a} \bar{\xi}_2 - \frac{L}{L'_{D,2}} \bar{\Omega}_2^2 + \gamma_1 \frac{L}{L_{R,2}} \bar{\Omega}_2 \bar{\xi}_2 \right) \bar{z} \right] d\bar{z}. \end{aligned} \quad (4.40)$$

The limits of integration indicate that the interaction occurs over  $-L/2 \leq z \leq L/2$ . Eq. (4.40), along with the definitions in Eqs. (4.37) and (4.39) and the FH solution in Eq. (4.38), represents the solution for broadband second-harmonic generation of a tilted FH field with angular dispersion characterized by  $\gamma_1$ .

## 4.7 Solution for a Gaussian FH field envelope

Eq. (4.40) is a general solution for tilted-pulse SHG, but in its current form is not particularly instructive. In this section, this expression is evaluated in the particular case of a Gaussian FH input field; the resulting SH field expression will give insight into the behavior of tilted pulse-front SHG. The initial FH field envelope is defined as

$$B_0(\bar{x}, \bar{\tau}) = \exp \left[ -\frac{\bar{x}^2}{2} - \frac{\bar{\tau}^2}{2} \right], \quad (4.41)$$

where the characteristic beam size  $w_0$  and pulse width  $\tau_0$  are defined as  $1/e$  intensity half-widths of the field envelope  $B_0(x, \tau)$ . Using the transform pair in Eqs. (4.33)

and (4.34), the frequency and spatial-frequency domain FH field envelope is

$$\hat{B}_0(\bar{\xi}_1, \bar{\Omega}_1) = \exp \left[ -\frac{\bar{\xi}_1^2}{2} - \frac{\bar{\Omega}_1^2}{2} \right]. \quad (4.42)$$

Substituting this Gaussian field into Eq. (4.38),  $\hat{F}_2(z, \bar{\xi}_2, \bar{\Omega}_2)$  is evaluated using Eq. (4.37) to find

$$\begin{aligned} \hat{F}_2(\bar{z}, \bar{\xi}_2, \bar{\Omega}_2) &= \frac{1}{2\sqrt{1 + 2i\frac{L}{L'_{D,1}}\bar{z} + \gamma_1^2\left(\frac{L}{L_{R,1}}\right)^2\bar{z}^2}} \\ &\times \exp \left[ -\frac{\bar{\Omega}_2^2}{4} \left( 1 + 2i\frac{L}{L'_{D,1}}\bar{z} \right) - \frac{\bar{\xi}_2^2}{4} + i\gamma_1\frac{L}{L_{R,1}}\frac{\bar{\Omega}_2\bar{\xi}_2\bar{z}}{2} \right]. \end{aligned} \quad (4.43)$$

Substituting Eq. (4.43) into Eq. (4.40), the expression for the output field envelope  $\hat{G}_2$ , related to  $\hat{B}_2$  through Eq. (4.39), is

$$\hat{G}_2(\bar{z} = 1/2, \bar{\xi}_2, \bar{\Omega}_2) = \frac{-i n_1 L}{2 n_2 L_G} \exp \left[ -\frac{\bar{\Omega}_2^2}{4} - \frac{\bar{\xi}_2^2}{4} \right] I_2(q) \quad (4.44)$$

where

$$I_2(q) = \int_{-1/2}^{1/2} \frac{\exp(iqz)}{\sqrt{1 + 2i\frac{L}{L'_{D,1}}z + \gamma_1^2\left(\frac{L}{L_{R,1}}\right)^2z^2}} dz \quad (4.45)$$

and

$$q = \gamma_1\delta_R\bar{\Omega}_2\bar{\xi}_2 + \delta_D\bar{\Omega}_2^2 - A\bar{\xi}_2. \quad (4.46)$$

The first term in the expression for  $q$  represents mismatch in the spectral angular dispersion between FH and SH fields, where

$$\delta_R = \frac{1}{2} \frac{L}{L_{R,1}} - \frac{L}{L_{R,2}} = \frac{L}{w_0^2 k_1 k_2} (k_2 - 2k_1). \quad (4.47)$$

Although we have assumed the FH and SH angular dispersion is equal to that required to maintain phase-matching across the bandwidth of the short pulse, according to the conditions given in Eqs. (4.2) and (4.4), dispersion in the refractive index causes these two waves to disperse differently as their frequency components separate in space. The

first term in  $q$  reflects the mismatch in angular dispersion, and is equal to zero if there is no angular dispersion ( $\gamma_1 = 0$ ) or if there is no difference in the refractive index at the FH and SH waves ( $n_1 - n_2 = 0$ ).

The second term represents mismatch in effective group-velocity dispersion:

$$\delta_D = \left( \frac{L}{L'_{D,2}} - \frac{1}{2} \frac{L}{L'_{D,1}} \right) = \frac{L}{2\tau_0^2} \left( \beta_2 - \frac{\beta_1}{2} \right) + \frac{\gamma_1^2 L}{2w_0^2 k_1 k_2} (2k_1 - k_2) \quad (4.48)$$

The first part is the mismatch in material group-velocity dispersion, and the second part represents the mismatch in effective group velocity dispersion that arises from the diffraction of a strongly tilted pulse. Depending on the geometry, the total effective group velocity dispersion may be dominated by either effect, but the effective dispersion term is of order  $\gamma_1$  larger than the angular dispersion effect in Eq. (4.47), so the angular dispersion mismatch may be ignored in the limit  $|\gamma_1| \gg 1$ . The third term in  $q$  represents the effects of spatial walkoff with the parameter  $A$  defined as the ratio

$$A = \frac{L}{L_a}. \quad (4.49)$$

The analysis of SHG in the presence of spectral angular dispersion depends centrally on the evaluation of  $I_2(q)$  which represents the influence of spatial walkoff and group-velocity dispersion, and can affect both the amplitude and shape of the SH envelope. The parameter  $q$  includes all frequency and spatial-frequency dependence, and groups together the effects of angular dispersion mismatch, effective GVD mismatch, and spatial walkoff. To determine the magnitude of these effects, we need only to examine each of the terms in the expression for  $q$ , and evaluate the dependence of  $I_2(q)$  on  $q$ .

The function  $I_2(q)$  can be evaluated in some practical limits that simplify the mathematics but still reveal clearly the essential physics. The first approximation is to assume strong spectral angular dispersion, or  $|\gamma_1| \gg 1$ . In addition, we assume that  $\gamma_1^2 \gg 2L_R/L_D$ , or equivalently, that the effective GVD is dominated by diffractive effects instead of material GVD and, according to Eq. (4.31),  $L'_{D,1} \approx -2L_{R,1}/\gamma_1^2$ .

With these simplifications,

$$I_2(q) = \int_{-1/2}^{1/2} \frac{\exp(iqz)}{\sqrt{1-2iDz}} dz \quad (4.50)$$

where the ratio  $D = -L/L'_{D,1} \approx \gamma_1^2 L/2L_{R,1}$  is defined to simplify notation. Since  $q$  is a function of  $\bar{\Omega}$  and  $\bar{\xi}$ ,  $I_2(q=0)$  represents the value at  $\bar{\Omega} = 0$  and  $\bar{\xi} = 0$ , or the mid-band amplitude reduction. At the mid-band, the integral can be readily evaluated, and the mid-band amplitude is defined as

$$I_0(D) = I_2(q=0) = 2\Im \left[ \frac{1}{D} (\sqrt{1-iD}) \right], \quad (4.51)$$

where  $\Im(x)$  denotes the imaginary part of  $x$ .

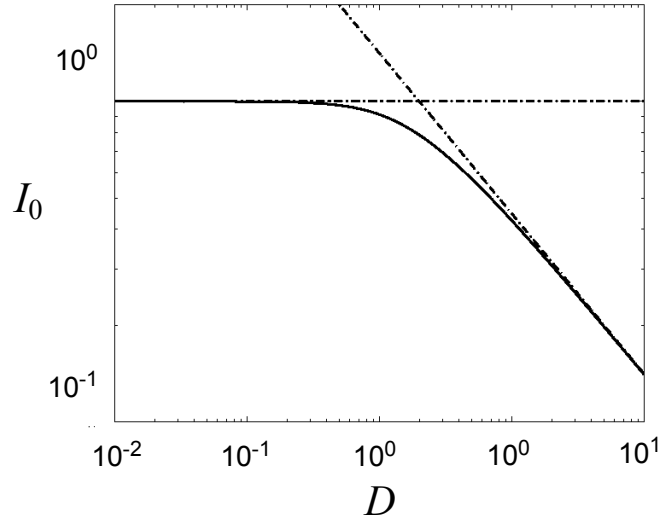


Figure 4.7: Second-harmonic amplitude reduction  $I_0(D)$ . Solid line is  $I_0(D)$ , and dotted lines indicate asymptotic behavior for  $D \ll 1$  where  $I_0(D) \approx 1$  and  $D \gg 1$  where  $I_0(D) \approx \sqrt{2/D}$ .

This function is plotted in Fig. 4.7. When  $D \ll 1$ ,  $I_0 \approx 1$  and the mid-band SH

amplitude is not influenced by the effective GVD. If  $D \gg 1$ ,  $I_0 \approx (2/D)^{1/2}$  and the mid-band SH amplitude decreases with an increasing ratio of  $|L/L'_{D,1}|$ .

In the general case the integral in Eq. (4.50) can't be expressed in terms of elementary functions, but may be expressed in terms of the complex error function defined as

$$\text{Erf}(z) = \frac{2}{\sqrt{\pi}} \int_0^z \exp(-u^2) du, \quad (4.52)$$

and  $I_2(q)$  is given by

$$I_2(q) = \text{sgn}(q) \exp\left(\frac{q}{2D}\right) \Im \left\{ \sqrt{\frac{2\pi}{qD}} \text{Erf} \left[ \sqrt{\frac{q}{2}} \left( \frac{1}{D} - i \right) \right] \right\} \quad (4.53)$$

where  $\text{sgn}(q) = q/|q|$ .

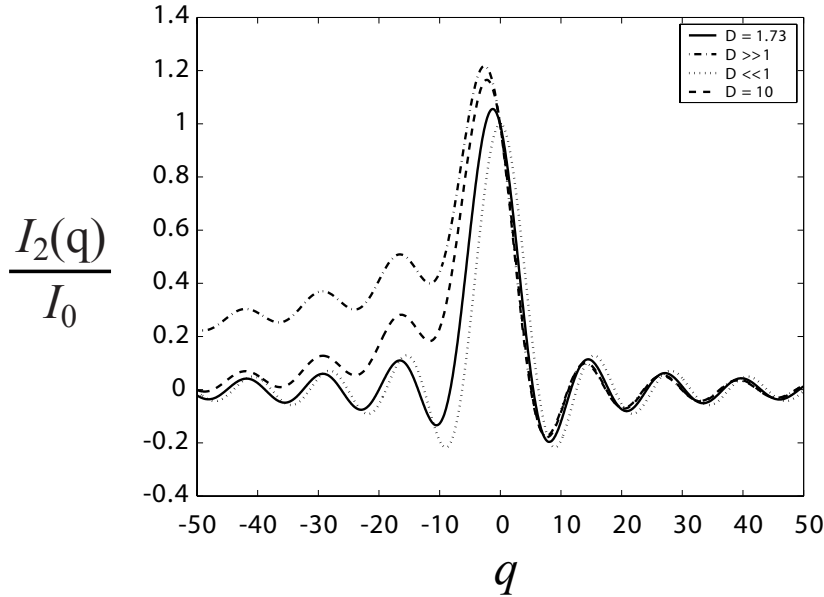


Figure 4.8: Evaluation of the response function  $I_2(q)$  for several values of  $D$ , normalized to the value at  $q = 0$ . When  $D \ll 1$ ,  $I_2(q) \approx \text{sinc}(q/2)$ . As  $D$  tends toward infinity,  $I_2(q)$  asymptotically approaches a function with a shape independent of  $D$ , and which is asymmetric with a slowly decaying tail for  $q < 0$ .

Fig. 4.8 shows a few cases of  $I_2(q)$  for several different values of  $D$ , including the limiting cases of  $D \gg 1$  and  $D \ll 1$ .

When  $D \ll 1$ ,

$$I_2(q) \approx \text{sinc}(q/2) \quad (4.54)$$

where  $\text{sinc}(x) = \sin(x)/x$ . When  $D \gg 1$ ,  $I_2(q)$  has the approximate solution

$$I_2(q) \approx \text{sgn}(q) \sqrt{\frac{2}{D}} \Im \left[ \sqrt{\frac{\pi}{q}} \text{Erf} \left( \sqrt{\frac{-iq}{2}} \right) \right] \quad (4.55)$$

In this limit, only the amplitude and not the shape of  $I_2(q)$  is influenced by the value of  $D$ .

## 4.8 Effects of GVD and spatial walkoff

Spatial walkoff and GVD are important effects influencing the behavior of second-harmonic generation. In their absence,  $I_2(q) = 1$  and the solution for tilted pulse-front SHG in Eq. (4.44) is trivial. The magnitudes of these effects are set by the magnitudes of the constants in Eqs. (4.47) through (4.49). These constants depend not only on material parameters, but on experimental conditions (i.e. interaction length, beam waist, pulse-front tilt) as well.

In order to understand the influence of spatial walkoff and GVD on conversion efficiency, bandwidth, and beam shape, we discuss in this section the influence of these effects on the solution in Eq. (4.44). All temporal frequency and spatial frequency behavior is contained in  $I_2(q)$ , since  $q$  is the only parameter in Eq. (4.44) that depends on  $\bar{\Omega}$  and  $\bar{\xi}$ .

The effect of GVD manifests itself in two ways. First, when the magnitude of dispersion at the fundamental frequency is large, the peak intensity decreases with propagation distance (see Fig. 4.9), reducing the effective interaction length. Mathematically, the magnitude of the FH dispersion appears in the ratio  $D$  and the FH intensity reduction due to GVD results in the mid-band SH amplitude reduction determined by the magnitude of  $D$ , as in Eq. (4.51). Since the magnitude of  $D$  does not

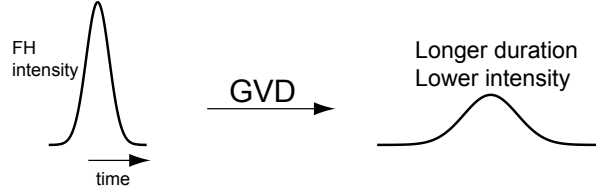


Figure 4.9: Diagram of reduced FH intensity and increased duration due to GVD. GVD causes temporal spreading, and at fixed FH energy, the peak intensity is reduced. Reduced FH intensity results in reduced SHG such that most of the frequency conversion takes place over an effective interaction length (which may be shorter than the crystal length) approximately equal to the FH dispersion length.

directly affect the shape of  $I_2(q)$ , the frequency content of the SH field is not affected by the magnitude of the effective dispersion represented by  $D$ .

While the magnitude of GVD does not directly affect the bandwidth of SHG, the mismatch between the effective dispersion of FH and SH fields (represented by the coefficient  $\delta_D$ , and shown schematically in Fig. 4.10) may influence the SH frequency content. When the effective GVD of the FH polarization and the SH field are mismatched, the result is a phase mismatch which can accumulate across the bandwidth of a short optical pulse, limiting the bandwidth of the SHG interaction. If the largest term in  $q$  is the GVD term in Eq. (4.46), then  $q \approx \delta_D \bar{\Omega}^2$  where  $\delta_D$  is the effective GVD mismatch, defined in Eq. (4.48). The frequency-domain field envelope  $\hat{G}_2$  is the product of  $I_2$  and the transform of the square of the envelope of the FH field, as in Eq. (4.39).

Fig. 4.11 shows the bandwidth reduction versus  $\delta_D$  for several values of  $D$ . With negligible dispersion mismatch ( $|\delta_D| \ll 1$ ), the expected bandwidth is  $\sqrt{2}$  times larger than the input FH bandwidth. The bandwidth decreases approximately as  $|\delta_D|^{-1/2}$  for  $|\delta_D| \gg 1$ . In order to preserve the bandwidth of the SHG interaction, one should choose the interaction length, pulse-front tilt, and beam size such that  $|\delta_D| \ll 1$ .

Note that when  $D \gg 1$  the bandwidth is asymmetric in  $\delta_D$ , and even exhibits

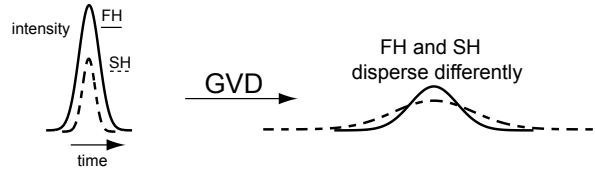


Figure 4.10: Diagram of mismatched GVD between FH and SH waves in SHG. Since FH and SH waves disperse at different rates, GVD can affect the frequency content of SHG in addition to the amplitude effects resulting from FH dispersion as shown in Fig. 4.9.

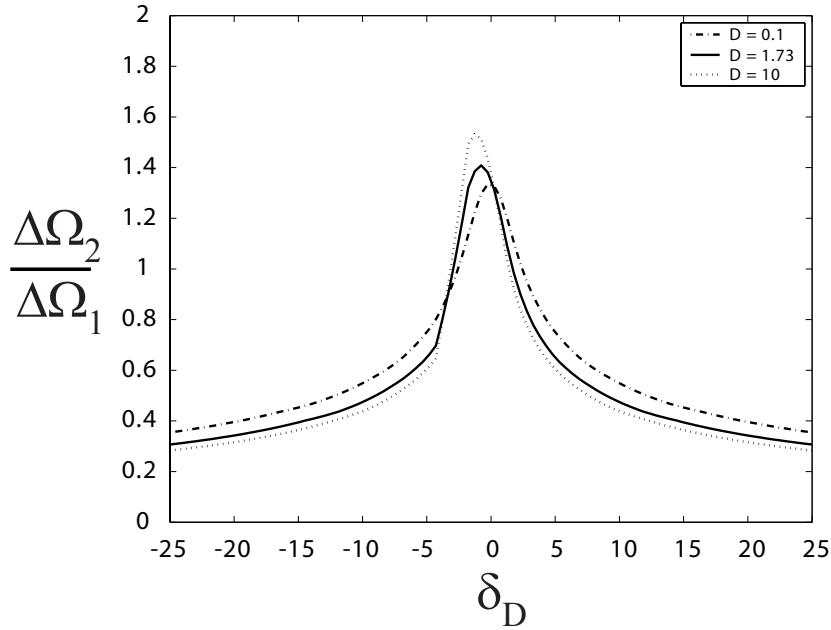


Figure 4.11: SHG acceptance bandwidth versus effective GVD mismatch parameter  $\delta_D$  defined in Eq. (4.48) for several values of the FH effective dispersion parameter  $D$ . Here spatial walkoff is neglected, so that  $q \approx \delta_D \Omega_2^2$ . Minimal loss of bandwidth results when  $|\delta_D| < 1$  regardless of the magnitude of  $D$ .

larger bandwidth than the  $\delta_D = 0$  case. This is due to the asymmetry in  $I_2(q)$  for  $D \gg 1$  shown in Fig. 4.8. Since  $q$  is quadratic in  $\bar{\Omega}$ , and the envelope of  $I_2(q)$  is not symmetric in  $q$ , the behavior can be quite different for different signs of  $\delta_D$ .

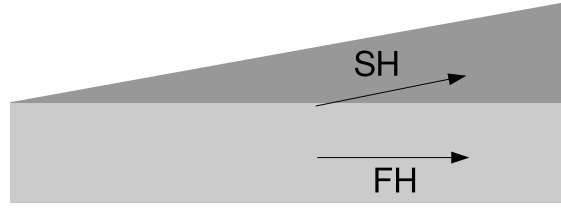


Figure 4.12: Diagram of spatial walkoff in noncollinear interactions. The SH beam (dark gray) walks off the FH beam (light gray) in a noncollinear interaction. The results are reduced conversion efficiency since SH is generated over an effective interaction length approximately equal to the aperture length  $L_a$ , as well as beam distortions resulting from a walkoff-dominated interaction.

Spatial walkoff (characterized by the aperture length  $L_a$  appearing in the parameter  $A$  in Eq. 4.46) also affects noncollinear SHG, as shown in Fig. 4.12. When  $q$  (see Eq. (4.46)) is dominated by the spatial walkoff term,  $q \approx -A\bar{\xi}_2$  where  $A = L/L_a$ . In this limit,  $I_2$  is independent of  $\bar{\Omega}$ , and even in the limit of large spatial walkoff, the frequency content of the electric field is unaltered. Walkoff will, however, limit the spatial frequency content for large values of  $|A|$ , and accordingly affects the size and shape of the SH beam. Although negligible dispersion mismatch ( $|\delta_D| < 1$ ) is a necessary condition for preserving the bandwidth of SHG, spatial walkoff does not affect the frequency bandwidth.

Fig. 4.13 shows the effects of varying spatial walkoff on the output beam size and shape for different values of the effective dispersion characterized by  $D$ . In all cases, as  $A = L/L_a$  increases, the beam size increases when  $I_2(q = -A\bar{\xi}_2)$  becomes narrower than the field envelope, or when  $|A| \approx 1$  and the field envelope is influenced

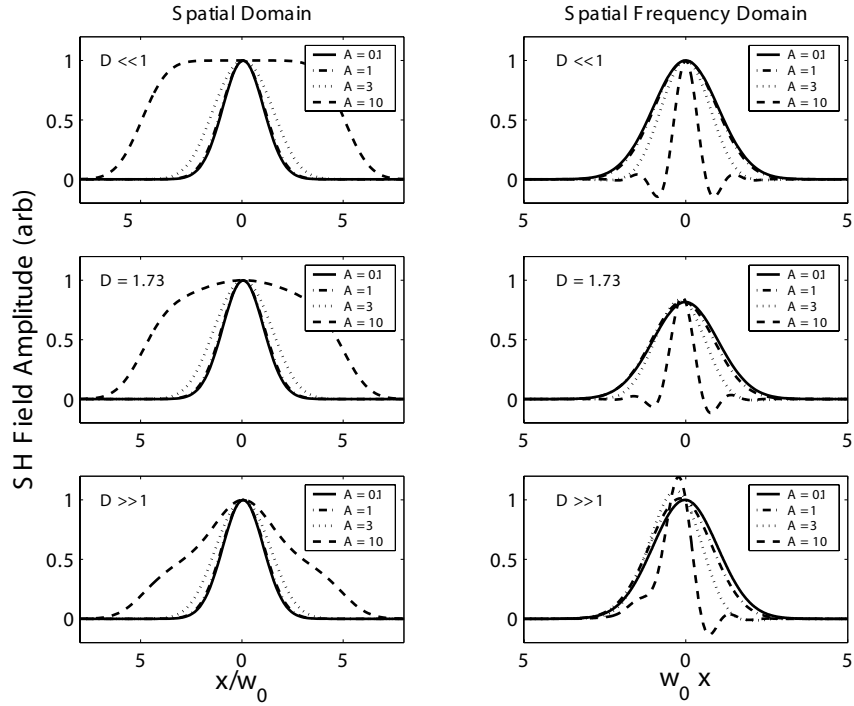


Figure 4.13: Effects of spatial walkoff on beam profile for several values of the spatial walkoff parameter  $A = L/L_a$ . On the left is plotted the near-field SH amplitude versus  $x$ , and on the right the field amplitude versus spatial frequency (proportional to the far-field SH amplitude distribution after angular dispersion has been compensated) is shown. The shape of the response function  $I_2(q)$  is influenced by the dispersion parameter  $D$ , while increasing  $A$  changes the scaling of the width of the response function in the spatial frequency domain since  $q = A\xi$ . When  $A \ll 1$  the response function is much wider than the polarization distribution and both the near-field and far-field distributions are Gaussian for all values of  $D$ . When  $A > 1$  the response function is narrower than the polarization distribution, and the SH amplitude is influenced by the shape of  $I_2(q)$ . When  $D \ll 1$  (top graphs),  $I_2(q) \approx \text{sinc}(q)$  and the near-field distribution approaches a flat-top function. For larger  $D$  (middle and bottom graphs),  $I_2(q)$  departs from the  $\text{sinc}(q)$  behavior as shown in Fig. 4.8, and the near-field and far-field distributions reflect the distortion of the response function when  $A > 1$ .

by the shape of  $I_2(q = -A\bar{\xi}_2)$ . Although when  $D \ll 1$  the resulting beam profile for  $|A| \gg 1$  would be a flat-top function (i.e. with a Fourier transform proportional to  $I_2(q) = \text{sinc}(q/2)$ ), at larger values of  $D$  this is not true. Section 4.10 discusses how the beam size and quality trade off against conversion efficiency, as the scaling of conversion efficiency with  $A$  is discussed in more detail.

This section has considered separately the influence of spatial walkoff and GVD mismatch. When one effect is clearly dominant, it influences separately the frequency and spatial-frequency content of the SH envelope; i.e. spatial walkoff does not influence the frequency content of the SH envelope, and GVD mismatch does not affect the SH spatial envelope. In general, however,  $q$  contains terms influenced by both spatial walkoff and GVD mismatch as shown in Eq. (4.46). If both  $L/L_a$  and  $\delta_D$  are of comparable magnitude, they must be considered together in the evaluation of  $I_2(q)$ . Consequently, the frequency and spatial-frequency behavior may not be separately attributed to the magnitude of GVD mismatch and spatial walkoff, respectively.

For the remainder of this chapter, we assume that  $|\delta_D| \ll 1$  in order to preserve the bandwidth of SHG and the effects of GVD mismatch are neglected.

## 4.9 Conversion efficiency in the absence of spatial walkoff and GVD

With the field solution of Eq. (4.44), the energy conversion efficiency for tilted pulse-front SHG is defined as the ratio of SH energy to FH energy:

$$\eta = \frac{U_2}{U_1} = \frac{n_2 \int_{-\infty}^{\infty} \int_{-\infty}^{\infty} |\hat{B}_2(\bar{z} = 1/2, \bar{\xi}, \bar{\Omega})|^2 d\bar{\xi} d\bar{\Omega}}{n_1 \int_{-\infty}^{\infty} \int_{-\infty}^{\infty} |\hat{B}_0(\bar{\xi}, \bar{\Omega})|^2 d\bar{\xi} d\bar{\Omega}}. \quad (4.56)$$

The conversion efficiency is evaluated using the definition of  $\hat{G}_2$  in Eq. (4.44), its relation to  $\hat{B}_2$  in Eq. (4.39), and the FH field used in this Gaussian example from Eq. (4.42). In the limit of negligible effective GVD and angular dispersion,  $I_2 \approx 1$ .

If  $L/L_G$  is written in terms of the FH pulse energy,

$$\left(\frac{n_1 L}{n_2 L_G}\right)^2 = \frac{8\pi d_m^2}{\epsilon_0 c n_2^2 n_1 \lambda_1^2} \frac{U_1 L^2}{w_0 \sigma_y \tau_0}, \quad (4.57)$$

where  $\sigma_y$  is the effective crosssection of the FH beam in the transverse  $y$  dimension (equal to  $\sqrt{\pi}w_y$  for a Gaussian field). The conversion efficiency is

$$\eta_0 = \frac{n_2}{2n_1} \left(\frac{n_1 L}{n_2 L_G}\right)^2 = \frac{4\pi d_m^2}{\epsilon_0 c n_2 n_1^2 \lambda_1^2} \frac{U_1 L^2}{w_0 \sigma_y \tau_0}. \quad (4.58)$$

The conversion efficiency is equal to the well known result for an untilted Gaussian FH pulse in the absence of group-velocity mismatch, GVD, diffraction and spatial walkoff[23]. The peak-power conversion efficiency is  $2\eta_0$ , and an additional factor of  $1/2$  results from averaging this peak-power efficiency over Gaussian envelopes in the transverse  $x$  dimension and in time. The theoretical model of Sections 5 through 7 ignores variations in the field envelope in the transverse- $y$  dimension, and consequently assumes an equal effective area of the FH and SH envelopes in this dimension. However, considering a Gaussian envelope in  $y$  simply involves substituting the FH effective area  $\sigma_y = \sqrt{\pi}w_y$  and further reducing the expression in Eq. (4.58) by a factor of  $1/\sqrt{2}$  due to the averaging of conversion efficiency over a Gaussian envelope in the  $y$ -dimension. With such a substitution, Eq. (4.58) is equivalent to the plane-wave estimate in Eq. (4.10).

For QPM-SHG in uniform (including uniformly periodic) nonlinear materials in the presence of group-velocity mismatch, the interaction length is chosen as  $L = 2L_g$  to preserve the pulse width[23]. The conversion efficiency for an untilted Gaussian FH beam limited by group-velocity mismatch is

$$\eta_{gvm} = \frac{38.3 d_m^2}{\epsilon_0 c n_2 n_1^2 \lambda_1^2} \frac{U_1 L_g^2}{w_0 \sigma_y \tau_0} = 3.05 \frac{L_g^2}{L^2} \eta_0 \quad (4.59)$$

and comparing Eq. (4.58) with Eq. (4.59) we find that group-velocity compensation through spectral angular dispersion gives an advantage of  $0.33L^2/L_g^2$  in conversion efficiency over using a collinear geometry and a bandwidth-limited crystal length

equal to  $2L_g$ . Using a chirped grating with an optimum grating chirp ( $D_g = 3\delta\nu/\tau_0L$ ) and an unchirped FH pulse results in a conversion efficiency of[23]

$$\eta_{CG} = 1.37 \frac{L}{L_g} \eta_{gvm} = 4.18 \frac{L_g}{L} \eta_0 \quad (4.60)$$

and comparing with Eq. (4.58) we find that the efficiency for the spectral angular dispersion technique is greater by a factor of  $0.24L/L_g$  than when using a chirped QPM grating.

## 4.10 Conversion efficiency in the presence of spatial walkoff and GVD: optimizing the focusing conditions and phase-matching angle

While it is always possible through appropriate choice of the phase-matching angle and the beam size to design an experiment with negligible effective GVD and spatial walkoff, it is not true that those conditions result in the peak conversion efficiency. Here the GVD mismatch parameter is assumed small ( $\delta_D \ll 1$ ), so that  $q = -A\bar{\xi}_2$  with  $A = L/L_a$ .

In an SHG experiment (in the absence of optical damage) there exists an optimum focusing condition for peak conversion efficiency. Boyd and Kleinman showed that, for continuous-wave interactions in the absence of spatial walkoff, there exists an optimum focusing condition approximated closely by confocal focusing, i.e. for a diffraction length equal to half the crystal length[74]. The nature of this optimum condition involves a trade-off between high peak intensity and an effective interaction length that may be less than  $L$  for tightly focused beams. For beams with waists larger than the confocal waist, decreasing the waist results in an increased intensity which is approximately constant over the interaction length, and the result is higher conversion efficiency. For beams smaller than the confocal waist, however, the effective interaction length is reduced below the crystal length  $L$  and the conversion efficiency decreases with tighter focusing. An analogous qualitative argument may

be made regarding the effective dispersion that exists in tilted pulse-front SHG, and the remainder of this section will show that the maximum conversion efficiency is achieved when the interaction length is equal to 1.73 times the effective dispersion length. This result is analogous to the focusing condition for best SHG conversion set forth in reference [74], where the interaction length is 2.84 times the FH confocal length. (This condition is often approximated by an interaction length equal to the confocal length, where the efficiency is 80% of the maximum but with a reduced peak intensity.)

In addition to a choice of focusing conditions, quasi-phase-matching affords a choice of phase-matching angles, since QPM gratings can be constructed to phase-match a variety of non-collinear interactions. Decreasing the phase-matching angle reduces spatial walkoff but also decreases the effective dispersion length (at fixed spot size). Maximizing the conversion efficiency involves choosing properly both the focusing conditions and the phase-matching angle.

With a given nonlinear material at a fixed FH wavelength and pulse duration, the effective dispersion length  $L'_{D,1}$  and the aperture length  $L_a$  are uniquely determined by the FH spot size  $w_0$  and the phase-matching angle  $\theta_0$ . The discussion to follow shows what choice of  $L_a$  and  $L'_{D,1}$ , or equivalently  $w_0$  and  $\theta_0$ , leads to the maximum conversion efficiency of a particular interaction at a fixed interaction length.

Including the effects of spatial walkoff and effective dispersion,

$$\eta = \eta_0 h(D, A) \quad (4.61)$$

where  $\eta_0$  is the conversion efficiency with negligible GVD and spatial walkoff, given in Eq. (4.58), and the efficiency reduction factor  $h$  is defined as

$$h(D, A) = \frac{1}{2\pi} \int_{-\infty}^{\infty} |I_2(q)|^2 \exp\left(-\frac{\bar{\Omega}_2^2}{2} - \frac{\bar{\xi}_2^2}{2}\right) d\bar{\Omega}_2 d\bar{\xi}_2. \quad (4.62)$$

Recalling the definition of parameters  $A = L/L_a$  and  $D = -L/L'_{D,1}$  representing the influence of spatial walkoff and effective dispersion, respectively; the efficiency reduction factor is plotted in Fig. 4.14 for several values of  $D$ . When  $|A| \ll 1$ ,  $h$  is

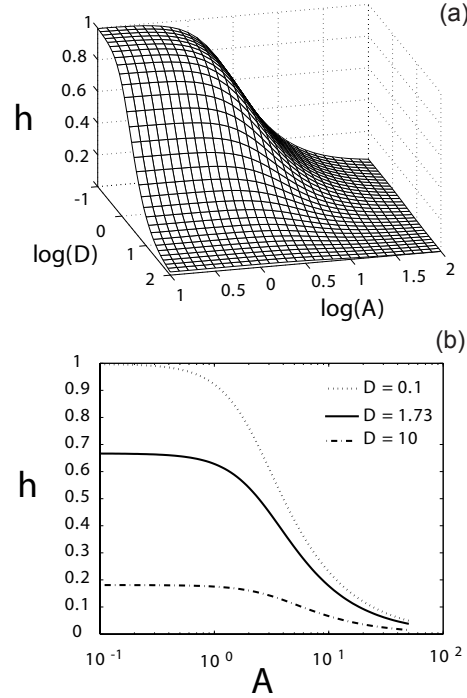


Figure 4.14: (a) Surface plot of the efficiency reduction factor  $h(A, D)$  as a function of  $A = L/L_a$  and  $D = L/L'_{D,1}$ . When both spatial walkoff and effective dispersion may be ignored ( $A \ll 1$  and  $D \ll 1$ ),  $h(A, D) \approx 1$ . Increased effective dispersion ( $D > 1$ ) leads to pulse spreading, and the length over which the intensity is at its maximum is reduced, resulting in a decreased conversion efficiency. Increased spatial walkoff ( $A > 1$ ) results in a generated SH field that propagates away from the peak FH intensity also resulting in a reduced effective interaction length and decreasing conversion efficiency. (b) Plot of  $h(A, D)$  at fixed selected values of  $D$ . For  $A \ll 1$ ,  $h(A, D) \approx |I_0|^2$  as given in Eq. (4.51) determined only by the effective dispersion parameter  $D$ .

simply the square of the amplitude reduction given in Eq. (4.51).

The efficiency reduction factor  $h$  is a function of  $D$  and  $A$ , and is consequently also a function of both  $w_0$  and  $\theta_0$ . The nonlinear mixing length  $L_G$  also changes with the input beam size, so maximizing the efficiency involves a balance between maximizing the reduction factor  $h$  and minimizing  $L_G$ .

Recalling the definitions of the characteristic lengths  $L_a$  and  $L'_{D,1}$ , we rewrite the relation in Eq. (4.57) as

$$\left(\frac{n_1}{n_2} \frac{L}{L_G}\right)^2 = \frac{16\pi^{3/2} d_m^2 L_g}{\epsilon_0 c n_2^2 n_1^{1/2} \lambda_1^{5/2}} \frac{U_1 L^{1/2}}{\sigma_y \tau_0} \frac{L}{L_a} \sqrt{\frac{L}{L'_{D,1}}}. \quad (4.63)$$

Upon substitution into Eq. (4.61), the conversion efficiency is equal to

$$\eta = \frac{8\pi^{3/2} d_m^2 L_g}{\epsilon_0 c n_2 n_1^{3/2} \lambda_1^{5/2}} \frac{U_1 L^{1/2}}{\sigma_y \tau_0} A \sqrt{D} h(A, D) \quad (4.64)$$

At fixed interaction length, variations in beam size  $w_0$  and phase matching angle  $\theta_0$  change only  $A$  and  $D$ , so that finding the maximum in  $A\sqrt{D}h(A, D)$  will return the focusing and phase-matching conditions for peak conversion efficiency. A global optimization of the conversion efficiency predicts that the conversion efficiency saturates to its maximum value when  $A$  tends to infinity; i.e. the limit of large spatial walkoff corresponding to very tight focusing and/or a large phase-matching angle. Practically speaking, however, this results in an output SH envelope with a spatial frequency distribution that is narrow (i.e. a wider SH beam) and resembles the function  $I_2(q)$  shown in Fig. 4.8. The resulting beam profile may be a top-hat when  $D \ll 1$  and  $I_2(q) \approx \text{sinc}(q/2)$ , or may have a spatial frequency distribution with a slowly-decaying asymmetric tail when  $D \gg 1$ .

Let us examine more closely the trade-off between beam quality and conversion efficiency. When  $A \ll 1$ ,  $h = h_0 = |I_0(D)|^2$  and is independent of  $A$ . Fig. 4.15 plots  $\sqrt{D}|I_0(D)|^2$ , and it demonstrates a peak at  $D_{max} = 1.73$ . This value of  $D$  maximizes the mid-spatial-frequency conversion efficiency. At larger values of  $D$ , the effective dispersion length is shorter than the interaction length, resulting in a decreased peak intensity over a significant portion of the interaction length. This decreased peak

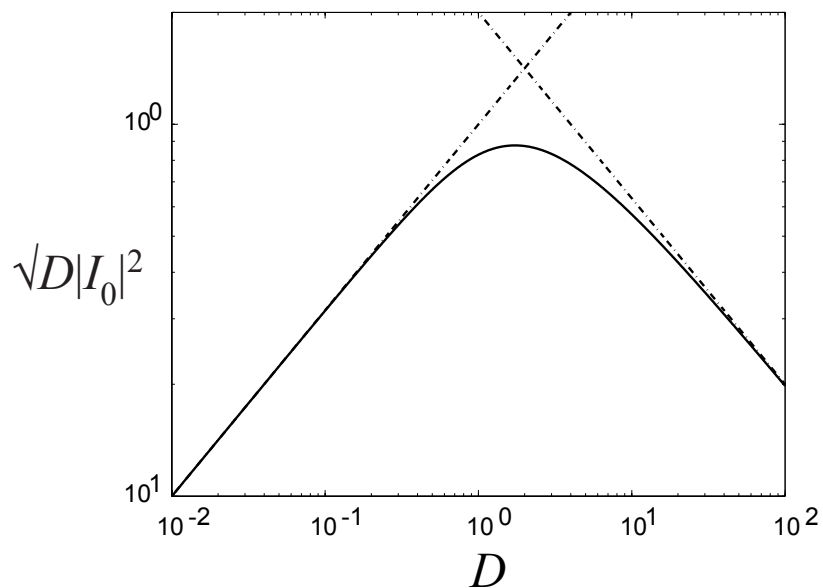


Figure 4.15: The normalized SH amplitude is proportional to the function  $\sqrt{D}|I_0(D)|^2$ , and demonstrates a peak at  $D = 1.73$ . Dotted lines indicate asymptotic behavior for  $D \ll 1$  where  $I_0(D) \approx 1$  and  $D \gg 1$  where  $I_0(D) \approx \sqrt{2/D}$ .

intensity is the source of the decreasing conversion efficiency when  $D \gg 1$ . For large pulse-front tilt  $|\gamma_1| \gg 1$ , note that  $D = 1.73$  implies  $L/L_{R,1} \ll 1$ , and the entire interaction takes place in the near field of the FH beam.

In the limits when  $D \ll 1$  and  $D \gg 1$ , Eqs. (4.54) and (4.55) demonstrate that the value of  $D$  affects the amplitude of  $I_2(q)$ , but not the functional form. Indeed, even when  $D \approx 1$ , the shape of  $I_2(q)$  changes very slowly with different values of  $D$  (see Fig. 4.8), and one might expect that the optimum value of  $D$  will be near its value when evaluated assuming no walkoff ( $A \ll 1$ ) as in cases with small amounts of walkoff  $A \approx 1$ . This assertion can be verified numerically; the optimum value for  $D$  is nearly independent of the choice of  $A$ . (For an absolute optimization of conversion efficiency, both  $D$  and  $A$  tend to infinity; however, large  $A$  results in significant beam distortions as shown below. If reasonably good beam quality is desired, the optimum value for  $D$  can be treated independently of the choice of  $A$ .)

With an optimum value for  $D$ , the SH conversion changes by changing  $A$  with fixed  $D$ . With  $D$  fixed, the phase matching angle is fixed and changing  $A = L/L_a = L\theta_0/w_0$  may be accomplished by changing the beam waist  $w_0$ . As  $A$  increases, the amplitude of the SH field increases as a result of the increased intensity resulting from a smaller beam waist, but the spatial frequency bandwidth narrows as  $I_2(q)$  becomes narrower than the Gaussian polarization envelope in Eq. (4.44). As a result, the SH beam broadens, and its shape is influenced by the shape of  $I_2(q)$  as shown in Fig. 4.13. If  $|A| \ll 1$ ,  $I_2(q = -A\bar{\xi}_2)$  is approximately constant over the spatial frequency envelope of  $\hat{G}_2$ , and the SH beam is Gaussian, with beam quality parameter[75]  $M^2 = 1$  and a beam size that is  $\sqrt{2}$  times smaller than the FH pump beam.

Fig. 4.16 quantifies the tradeoffs between conversion efficiency and beam size and quality. Conversion efficiency, beam size, and beam quality are plotted as  $D$  is held fixed at its optimum value of  $D_{max} = 1.73$ . When  $A = 3$ , the conversion efficiency is at 71% of its maximum value. The SH beam with  $A = 3$  has a waist that is approximately  $\sqrt{2}$ -times larger than the  $A \ll 1$  value, or roughly equal to the FH beam size  $w_0$ , and has  $M^2 = 1.10$ . (The beam quality parameter  $M^2 = 1$  for a perfect Gaussian  $TEM_{00}$  mode, and increases with increasing higher order mode content. For a more complete discussion on the concept and measurement of  $M^2$ , see

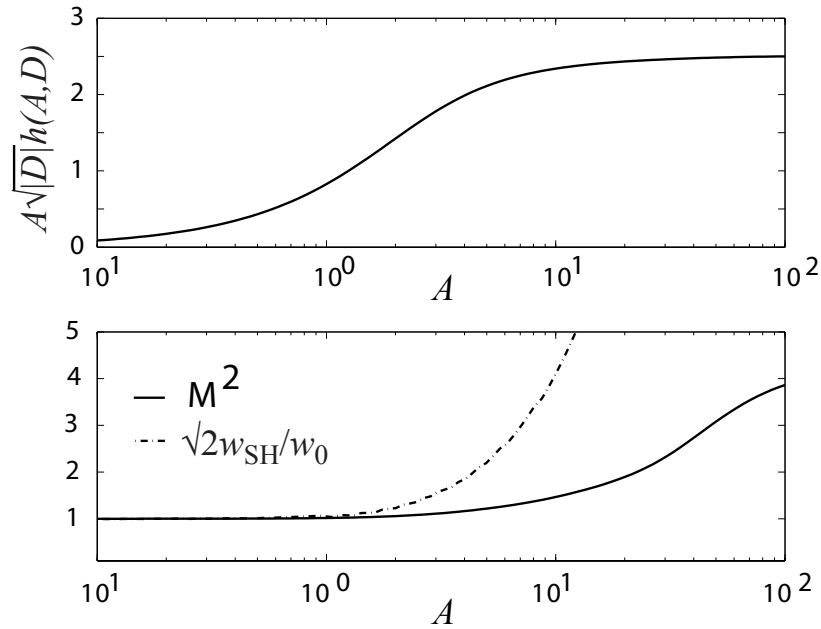


Figure 4.16: Trade-off of normalized conversion efficiency (top) and beam size and quality (bottom) with optimum dispersion parameter  $D = 1.73$  in the presence of spatial walkoff. At fixed value of  $D$ , the spatial walkoff parameter  $A = L/L_a$  is increased by decreasing the beam size  $w_0$ . The increased intensity results in higher conversion efficiency, but the resulting increase in spatial walkoff causes an increase in SH beam size and poor SH spatial mode quality. A compromise may be reached for  $A \approx 3$ , where the conversion efficiency reaches 71% of its maximum value, but the beam is approximately equal to the FH beam size with a beam quality parameter  $M^2 = 1.10$  ( $M^2 = 1$  implies a Gaussian  $\text{TEM}_{00}$  mode).

Ref. [75].) With  $A = 3$  and  $D = 1.73$ ,  $h(A, D) = 0.45$  and the conversion efficiency in Eq. (4.64) is

$$\eta = \frac{79d_m^2}{\epsilon_0 c n_2 n_1^{3/2} \lambda_1^{5/2} \delta\nu} \frac{U_1 L^{1/2}}{\sigma_y}. \quad (4.65)$$

If the beam is confocally focused in the transverse  $y$  (non-dispersed) dimension for maximum conversion efficiency[74], then  $\sigma_y = (L\lambda_1/3.2n_1)^{1/2}$ , and the optimized conversion efficiency is

$$\eta_{opt} = \frac{141.4d_m^2}{\epsilon_0 c \delta\nu n_2 n_1 \lambda_1^3} U_1. \quad (4.66)$$

This result is compared with the conversion efficiency for collinear SHG in a uniform crystal with a bandwidth-limited length of  $L = 2L_g$  and confocal focusing[23]

$$\eta_{gvm}^{conf} = \frac{76.7d_m^2}{\epsilon_0 c \delta\nu n_1 n_2 \lambda_1^3} U_1 \quad (4.67)$$

and with the conversion efficiency for collinear SHG in a chirped QPM grating with confocal focusing[23]

$$\eta_{CG}^{conf} = 1.39\eta_{gvm}^{conf} = \frac{106.6d_m^2}{\epsilon_0 c \delta\nu n_1 n_2 \lambda_1^3} U_1 \quad (4.68)$$

and the scaling of the conversion efficiency for all three cases is identical. The difference in the magnitude of the conversion efficiency lies primarily in selecting the “best conditions”, since all three techniques require some subjective choice regarding a trade-off. Non-collinear SHG with spectral angular dispersion trades off beam quality with conversion efficiency, while the other two trade off bandwidth and conversion efficiency. In all three cases, a slightly higher conversion efficiency may be obtained at an expense of either decreased SH bandwidth or reduced SH beam quality.

Table 4.2 summarizes the comparison between ultrafast SHG in a short, uniform grating, in a chirped-grating, and with spectral angular dispersion.

Since all three techniques under optimum focusing conditions yield approximately identical values for energy conversion efficiency, other considerations may influence the experimenter’s choice regarding the best method in a particular application. For

Technique	NF Efficiency	Opt. Efficiency	Optimized Area
Short Crystal	$\eta_{gvm} = \frac{21.3d_{eff}^2}{n_1 n_2 \lambda_1^2} E_0^2 L_g^2$	$\eta_{gvm}^{conf} = \frac{76.7d_{eff}^2}{\epsilon_0 c n_2 n_1 \lambda_1^3 \delta \nu} U_1$	$A_0 = \frac{5}{8} \frac{\lambda_1 L_g}{n_1}$
Chirped-Grating	$\eta_{CG} = 1.37 \frac{L}{L_g} \eta_{gvm}$	$\eta_{CG}^{conf} = 1.39 \eta_{gvm}^{conf}$	$\left(\frac{L}{4L_g}\right) A_0$
Angular Dispersion	$\eta_0 = 0.33 \frac{L^2}{L_g^2} \eta_{gvm}$	$\eta_{opt} = 1.84 \eta_{gvm}^{conf}$	$\left(\frac{L^2}{8L_g^2}\right) A_0$

Table 4.2: Comparison of techniques for ultrashort-pulse SHG: efficiency and effective area. Here we compare the conversion efficiency for SHG under conditions of near-field (NF) and optimized focusing conditions, as well as list the beam area under optimized focusing conditions for three techniques for ultrashort-pulse SHG discussed in this chapter.

example, using a short QPM grating is significantly simpler than using chirped gratings or spectral angular dispersion, as no dispersive elements are required. Dispersive elements are required when using either a chirped QPM grating (a grating pair or dispersive material is required to compress the chirped SH output, although with a chirped FH pulse the phase response of the QPM grating can result in pulse compression without gratings as discussed in Chapter 3) or spectral angular dispersion (a grating or prism is required at the input to impose angular dispersion on the FH and at the output to compensate the angular dispersion of the generated SH field). Additional dispersive elements add both complexity and loss. However, since a short QPM grating is much shorter than the crystal length that may be used for the other two techniques, the required focusing for best conversion requires a much smaller spot size and results in a correspondingly high peak intensity. If this intensity exceeds the damage intensity, or leads to increased two-photon absorption, either of the other two techniques allows for the same conversion efficiency at much larger spot sizes. In the tilted pulse-front case, the optimum is reached when the beam size is larger than confocal, and so offers a lower peak intensity for the same conversion as a chirped grating of equivalent crystal length. The peak FH intensity in non-collinear SHG with spectral angular dispersion under the optimum focusing conditions discussed above

is a factor of  $8(L_g/L)^2$  lower than the peak intensity for a short crystal of length  $2L_g$  under confocal-focusing conditions, and is a factor of  $4L_g/L$  lower than for confocal focusing into a chirped QPM crystal of equivalent length  $L$ .

Returning to the experiment in Section 4.4, the effective dispersion and spatial walkoff can be included through the efficiency reduction factor  $h(A, D)$  in Eq. (4.61). With a beam size  $w_0 = 180\mu\text{m}$  and a phase matching angle of  $\theta_0 = 1.92$  degrees, the aperture length is 5.6 mm, making  $A = L/L_a = 1.8$  for a crystal length of 1 cm. The group-velocity walkoff length  $L_g$  is equal to  $260\mu\text{m}$  for 138 fs pulses ( $\tau_0 = 84\text{fs}$ ), so that the pulse front tilt parameter  $|\gamma_1| = L_a/L_g = 21$ , and the effective dispersion length is  $|L'_{D,1}| = 1.4\text{mm}$  with  $D = 7.1$ . The GVD mismatch parameter  $\delta_D = 0.31$ , so negligible loss of bandwidth is expected. The corresponding efficiency reduction factor  $h(A, D)$  is 21%, making the calculated conversion efficiency 14.7% in reasonable agreement with the 6.7% observed. Note that these values of  $A$  and  $D$  are not the optimum values computed in the theoretical calculation, and accordingly with a 1-cm-length crystal one could achieve a higher conversion efficiency by decreasing both the phase-matching angle and the beam size until  $A \approx 3$  and  $D = 1.73$ , i.e. for  $\theta_0 = 1.56$  degrees and  $w_0 = 91\mu\text{m}$ . With confocal focusing in the non-dispersed dimension, the peak conversion efficiency calculated with Eq. (4.66) is 143 %/nJ, or well into pump depletion with a FH pulse energy of 0.58 nJ.

## 4.11 Generalized Three-Wave Description

Fig. 4.17 shows a diagram (similar to Fig. 1 in Ref. [42]) of group-velocity mismatch compensation for a general three-wave mixing process in a QPM device. The pulse fronts of interacting waves are tilted so as to match the projection of the group-velocities on any given direction. Ref. [42] discusses this generalized approach for birefringent phasematching in detail. QPM lifts the constraints of particular material dispersion on the phase-matching condition, and allows for broader application of this technique for many wavelengths.

To illustrate this generalized approach, we follow a similar approach to Ref. [42] and compute the group velocities of the interacting waves as projected on the direction

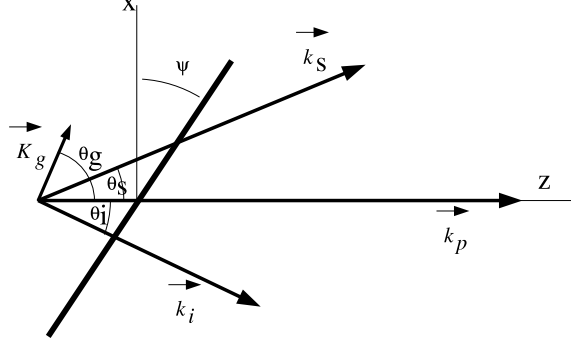


Figure 4.17: Diagram of three-wave mixing with tilted pulse fronts for group-velocity mismatch compensation. The pump, signal, and idler ( $\mathbf{k}_p$ ,  $\mathbf{k}_s$ ,  $\mathbf{k}_i$ ) vectors are shown, along with the tilted pulse front (bold black line) of all three waves. The pulse fronts are tilted such that the projection of the group-velocities on any given direction (e.g. the direction of the pump wavevector) are matched.

of the pump wave, defined in this section as the  $z$  axis. The group velocity of the pump is given by

$$\frac{1}{u_{p,z}} = \left. \frac{\partial k}{\partial \omega} \right|_{\omega_p}. \quad (4.69)$$

The projection of the group velocities of the signal and idler follow from geometrical arguments:

$$u_{s,z} = \left( \left. \frac{\partial k}{\partial \omega} \right|_{\omega_s} \right)^{-1} [\cos \theta_s - \tan \psi \sin \theta_s] \quad (4.70)$$

and

$$u_{i,z} = \left( \left. \frac{\partial k}{\partial \omega} \right|_{\omega_i} \right)^{-1} [\cos \theta_i - \tan \psi \sin \theta_i]. \quad (4.71)$$

The phase-matching condition along this same axis is written as

$$\Delta k_z = 0 = k_s \cos \theta_s + k_i \cos \theta_i - k_p + K_g \cos \theta_g, \quad (4.72)$$

and the phase-matching condition must also be met along the orthogonal (dispersed)

$x$ -direction:

$$\Delta k_x = 0 = k_s \sin \theta_s + k_i \sin \theta_i + K_g \sin \theta_g, \quad (4.73)$$

For given pump and signal frequencies, QPM period, and QPM angle ( $\theta_g$ ), we can set the group velocities  $u_{p,z}$ ,  $u_{s,z}$ , and  $u_{i,z}$  equal to each other and use the above five equations, in combination with the relation  $\omega_p = \omega_s + \omega_i$ , to compute the idler frequency  $\omega_i$ , and the angles  $\theta_s$ ,  $\theta_i$  and  $\psi$ .

One example of interest is that of high-gain OPA with a CW or long-duration pump pulse; where only the signal and idler group-velocities are matched using this technique, and the pump pulses may be untilted provided they are of long enough duration that the signal and idler fields do not experience significant walkoff. In this manner, the amplification bandwidth is broader due to angular dispersion of signal and idler waves. Similar geometries in birefringent crystals have demonstrated dramatically broader amplification bandwidths when compared with collinear OPA[76, 77].

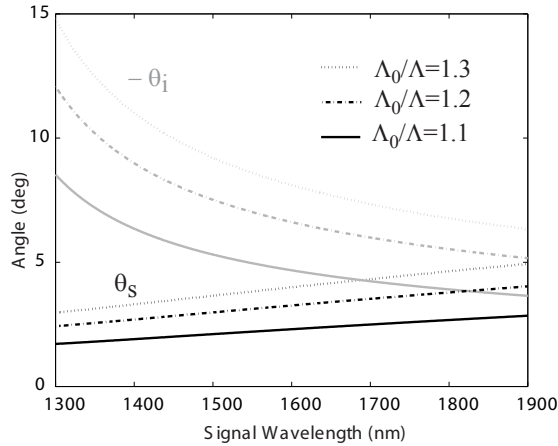


Figure 4.18: Angle of signal and idler beams in tilted pulse-front optical parametric amplification versus wavelength. We assume a pump wavelength of 1064 nm, and a QPM grating vector that is parallel to the pump wave ( $\theta_g = 0$ ). Different curves are plotted for different values of the QPM period  $\Lambda$ , given as a fixed ratio of the nominal QPM period  $\Lambda_0$  for the plotted signal wavelength.

Figs. 4.18 and 4.19 show calculated beam angles and pulse-front tilt angles for

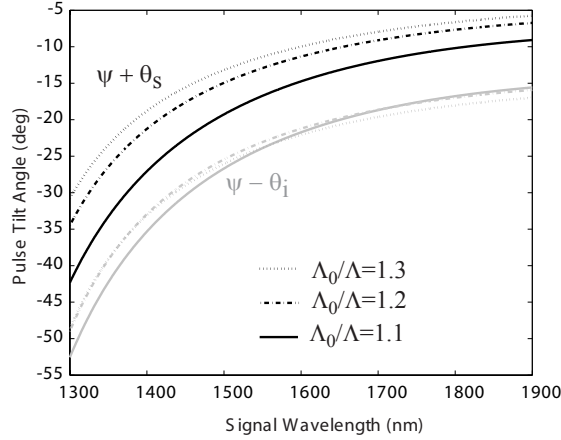


Figure 4.19: Pulse-front tilt of signal and idler pulses (given relative to the propagation direction of the associated beam) for group-velocity mismatch compensated OPA associated with the calculated angles plotted in Fig. 4.18. The spectral angular dispersion may be calculated from Eq. (4.9).

signal and idler versus signal wavelength for group-velocity compensated parametric amplification in periodically poled lithium niobate. Note that only periods shorter than the collinear QPM period work for noncollinear phase-matching; this is evident from simple geometry. For collinear QPM, the nominal QPM wavevector  $K_0$  meets the condition  $\pm|\mathbf{K}_0| = |\mathbf{k}_3| - |\mathbf{k}_1| + |\mathbf{k}_2|$ . (the positive sign is taken if  $|\mathbf{k}_3| - |\mathbf{k}_1| + |\mathbf{k}_2| > 0$ , or the negative sign if  $|\mathbf{k}_3| - |\mathbf{k}_1| + |\mathbf{k}_2| < 0$ ) For noncollinear QPM, the four vectors  $\mathbf{k}_3$ ,  $\mathbf{k}_2$ ,  $\mathbf{k}_1$ , and  $\mathbf{K}_g$  form a closed quadrangle. Such a closed quadrangle may only be constructed if  $|\mathbf{K}_g| \geq |\mathbf{K}_0|$ .

In Figs. 4.18 and 4.19 we assume a pump wavelength of 1064 nm and disregard the pump group velocity, effectively assuming pump pulses much longer than the incident signal pulse. In OPA with a CW (or long-duration) pump pulse, the amplification bandwidth is limited by the signal-idler group-velocity mismatch. Compensating the group-velocity mismatch using tilted pulse fronts of the signal and idler waves has been used effectively to broaden the amplification bandwidth [76, 77, 78, 79].

A complete analysis of the gain and associated tradeoffs, similar to that in Sections 4.5 through 4.10 for SHG, has not yet been developed for the case of OPA; however,

the physical limitations to this technique (spatial walkoff, effective GVD) are expected to be similar to those of its application to SHG. The mathematical analysis in the case of high-gain OPA is more complicated than for the case of SHG discussed in this chapter, since even in the undepleted pump limit the solution must be extracted for two coupled nonlinear differential equations representing the evolution of signal and idler waves. Nevertheless, in the future a thorough theoretical analysis of this technique as applied to OPA may result in a more complete understanding of the associated benefits and tradeoffs as compared to other techniques for ultrashort-pulse parametric amplification in a similar comparison as was discussed in Section 4.10 for the case of SHG.

We can estimate the parametric gain for this geometry using the scaling results from the SHG analysis. The SHG conversion efficiency is equal to the undepleted-pump conversion efficiency in the limit of plane, monochromatic waves averaged over a Gaussian spatio-temporal envelope, provided that the interaction length is shorter than both the aperture length and the effective dispersion length. Sections 2.4 and 2.5 showed that in the limit of plane, monochromatic waves the SHG conversion efficiency and the logarithmic amplitude gain for OPA are related by

$$g_{OPA} = \frac{L}{L_G} = \sqrt{\eta_{SHG}}, \quad (4.74)$$

where  $E_0$  in the definition of the mixing length  $L_G$  represents the pump field amplitude instead of the FH field amplitude when describing OPA. The logarithmic parametric power gain can be estimated using the optimized SHG conversion efficiency, assuming that the signal-idler phase-matching angle and the beam waist are chosen such that the aperture length and effective dispersion lengths are approximately equal to the interaction length. Here, the effective dispersion is that of the signal (or idler) wave, since the pump is assumed CW. The logarithmic power gain is therefore approximately given by

$$g_{OPA} = \sqrt{\eta_{opt}} = 11.9 \sqrt{\frac{d_m^2}{\epsilon_0 c \delta \nu n_2 n_1 \lambda_1^3} \frac{P_0}{\Delta \omega_1}}, \quad (4.75)$$

where  $P_0$  is the pump power,  $\Delta\omega_1$  is the signal bandwidth, and  $\delta\nu_{1,2}$  is the signal-idler GVM parameter. Since a short, uniform nonlinear crystal chosen to optimize the gain at a fixed bandwidth also follows approximately the monochromatic plane-wave scaling, there once again should be no significant advantage in gain when using a noncollinear geometry with spectral angular dispersion.

Parametric gain in a chirped QPM grating, however, does not scale the same as for plane, monochromatic waves. For comparison, we can compute the logarithmic power gain for a chirped grating with the same amplification bandwidth according to Ref. [30], and assuming confocal focusing we have

$$g_{OPA}^{CG} \approx 12.8 \frac{d_m^2}{\epsilon_0 n_3 n_2 c^3} \frac{\omega_1 \omega_2}{\lambda_1 \delta\nu_{1,2}} \frac{P_0}{\Delta\omega_1} = 3.6 g_{OPA}^2. \quad (4.76)$$

Note that the logarithmic gain in the case of a chirped QPM grating scales as the square of the gain for noncollinear phase-matching using spectral angular dispersion when ideal focusing conditions are assumed. As a result, for the same amplification bandwidth a chirped grating will almost always result in higher parametric gain under ideal focusing conditions.

## 4.12 Summary of Chapter 4

In this chapter we discussed the demonstration of frequency doubling of ultrashort pulses using spectral angular dispersion and a non-collinear geometry to eliminate the effects of group-velocity mismatch. This experiment demonstrates SHG of pulses 138 fs in duration at a FH wavelength of 1550 nm in a PPLN crystal many times longer than the group-velocity walkoff length with negligible loss of SHG bandwidth.

A theoretical model for group-velocity matched SHG in quasi-phase-matched materials that includes the effects of dispersion, diffraction, and spatial walkoff is also discussed. The diffraction of a strongly tilted pulse is treated as an effective dispersion, and a solution for the output second-harmonic field envelope is presented for the case of a Gaussian FH pump pulse. The diffraction of a strongly tilted pulse envelope is separated into the diffraction of the beam and an effective dispersion that results

from the pulse-front tilt. The second-harmonic bandwidth may be limited by mismatch in the group-velocity dispersion or in the effective dispersion resulting from the diffraction of a tilted pulse. The total effective dispersion mismatch is characterized by a dispersion mismatch parameter  $\delta_D$ , which should have less than unit magnitude to preserve the bandwidth of SHG. If  $\delta_D \ll 1$ , spatial walkoff and dispersion do not affect the frequency content of SHG, and affect only the amplitude and/or beam shape.

The effective dispersion resulting from a tilted pulse-front, combined with the effects of spatial walkoff, results in a reduced conversion efficiency characterized by an efficiency reduction factor. The efficiency reduction factor affects the optimum focusing condition and phase-matching angle for peak conversion efficiency. This optimum is found where the phase-matching angle, inversely proportional to the pulse-front tilt, is chosen such that the effective dispersion resulting from the diffraction of a tilted pulse has a characteristic length equal to 0.58 times the interaction length. In addition, the beam size is chosen to balance the trade-off between increasing conversion efficiency and increased distortions in the beam shape and quality due to spatial walkoff. A reasonable balance is found when the aperture length is approximately 1/3 the interaction length.

The best achievable conversion efficiency for non-collinear SHG with spectral angular dispersion is independent of the interaction length, and is approximately equal to the conversion efficiency for other methods of ultrashort-pulse SHG under ideal focusing conditions.

# Chapter 5

## Engineering of multi-color spatial solitons with chirped-period quasi-phase-matching gratings in optical parametric amplification

### 5.1 Introduction

In Section 1.4 we discussed the technique of chirped-pulse optical parametric amplification for the amplification of ultrashort optical pulses. While we highlighted many advantages of OPA as compared to laser amplification, we also discussed the challenge of achieving efficient OPA with non-uniform pump beams. This challenge arises not only from non-uniform gain that is associated with the spatial intensity of the pump, but from cascaded frequency conversion in which generated signal-idler pairs may convert back to pump photons through sum-frequency generation.

While cascaded frequency conversion may limit the efficiency of parametric amplification, in Section 2.7 we also showed that in cascaded three-wave mixing, when all interacting waves are of comparable amplitude and strongly coupled together, that

stable non-diffracting spatial solitons exist, and propagate without change in amplitude. Spatial solitons are nonlinear eigenstates of three-wave mixing which have approximately Gaussian envelopes that depend on the wavevector mismatch. Since the effective wavevector mismatch may be manipulated through quasi-phase-matching, the properties of spatial solitons may be tailored with QPM engineering – even in an effort to reach uniform depletion of the pump wave in a parametric amplifier.

In this chapter, we demonstrate the engineering of spatial solitons excited in optical parametric amplification through the use of chirped-period QPM gratings. Solitons may be tailored with chirped QPM gratings to have high signal-idler content and very little pump, thus representing a technique for achieving high conversion efficiency in a parametric amplifier even in the presence of cascaded frequency mixing.

## 5.2 Efficient parametric amplification with solitons

Quasi-phase-matching (QPM) engineering allows tailoring of the properties of parametric amplification, including the regime of quadratic soliton generation where the signal, idler and pump waves propagate mutually trapped and locked together with high-quality beam modes as in spatial solitons. The tunability afforded by QPM allows for engineering of the soliton launching efficiency and the soliton properties [80, 81], since soliton properties depend on the wavevector mismatch as shown in Fig. 2.4. Soliton tailoring has been observed through inhomogeneous phase-matching induced, e.g., by temperature gradients [82]. Generating solitons in a parametric amplifier and exploiting the properties of solitons subject to a changing local wavevector mismatch in a chirped QPM grating was shown theoretically to allow increased conversion efficiency [83]. Continuous-wave numerical simulations indicate that photon conversion efficiencies of 90% are possible with this technique. Moreover, it was shown to be relatively insensitive to changes in pump power and signal frequency, making it applicable to the amplification of short pulses in a chirped-pulse optical parametric amplifier. Generation of quadratic solitons in parametric amplification and parametric generation was demonstrated [84, 85], and high gain in an CPOPA system under conditions suitable for soliton formation featuring a photon conversion efficiency of

46% has been observed [86]. In this chapter, we demonstrate the manipulation of soliton properties through OPA in a chirped QPM grating in periodically poled lithium niobate (PPLN) and show the essential features of the efficiency-enhanced parametric amplifier put forward in Ref. [83].

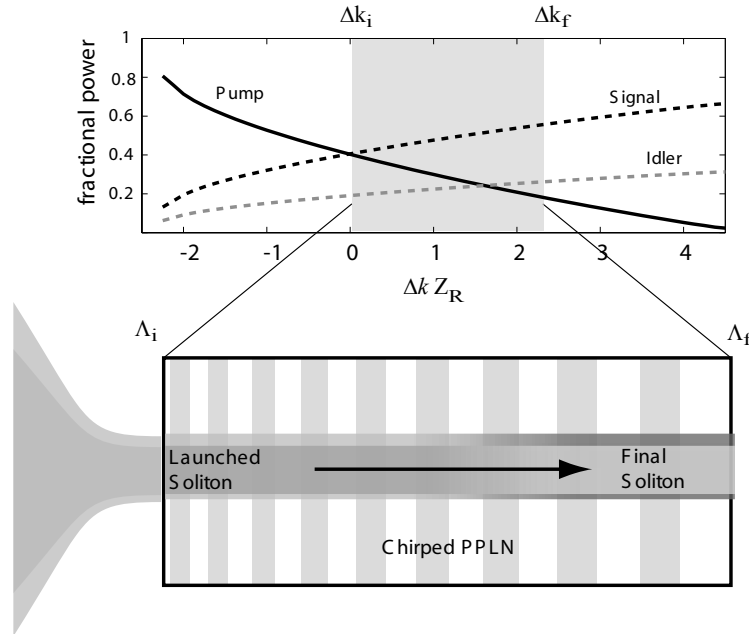


Figure 5.1: Soliton parametric amplification with chirped gratings. The graph shows the power sharing between the component waves of an exact multi-color soliton as a function of wavevector mismatch, normalized to the pump beam diffraction length  $Z_R$  ( $Z_R = 5.1$  mm in this experiment), for a soliton with 6 kW of total power. The bottom schematic shows how these properties can be mapped onto a chirped QPM grating.

The concept of chirped-grating soliton parametric amplification is illustrated in Fig. 5.1. The distribution of power between the signal, idler, and pump waves in a soliton is a function of wavevector mismatch (see Fig. 2.4), defined as  $\Delta k = k_1 + k_2 - k_3 + K_g$  where  $k_i$  is the wavevector for the signal ( $i = 1$ ), idler ( $i = 2$ ), or pump ( $i = 3$ ) wave, and  $K_g = 2\pi/\Lambda$  is the grating vector of a QPM grating defined in terms of the QPM period  $\Lambda$ . The condition desirable for maximum conversion to signal/idler pairs in a soliton occurs when  $\Delta k \gg 0$ ; however, the condition for

low soliton excitation threshold is  $\Delta k \approx 0$  and the highest launching efficiency in OPA occurs at a slightly negative  $\Delta k$  [87] according to the CW model. A chirped QPM grating utilizes a  $z$ -dependent ( $z$  is defined as the spatial coordinate along the propagation direction) grating wavevector  $K_g(z)$ , defined by the local QPM period  $\Lambda(z)$ . The chirped QPM structure allows for  $\Delta k \approx 0$  at the incident face of the nonlinear crystal for large launching efficiency, and a smooth transformation that follows the local wavevector mismatch to solitons at  $\Delta k \gg 0$  at the end for maximum conversion efficiency.

### 5.3 Experimental results

We demonstrate the tailoring of soliton states in chirped PPLN gratings using the experimental setup shown schematically in Fig. 5.2. The pump laser in this experiment is a JDS Uniphase PowerChip laser, a passively Q-switched Nd:YAG microchip laser that supplies pump pulses 500 ps long up to 50  $\mu\text{J}$  in energy at a repetition rate of 1 kHz and a wavelength of 1064 nm. The continuous-wave signal is at a wavelength of 1553 nm with approximately 3 mW of output power. The pump and signal beams are combined using a dichroic mirror and focused to a spot size ( $1/e^2$  diameter) of 55  $\mu\text{m}$  at the input face of a 5-cm-long PPLN crystal. The 5-cm-long PPLN crystal used in this experiment is 10 times longer than the diffraction length for a 55- $\mu\text{m}$ -wide Gaussian beam. The pump beam in this experiment was measured to have a beam quality factor  $M^2 = 1.5$ , indicating faster divergence than the equivalent-width Gaussian TEM<sub>00</sub> beam.

The output light is separated, using a second dichroic mirror, into signal and pump beams. The exit face of the PPLN crystal is imaged using separate cameras for the component waves: a silicon camera for the pump, and an InGaAs camera for the signal. The energies of the pump and signal waves are measured using integrating photoreceivers that are time-gated in order to reject energy in the un-amplified CW signal that is present between pump pulses. No measurements were made on the idler wave.

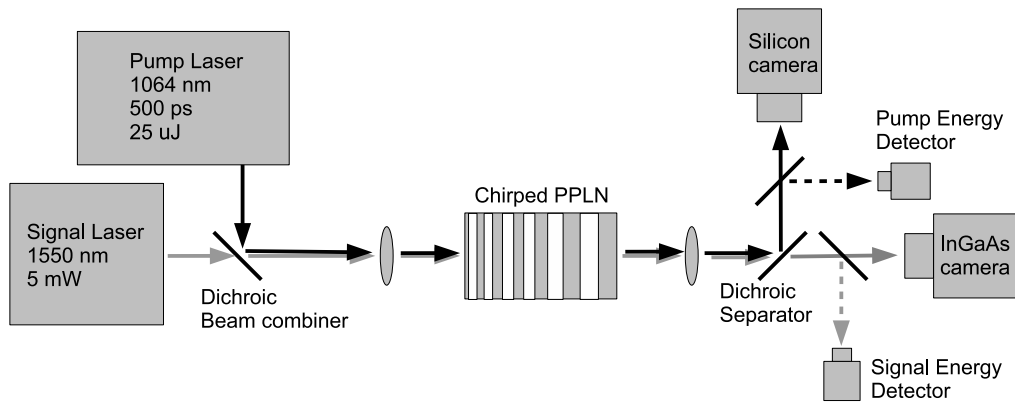


Figure 5.2: Experimental setup for the measurement of quadratic spatial solitons in optical parametric amplification. Pump and signal lasers are focused at the input face of a PPLN crystal to a spot size ( $1/e$  intensity half-width) of  $20 \mu\text{m}$ . The exit face is imaged using separate cameras for the pump and signal beams, and the energy of the pump and signal is detected using integrating photoreceivers. No measurements are made on the idler wave.

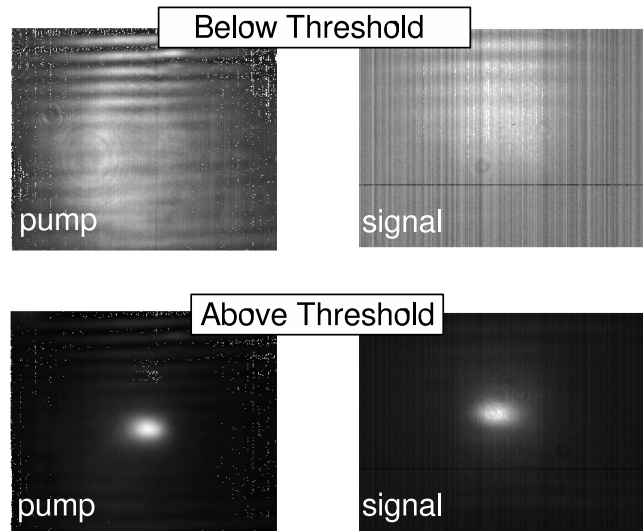


Figure 5.3: Images of soliton formation in optical parametric amplification in PPLN. Top: Images of pump and signal beams at the exit face of a PPLN crystal many diffraction lengths long show a large spatial intensity distribution, and fringes resulting from total internal reflection in a 0.5-mm-thick PPLN sample. Bottom: At high intensities, mutual self-trapping occurs due to the interaction of pump, signal, and idler (not shown) beams such that a small beam spot appears at the exit face of the nonlinear crystal. The width of this spot ( $55 \mu\text{m}$ ) is approximately the same as the focal spot at the input face despite the fact that the crystal is much longer than the diffraction length.

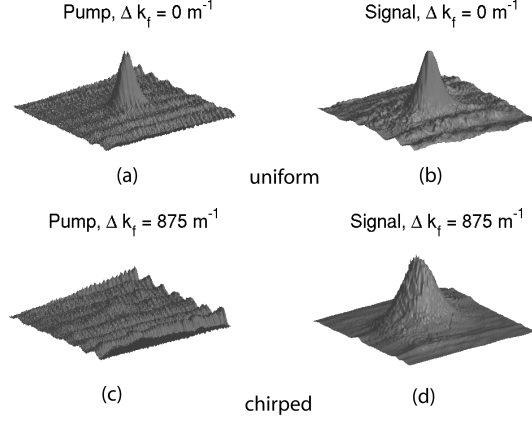


Figure 5.4: Engineered solitons. Top: surface plots show spatial intensity profile of pump (a) and signal (b) components of a multi-color soliton at the output of a uniform grating with  $\Delta k = 0$ . Bottom: Surface plots of pump (c) and signal (d) waves at the output of a chirped grating with initial wavevector mismatch  $\Delta k_i = 0$  and final mismatch  $\Delta k_f = 875\text{m}^{-1}$ .

Sample images of the pump and signal beams above and below the soliton threshold are shown in Fig. 5.3. Below threshold, the large spatial intensity distribution that results from diffraction-dominated propagation is shown. Since the crystal length is 10 times the diffraction length of the pump beam, the pump beam diameter is large, and interference fringes are apparent as the beam experiences total internal reflection on propagation inside the 0.5-mm-thick PPLN crystal. Similarly, the signal wave also spreads due to diffraction. With high pump power, focusing effects due to nonlinear frequency mixing result in a much smaller spot size for both the pump and signal waves at the exit face of the nonlinear crystal. The soliton threshold is defined as the pump power for which the spot size at the exit is approximately equal to the size at the crystal input face; in our experiments the threshold at  $\Delta k = 0$  has been measured to be 30-35 kW (approximately 15-17.5  $\mu\text{J}$  for our 500-ps pump pulses) corresponding to a soliton size approximately  $55 \mu\text{m}$  in  $(1/e^2 \text{ intensity})$  diameter.

Fig. 5.4 compares the spatial intensity distribution of a soliton measured in a uniform grating at  $\Delta k = 0$  to a soliton in a QPM grating chirped to a final mismatch of  $\Delta k_f = 875\text{m}^{-1}$ . The soliton at the output of the chirped grating has most of its

energy in the signal and idler components with reduced pump intensity as compared to the uniform grating. Fringes are observed on the background of the image as a result of total internal reflection of non-soliton fields at the surface of the 0.5-mm-thick PPLN samples.

In order to quantify the behavior for several chirped gratings, it was necessary to distinguish the soliton content in the output beam from unguided pump and signal light. Using the captured images of the pump and signal spatial modes, a circular digital mask is defined; centered at the peak of the soliton mode, and with a radius approximately twice the soliton radius. The sum of all pixel values inside this soliton radius divided by the sum of all pixels in the image is equal to the soliton energy divided by the total energy, and this ratio can be used with the measured total energy to calculate the soliton content. The soliton energy in pump and signal waves is measured for several chirped gratings, all with initial mismatch  $\Delta k_i = 0$  (QPM period  $\Lambda_i = 29.56\mu\text{m}$ ) and final wavevector mismatch ranging between  $\Delta k_f = -1000\text{m}^{-1}$  ( $\Lambda_f = 29.70\mu\text{m}$ ) and  $\Delta k_f = 1000\text{m}^{-1}$  ( $\Lambda_f = 29.44\mu\text{m}$ ).

The central result of this experiment is shown in Fig. 5.5. The top graph shows the measured total soliton energy versus the final wavevector mismatch for a number of chirped gratings, all with  $\Delta k = 0$  at the input of the chirped PPLN crystal. The bottom plot shows the fraction of soliton energy carried by the pump (crosses) and signal (circles) components. For comparison, the results of numerical beam propagation of the CW coupled equations (Eqs. (2.47) through (2.49)) assuming radial symmetry are also plotted. The temporal shape of the pump pulse was included by averaging the results of CW propagations over a Gaussian temporal envelope. The conditions mimic the experimental conditions, with the exception that the numerical simulations use a Gaussian pump field with an energy of  $8\mu\text{J}$  to yield a soliton energy of  $4\mu\text{J}$  similar to that measured in the experiment.

The data in Fig. 5.5 shows clearly that chirped gratings may be used to tailor the fractional power in OPA solitons, but falls short of the ideal behavior of the efficiency-enhanced soliton parametric amplifier shown schematically in Fig. 5.1. Even if all of the ( $\approx 4\mu\text{J}$ ) soliton energy is efficiently converted to signal-idler pairs, this still represents a small fraction of the incident pump energy ( $\approx 23\mu\text{J}$ ). The continuous

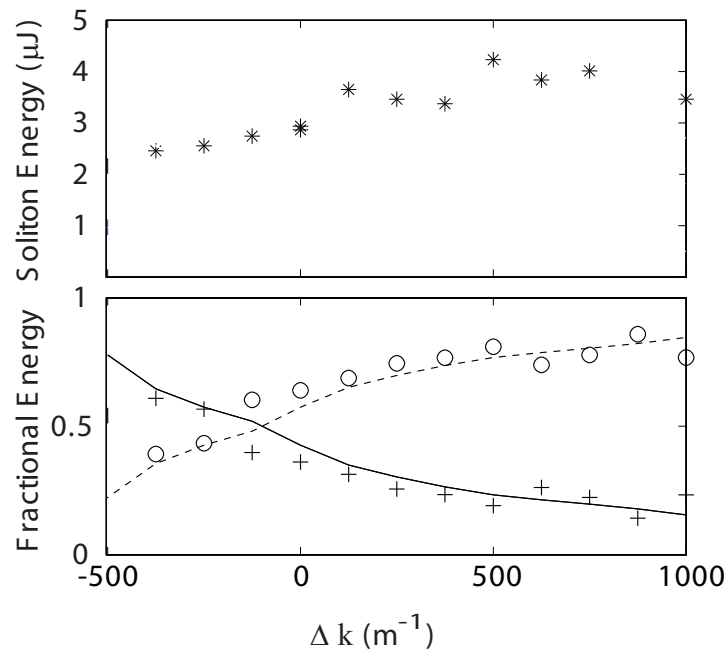


Figure 5.5: Measured properties of engineered solitons. Top: Measured total soliton energy versus final wavevector mismatch. The initial mismatch in all cases is  $\Delta k = 0$ . Bottom: Fractional energy, defined as the signal (circles) or pump (crosses) energy divided by the sum (signal + pump) energy. Lines (dotted line for the signal fraction, solid line depicts the pump) represent the calculated prediction for solitons with total energy of 4  $\mu\text{J}$  resulting from numerical simulation.

wave model discussed in Section 2.7 suggests that the soliton content for the chirped gratings used in this experiment should be approximately 50%, or a pump energy of only 8  $\mu\text{J}$  should be required to produce the observed 4  $\mu\text{J}$  solitons.

The plots in Fig. 5.5 span the entire existence region of solitons which have a spot size equal to the focused beam size at the incident face of the PPLN device. Measurement at larger negative values of the final wavevector mismatch resulted in the observation of amplified parametric noise near wavelengths of 1562 nm, far from the signal seed wavelength of 1553 nm. The parametric noise in crystals with such large negative chirp was at a level greater than the signal seed power, and might be expected since OPA solitons at the seed signal wavelength cannot exist at larger values of the final wavevector mismatch than  $-500 \text{ mm}^{-1}$ . Parametric noise at small amplitudes ( $\leq 10$  dB below the CW signal amplitude) was observed in the experiments corresponding to the data in Fig. 5.5. More detailed measurements of parametric noise and a discussion of its influence on these and similar experiments are presented in Chapter 6.

The pump energy required to launch a soliton was between 23 and 25  $\mu\text{J}$ . At this pump power, soliton energies between 2 and 6  $\mu\text{J}$  are measured, resulting in soliton content (defined as the soliton energy divided by the total incident energy) between 8% and 26% near the soliton threshold for  $\Delta k = 0$ . Numerical simulations for ideal pulse and beam quality conditions predict soliton content in excess of 50%. The soliton energy at threshold is consistent with the numerical simulations, but the observed pump power required to excite solitons is thus higher than expected. This difference is likely influenced by the poor beam quality in this experiment, as shown by recent measurements where the soliton threshold was observed to substantially increase with increasing pump beam quality factor ( $M^2$ )[88], and is also influenced by the presence of parametric noise.

In Chapter 6 we discuss in detail the influence of parametric noise on soliton excitation and propagation. Although the amplitude of parametric noise is below the level of the seed signal for the experimental data plotted in Fig. 5.5, the total energy integrated over the broad bandwidth can be a significant fraction of the total signal radiation, and influences the efficiency of soliton excitation. We show in Chapter 6

that parametric noise accounts for most of the difference between the observed pump energy of  $23 \mu\text{J}$  and the calculated (using the CW model) energy of  $8 \mu\text{J}$  required to excite solitons with  $4 \mu\text{J}$  of energy in these experiments. Furthermore, the top plot of Fig. 5.5 shows that the soliton energy is not constant as the final wavevector mismatch varies, but decreases as  $\Delta k$  becomes more negative – in contrast to the CW model, which suggests that it should follow the opposite trend and increase slightly for negatively chirped gratings. This, too, may be explained by including amplified parametric noise and is discussed in detail in Chapter 6.

## 5.4 Summary of Chapter 5

In this chapter, engineering of solitons is shown in OPA through the use of a chirped QPM grating; generating solitons near phase-matching where the launching soliton efficiency is close to optimum, and using a linearly-chirped QPM grating to transform the energy sharing of the soliton to a more favorable value determined by the local wavevector mismatch. This behavior demonstrates the essential features of an efficiency-enhanced soliton optical parametric amplifier.

Figures 5.4 and 5.5 confirm that the amount of signal (and idler) light carried by a spatial soliton may be tailored through the use of a chirped QPM grating. However, even if all of the ( $\approx 4 \mu\text{J}$ ) soliton energy is converted to signal-idler pairs, in this experiment it represents a small fraction of the incident pump light ( $\approx 23 \mu\text{J}$ ) such that a truly high-efficiency soliton parametric amplifier has yet to be demonstrated. The low observed soliton energy is below that which CW theory predicts, and to more completely understand the nature of this observation, we must depart from the CW model and include the effects of parametric noise. The next chapter is dedicated to this departure, and discusses the influence of parametric noise on the generation and propagation of spatial solitons in a parametric amplifier.

# Chapter 6

## Excitation of quadratic spatial solitons in the presence of parametric noise

### 6.1 Introduction

The generation and propagation of spatial solitary waves in quadratic nonlinear media has been studied extensively, and in recent years multicolor solitons have been experimentally demonstrated in a variety of nonlinear materials in both frequency up-conversion (second-harmonic generation) and down-conversion (optical parametric amplification)[89, 84, 90, 91, 92, 85, 93, 94]. A variety of applications of QPM engineering to the manipulation and tailoring of spatial solitons have been proposed and demonstrated [95, 96, 97, 83, 98].

In Chapter 5 we showed spatial solitons can be tailored using non-uniform (chirped) QPM structures. The experimental data in Chapter 5, however, suggests that the observed soliton content is lower (or, rather, the observed excitation threshold is higher) than the CW model of Section 2.7 predicts. In this chapter, we discuss the influence of parametric noise on soliton excitation and propagation, including experiments similar to those in the previous chapter. We show that over short propagation distances, amplified noise results in the observation of lower soliton content than the noiseless

model predicts, and accounts for much of the difference between the experimental results of Chapter 5 and both the CW and noiseless predictions. (We note that even with pulsed inputs, a noiseless model results in predictions remarkably close to the CW model of Section 2.7 when the total group delay between the interacting fields is much less than the pulse duration, as noted in Ref. [99]. For cases with small group-velocity mismatch and no noise, a CW model with the same average input power as the pulsed signal, idler, and pump fields is typically sufficient to describe the essential physics.) Furthermore, we show that over long propagation distances, parametric noise inhibits the spatially-confined propagation characteristic of noiseless solitons, suggesting that the noiseless (CW) description is valid over limited propagation distances. The differences between observed soliton behavior in the presence of noise and the predictions of the CW model are not altogether surprising since parametric noise can not be treated in the same manner as continuous-wave radiation.

Spatial confinement through cascaded second-order nonlinearities is predicted in the existence of stationary solutions to CW coupled equations describing the interaction between three monochromatic waves interacting in a nonlinear medium [100, 101, 59], as discussed in Section 2.7. Since the coupled wave equations governing three-wave mixing are not completely integrable, numerical techniques are required to investigate the excitation and propagation of multicolor spatial solitons [102, 87]. Typically, such numerical calculations involve the simulation of beam propagation along the propagation dimension with monochromatic waves allowed to vary in two transverse dimensions such that the dimensionality may be denoted as (2+1)-D (or when comparing with experiments in which confinement in one transverse dimension is provided by a conventional planar waveguide, one transverse dimension may be considered and denoted as (1+1)-D).

Recently, experiments demonstrated that the noiseless description may not be sufficient to adequately describe soliton behavior when excited by spontaneous parametric generation [103]. Temporal noise was shown to seed temporal breakup and subsequent spoiling of the spatial confinement of a large fraction of the incident pump radiation. Better agreement with experiment was found when compared with a quasi-(3+1)-D model, in which the temporal envelope and the associated dispersion were

considered. (The quasi-(3+1)-D model assumes radial symmetry in the two transverse dimensions, as compared with a true (3+1)-D model.) A remarkable feature of this experiment is the profound influence of dispersion (group-velocity mismatch as well as group-velocity dispersion) despite the relatively small amount of net temporal walkoff (0.25 to 0.5 times the pulse duration) and group-delay dispersion ( $10^{-2}$  to  $10^{-3}$  times the pulse duration).

This chapter extends this discussion to optical parametric amplification, in which vacuum noise (the equivalent input signal of spontaneous parametric downconversion) grows despite the injection of a monochromatic signal wave. Parametric noise is shown to affect the spatial confinement and consequently the efficiency of soliton excitation at both zero and non-zero wavevector mismatch. The growth of parametric noise explains the large difference between the observed and expected (from the noiseless model) soliton content presented in Section 5.3, and influences the utility of the efficiency-enhanced soliton parametric amplifier presented in Chapter 5.

The rest of this chapter addresses departures from the CW model of Section 2.7 due to amplified parametric noise. In Section 6.2 we discuss some simple physics of amplified parametric noise in the context of soliton generation, and how it may be expected to influence the excitation and propagation of self-trapped waves excited by parametric amplification. In Section 6.3, we revise the noiseless model to include parametric noise, including alterations to the relevant coupled equations and a simple estimate of the power and bandwidth of an equivalent parametric noise field for the purposes of numerical simulation.

In Section 6.4 we present the results of experiments in which spatial solitons are excited in parametric amplification under a variety of conditions, and demonstrate agreement with numerical simulations. The growth of parametric noise affects the frequency content of the propagating light, as well as the nonlinear beam confinement characteristic of spatial solitons, demonstrating a marked departure from the noiseless model. The data in this section is consistent with the data in Section 5.3, which demonstrated similar departures from the CW model of Section 2.7.

Section 6.5 extends the discussion of experiments in Section 6.4 to experiments

with variable signal input power. In Section 6.6 the numerical simulation of near-ideal launching conditions demonstrates that parametric noise grows not only in the excitation of spatial solitons under conditions where the input fields are far from the soliton states, but also under conditions when the input fields are nearly matched to the spatial soliton state. This suggests that the propagation length of spatial solitons, predicted to propagate infinite distances by a CW model, may be limited in the presence of parametric noise. Section 6.8 summarizes the results of this chapter.

## 6.2 Parametric noise and its influence on soliton OPA

This section gives some simple physical insight into the influence of noise on the behavior of quadratic spatial solitons. Although a complete description of the excitation and propagation of quadratic spatial solitons is available only through comprehensive numerical treatments, this section describes some basic physics, which may aid in the understanding of the experimental and numerical results presented in later sections.

In a conventional seeded parametric amplifier, the presence of vacuum noise is typically neglected for several reasons: the equivalent noise power is typically far below the input signal seed, the interaction involving the seed signal is wave-vector-matched (or nearly wave-vector matched) so that all frequency components of the parametric noise experience gain at or below the level of gain of the seed signal, and the interaction is not saturated, so that significant back-conversion may be neglected.

In a quadratic spatial soliton, at least one, and in some cases all, of these assumptions may be inaccurate. The cascaded nonlinear interaction necessary for self-trapped behavior requires the consideration of saturated parametric amplification. With such strong nonlinear mixing it is possible, and sometimes desirable, to consider interactions for which the seed-signal wavelength may be different from the one meeting the wave-vector matching condition ( $\Delta k = 0$ ). For example, operation at non-zero wavevector mismatch was shown in Chapter 5 to allow tailoring of the soliton states for improved conversion to signal-idler pairs. In addition, excitation

at non-zero wavenumber mismatch has been shown theoretically (using a CW (2+1)-D model) to enhance the efficiency of soliton excitation [87]. Finally, in a high-gain parametric amplifier the effective noise input power may be comparable to the seed signal power. Spatial solitons have also been observed without any input seed signal, where vacuum noise is not only present but essential to soliton behavior [85].

Consider the propagation of a CW spatial soliton. We should expect a small noise signal at a nearby (still in the signal-idler amplification bandwidth) frequency to grow with propagation in the presence of a strong pump. If sufficiently off-axis, a generated signal (or idler) photon may soon leave the volume of the quadratic soliton before a subsequent nonlinear conversion takes place, thus representing a slow radiative loss mechanism to the confined single-frequency beam. If it remains in the propagation volume, we might expect that it continues to participate in nonlinear mixing, amplifying until it is at a comparable level to the seed signal and disturbing the signal integrity, or cascading to generate new nearby frequencies and further broadening the spectrum of signal and idler. Since vacuum noise is broadband and randomly phased, we may even expect temporal bunching to occur as many of these nearby frequencies are amplified and nonlinear phase shifts associated with cascaded second-order nonlinear interactions affect the temporal structure of interacting broadband fields. Eventually, they may form a spatially self-trapped entity that departs from the continuous-wave soliton description, similar to the formation of “red solitons” described in Ref. [103].

How quickly such a noise signal grows is expected to depend on the intensity of the pump light carried in the solitary wave, since it is the pump that drives the initial amplification of nearby signal (or idler) frequencies. Qualitatively, this suggests that we might expect to observe more noise amplification when  $\Delta k < 0$ , since the majority of power in a spatial soliton in this region is carried by the pump wave (see Fig. 2.4).

Another distinct difference between  $\Delta k > 0$  and  $\Delta k < 0$  may be visualized by considering the angular distribution of wave-vectors, as shown in Fig. 6.1. Since solitons are, by definition, of finite extent in the spatial domain, each temporal frequency component contains a distribution of waves propagating at slightly different angles. When  $\Delta k \geq 0$ ,  $\mathbf{k}_1 + \mathbf{k}_2 \geq \mathbf{k}_3 - \mathbf{K}_g$ . (Note, as defined in this chapter,  $\Delta k$

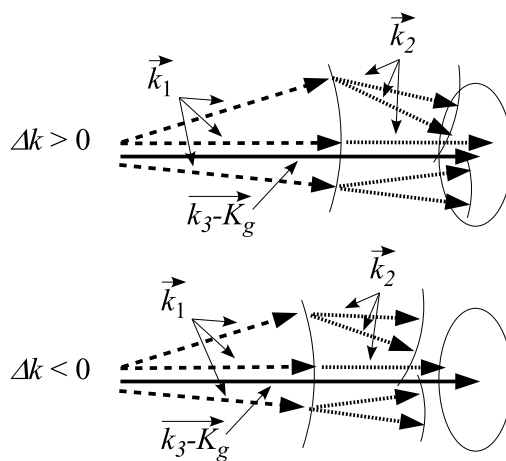


Figure 6.1: Wavevector diagram for  $\Delta k > 0$  (top) and  $\Delta k < 0$  (bottom) for a spatial distribution of signal ( $k_1$ ) and idler ( $k_2$ ) vectors. Simple geometric arguments demonstrate that when  $\Delta k > 0$  there are many configurations that result in amplification (represented schematically by the set of vectors  $\mathbf{k}_1 + \mathbf{k}_2$  which fall in the ellipse at the end of the vector  $\mathbf{k}_3 - \mathbf{K}_g$ ), while the  $\Delta k < 0$  case leaves a much smaller set of amplified signal-idler geometries, and none access the peak of the parametric gain, at the center of the gain ellipse.

is the *scalar* sum of vector magnitudes:  $\Delta k = k_1 + k_2 - k_3 + K_g$ .) In Fig. 6.1, the amplification bandwidth is represented by the ellipse, drawn at the end of the vector  $\mathbf{k}_3 - \mathbf{K}_g$ . In the CW case, when the magnitudes of  $\mathbf{k}_1$  and  $\mathbf{k}_2$  are fixed but directions are allowed to vary, many geometries may be drawn to lie inside the amplification bandwidth. As  $\Delta k$  is decreased and becomes negative, the number of angles that result in amplification is reduced until only the collinear case remains. Of course, broadband noise is not constrained to the single-frequency states of a seed signal (and the corresponding narrow-band idler), and as such there are many configurations for which noise photons may fill the available amplification bandwidth. This is particularly true when  $\Delta k < 0$ , and the seeded signal (and corresponding idler) cannot access the center of the amplification band where the gain is at its peak. Noise photons with frequencies different from the CW (or narrow-bandwidth, pulsed) seed signal are available for perfectly phase-matched amplification. This description is supported by experimental data in injection-seeded parametric generation presented in Ref. [104], where a high-gain parametric amplifier is seeded at the phase-matched signal frequency, but the measured spectrum of amplified radiation extends to longer wavelengths, for which  $\Delta k > 0$ .

While the above simplified description provides some qualitative insight, a full numerical treatment is necessary to describe quantitatively the behavior, particularly when many frequencies are considered simultaneously. Such a numerical treatment considers not only the angular distribution, but a distribution in magnitude, of the interacting wavevectors.

### 6.3 Parametric noise in nonlinear interactions

The consideration of broadband parametric noise necessitates two alterations to the CW model in Section 2.7: the allowance of multiple frequencies, or equivalently, the inclusion of time-dependence and dispersion; and the injection of a suitable equivalent noise at the input to mimic the source of parametric noise in physical experiments. In this section, we discuss the necessary changes to the CW model and the characteristics of an equivalent noise input.

Although the high peak powers required for soliton generation usually necessitate a pulsed interaction to maintain low average power, it is commonly assumed that if the interaction length is shorter than the characteristic length for group-velocity walkoff and group-velocity dispersion for the pulse duration employed in the experiment, that these time-dependent effects may be neglected. As discussed above, we expect that broadband frequency noise may influence the behavior of spatial solitons regardless of the pulse duration, and in fact, we will show experimental results in Section 6.4 that confirm this notion, even in the presence of net group-velocity walkoff less than 1% of the pump pulse duration (500 ps), and net group-delay dispersion less than  $10^{-7}$  times the pulse duration.

To allow numerical simulation of the effects of broadband frequency noise, time dependent terms must be introduced into Eqs. (2.47) through (2.49):

$$-i\sigma_1 \frac{\partial a_1}{\partial \xi} + \bar{\nabla}_\perp^2 a_1 - i\sigma_1 \frac{\partial a_1}{\partial \tau} - \sigma_1 \bar{\beta}_1 \frac{\partial^2 a_1}{\partial \tau^2} + a_2^* a_3 \exp(i\bar{\Delta}k\xi) = 0 \quad (6.1)$$

$$-i\sigma_2 \frac{\partial a_2}{\partial \xi} + \bar{\nabla}_\perp^2 a_2 - i\sigma_2 \delta_2 \frac{\partial a_2}{\partial \tau} - \sigma_2 \bar{\beta}_2 \frac{\partial^2 a_2}{\partial \tau^2} + a_1^* a_3 \exp(i\bar{\Delta}k\xi) = 0 \quad (6.2)$$

$$-i\sigma_3 \frac{\partial a_3}{\partial \xi} + \bar{\nabla}_\perp^2 a_3 - \sigma_3 \bar{\beta}_3 \frac{\partial^2 a_3}{\partial \tau^2} + a_1 a_2 \exp(-i\bar{\Delta}k\xi) = 0, \quad (6.3)$$

where  $\delta_2$  is defined as the ratio of the pump-idler to pump-signal group-velocity mismatch parameters

$$\delta_2 = \frac{\delta\nu_{2,3}}{\delta\nu_{1,3}}, \quad (6.4)$$

and  $\delta\nu_{i,j} = u_i^{-1} - u_j^{-1}$  is the group-velocity mismatch parameter, defined as the difference in reciprocal group velocities. Note that all group velocities are defined relative to the pump wave, so that there is no GVM term in Eq. (6.3). In this description, time has been normalized to  $\delta\nu_{1,3}Z_R$ , or the group-delay difference between pump and signal waves on propagating a distance equal to the soliton length  $Z_R$ . This characteristic time is approximately equal to the reciprocal of the DFG bandwidth for a CW pump, in the limit that  $\delta_2 = 0$ . As we will show in Sections 6.4 through 6.7, the influence of group-velocity mismatch may not be neglected even when the

pulse duration is much longer than the total group delay difference between the three interacting waves.

The normalized group velocity dispersion coefficient (see Eq. (2.13)) is

$$\bar{\beta}_i = \frac{1}{2Z_R \delta \nu_{1,3}^2} \left. \frac{\partial^2 k}{\partial \omega^2} \right|_{\omega_i}. \quad (6.5)$$

If we consider a pulse of normalized duration  $\tau_p$  and propagation over a normalized distance  $\xi_{max}$ , it is tempting to ignore dispersive effects if  $\delta_2 \xi_{max} / \tau_p \ll 1$  and  $\bar{\beta}_i \xi_{max} / \tau_p^2 \ll 1$  for signal, idler, and pump waves. However, since the presence of parametric noise can introduce temporal fluctuations on a time scale much less than  $\tau_p$ , this criterion for ignoring time-dependence may lead to misleading computational results.

To simulate the behavior of quadratic solitons in the presence of vacuum noise, we perform numerical beam-propagation simulation of Eqs. (6.1) through (6.3). In addition to the conventional input signal and pump fields, which have well-defined spatio-temporal envelopes, we add broadband noise near the signal frequency.

Although we expect the influence of parametric noise to depend only logarithmically on the input noise power, we must at least estimate this equivalent noise power in order to include it in a numerical simulation. Furthermore, the anticipated bandwidth of this noise will determine the sampling parameters of the numerical beam propagation, since we must sample enough points in the time domain to include the appropriate collection of frequencies. The power and bandwidth of parametric noise is discussed by Byer and Harris in Ref. [105]. Following their analysis, parametric noise has an equivalent differential signal input intensity of

$$dI_{OPG} = \frac{dP_{OPG}}{A_{eff}} = \frac{k^2 \hbar \omega c}{4\pi^2 n} dk \psi d\psi, \quad (6.6)$$

where  $A_{eff}$  is the effective area. To estimate the equivalent noise input power, this expression should be integrated over all possible magnitudes  $k$  of the OPG signal wavevector, and over all solid angles  $\psi$ . To compute an equivalent input signal field, we assert that  $dk$  may be replaced with  $\delta k = 2\pi n_1 \delta \lambda / \lambda_1^2$ , where  $\delta \lambda$  is the measured

bandwidth of parametric generation, at a center wavelength nearby the signal wavelength  $\lambda_1$ , so that  $\omega$ ,  $k$ , and  $n$  may be approximated as  $\omega_1$ ,  $k_1$ , and  $n_1$ , respectively. In the absence of a measured bandwidth, a lower bound is estimated in the limit of the difference-frequency generation (DFG) bandwidth for an interaction length equal to the diffraction length  $Z_R$ , such that  $\delta k \approx \pi/Z_R$  where  $Z_R$  is the Rayleigh length of the input pump beam, equal to  $k_3 r_0^2$ , and is approximately equal to the effective interaction length for soliton formation[64]. The associated frequency bandwidth is

$$\delta\omega = \delta k (\partial\Delta k/\partial\omega)^{-1} \approx \frac{\pi}{Z_R} \delta\nu_{1,2}. \quad (6.7)$$

In our experiment,  $\delta\lambda$  was measured to be approximately 10 nm. In the low-gain limit, the DFG bandwidth ( $\delta k \approx \pi/Z_R$ ) yields an estimate of 7 nm of amplified parametric noise bandwidth in the limit of low gain. Despite the fact that the peak powers are very high, the low-gain estimate appears sufficient for the self-trapped behavior present in a seeded soliton parametric amplifier, since the pump wave is strongly depleted.

To estimate the angular acceptance, we assert that only those wavevectors in the cone of divergence for a Gaussian beam equal in size to the soliton radius  $r_0$  are important, for which  $\theta_{max} \approx 1/k_1 r_0$ . The vacuum-noise equivalent intensity may now be expressed as

$$\frac{P_{OPG}}{A_{eff}} \approx \frac{\hbar\omega_1 c}{8\pi^2 n_1 r_0^2} \delta k. \quad (6.8)$$

If the injected noise signal has an effective area equal to the pump area, then  $A_{eff} = \pi r_0^2$ . Estimating the amplification bandwidth in the limit of low gain as being equal to the bandwidth of difference-frequency generation for a crystal of length equal to  $Z_R$  such that  $\delta k \approx \pi/Z_R$ , the noise power is

$$\frac{P_{OPG}}{A_{eff}} \approx \frac{\hbar\omega_1 c}{8n_1 Z_R}; \quad (6.9)$$

or, substituting in the measured noise bandwidth:

$$P_{OPG} \approx \frac{\hbar\omega_1 c \delta\lambda}{4\lambda_1^2}. \quad (6.10)$$

Using experimental quantities of  $\lambda_1 = 1555$  nm and  $\delta\lambda = 10$  nm the equivalent injected noise power is  $P_{OPG} \approx 1.6 \mu$  W. This may be compared with our seed signal of  $P_1(0) \approx 3$  mW, and an incident pump power of approximately 30 kW to generate solitons with  $r_0 = 20 \mu$ m, for a total soliton peak power of 6 kW.

## 6.4 Experimental results and comparison with numerical simulation

Experiments are conducted with an experimental setup identical to that shown in Fig. 5.2. In addition to the properties measured in Section 5.3, we measure the spectrum of the signal component at the output of the PPLN chip. The spectrum of the signal light was measured using a fiber-coupled optical spectrum analyzer. A fiber collimator (1-mm-wide graded-index lens packaged with an optical fiber) was placed at the image plane of the exit face of the PPLN crystal. The imaging magnification was 16:1, so that the effective soliton waist at the image plane was  $880 \mu$ m, corresponding to a  $55 \mu$ m  $1/e^2$  intensity diameter of solitons exiting the PPLN crystal. Since the diameter of the collimator is nearly the soliton diameter, we measure only the soliton light and spatially reject radiated non-soliton light.

We first report on signal noise in solitons generated through OPA in a uniform QPM grating with period  $29.564 \mu$ m (phase-matching wavelength was measured to be 1555nm at a temperature of approximately 150 degrees Celsius). By changing the signal wavelength we measured the soliton energy and spectra for several different values of  $\Delta k$  (defined relative to the seed signal wavelength). The pump energy of  $21 \mu$ J was 1.31 times the measured soliton threshold at  $\Delta k = 0$ . We compare this data with numerical simulations using Gaussian pulses with a normalized peak power of  $\bar{P}_3 = 627$  as defined in Eq. (2.50), equal to 1.3 times the numerically calculated soliton threshold, with a normalized signal power 60 dB below the pump. (The soliton threshold at  $\Delta k = 0$  was determined the same way in both the experiment and in calculation; by turning up the incident pump power until the time-averaged pump beam radius at the exit of our 5-cm-long ( $\xi_{max} = 10$ ) interaction was less than or

equal to the incident pump radius ( $1/e$  half-width =  $20 \mu\text{ m}$ ).

In both numerical simulations and experiment, in order to quantify the distinction between amplified signal and amplified noise, we define a 2-nm-wide window around our signal-seed wavelength. The integrated power outside this window is designated “noise”, and we define the noise content as the fraction of the total signal power lying outside this 2-nm-wide signal band. A 2-nm-wide window was chosen since it is narrower than the OPG bandwidth, as discussed in Section 6.2, but wider than the resolution of the optical spectrum analyzer which was increased from the minimum resolution to 1 nm due to the low average power coupled in from our experiment. The spectra were measured by averaging many ( $\approx 100$ ) pulses at each measured wavelength.

Numerical simulations were conducted assuming Gaussian pulses with 50-ps ( $1/e^2$  full-width) pulse duration, or  $\tau_p = 100$  (in comparison to the 500 ps experimental pulse duration), with 1000 sampling points per pulse width. The temporal point density must be chosen to accommodate the anticipated noise bandwidth, and with 500-ps pulse duration the required temporal samples would exceed 10000. Reducing the point spacing allowed us to significantly reduce the computation time. Since the characteristic time for the relevant dispersive effects is determined by the noise bandwidth and not by the temporal pulse duration, such a reduction does not significantly affect the outcome. This assertion was confirmed with a few representative cases where comparison between simulations of 500-ps pulses and 50-ps pulses showed no significant difference. With 50-ps pulses, the maximum temporal walkoff between the field envelopes was 5 ps, such that further reduction of the simulated pulse duration would result in a more significant fraction of the amplified signal pulse experiencing walkoff from the pump pulse. In the spatial domain, we use 8 sample points per beam width, and a maximum sampled radius of  $r/r_0 = 25$ . Absorbing boundary conditions were used (loss at  $r/r_0 \geq 20$ ) to eliminate reflections from the sampling boundary.

For the purpose of computation we define a noise field in the temporal- and spatial-frequency domain to have flat spectral amplitude, but phase that varies randomly between 0 and  $2\pi$  from point to point. As a result, the time-domain field has large amplitude fluctuations. The frequency-domain amplitude is defined such that there

is approximately the same amount of average intensity as predicted by Eq. (6.6). The point density must be high enough to accommodate the anticipated bandwidth of parametric amplification.

Noise is added to a Gaussian signal field in the time domain, and propagated with a quasi-(3+1)-D (along the  $\xi$  axis, considering temporal and radial effects; radial symmetry is assumed) iterative finite difference beam-propagation code[106, 107]. The assumption of radial symmetry in our calculations is expected to be valid near the soliton threshold; below the threshold for multi-soliton generation and other spatial modulational instabilities that may cause spontaneous radial symmetry breaking for spatial intensity fluctuations on a scale smaller than the beam width[88, 108]. It is expected that a true (3+1)-D model would result in more accurate computation; however, radial symmetry allows for more expedient computation, and for powers near (or below) the soliton threshold we expect the results of a radially-symmetric simulation to reflect the essential physics.

We calculated using the dispersion relation in Ref. [71] the normalized GVM parameter used in Eqs. (6.2) to be  $\delta_2 = 0.055$ . Likewise, the normalized GVD parameters are  $\bar{\beta}_1 = 1 \times 10^{-3}$ ,  $\bar{\beta}_2 = -8 \times 10^{-3}$ , and  $\bar{\beta}_3 = 2.4 \times 10^{-3}$ . Although numerical simulations reported in this paper include the group-velocity dispersion, it does not appear to have a strong influence on the outcome, and we have observed similar results in considering the above values for  $\bar{\beta}_i$  as when  $\bar{\beta}_i = 0$  for all waves.

Fig. 6.2 shows the measured and calculated signal spectra for different values of the wavevector mismatch, changed by tuning the wavelength of the input signal. (The pump spectrum was measured to be less than 0.2 nm in bandwidth under all experimental conditions. The numerical model demonstrates similarly narrow pump bandwidth, with a maximum observed bandwidth of 0.3 nm, even under conditions for which the signal spectrum is dominated by noise.) Qualitatively, there are many similarities between the measured and calculated spectra; most notably, the presence of broadband radiation at longer wavelengths than the input seed. In addition, the amplitude of this broadband feature decreases with increasing  $\Delta k$  (longer seed wavelength) for both calculated and measured spectra. While absolute agreement between these spectra is not perfect (e.g. the substantially larger noise bandwidth in numerical

simulation), there are many conclusions that may be drawn by examining the trends in how these spectra change as the wavevector mismatch changes, and in correlating changes in the output spectrum with changes in soliton excitation efficiency. Such trends demonstrate the predictive ability of our simple numerical model.

The presence of broadband noise shown in Fig. 6.2 is correlated with poor spatial confinement, in contrast to the noiseless model which predicted the excitation efficiency of quadratic solitons excited with a strong pump and weak signal should increase slightly for  $\Delta k < 0$ [87]. In our experiments, we not only observe pronounced growth of broadband noise in this region, but also reduced spatial confinement of quadratic solitons under these conditions, as shown in the spatial mode profiles in Fig. 6.3. Images of the spatial modes at the exit face of the PPLN crystal at 1550 nm ( $\Delta k Z_R = -2$ ) show a weakly confined signal, and virtually no confinement for the pump wave as compared to solitons launched at 1555 nm ( $\Delta k = 0$ ) and 1560 nm ( $\Delta k Z_R = 2$ ). This behavior is similar to the “red soliton” behavior discussed in Ref. [103], where the temporal breakup of spatial solitons excited by the spontaneous parametric amplification was shown. Although the nature of parametric noise allows for the amplification of sharply peaked temporal pulses, this is different than the formation of temporal or spatio-temporal solitons which require small group-velocity mismatch, or which exist in very specific spectral locations of the dispersion curve for a particular material[85, 109, 110, 111]. In contrast, the growth of parametric noise in the presence of a strong pump wave is fairly general[112].

Spatial noise has no apparent effect on the simulated propagation of these waves, and spatial frequencies in the sampled spatial-frequency bandwidth limited by our sampling density of approximately 8 points per beam radius  $r_0$  were not amplified; i.e., the propagating wave fractured in time rather than in space. Although the circular symmetry assumed in our calculation may not allow for spatial breakup commonly seen in soliton experiments well above the soliton threshold[88], we note that near the soliton threshold we do not expect spatial modulational instabilities with spatial noise features of a size equal to  $\Delta x/r_0 \ll 1$ . To simulate behavior far above the soliton threshold, circular symmetry should not be assumed, and increased sampling density in the spatial domain may be necessary to observe spatial modulational instability

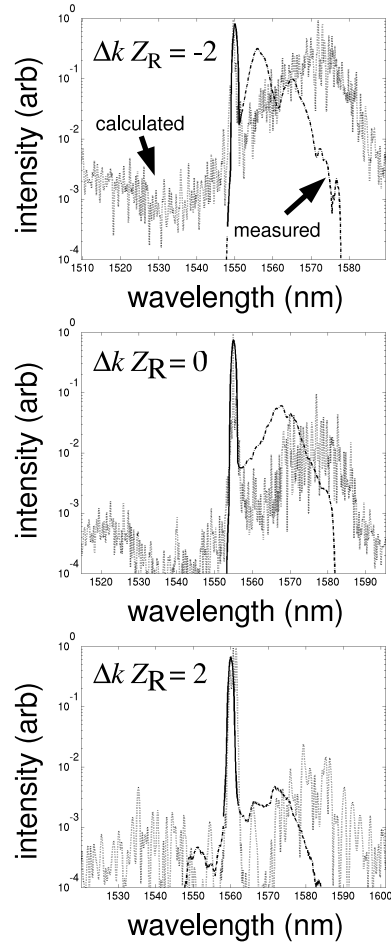


Figure 6.2: Measured and calculated spectra of the signal wave at the exit of a soliton parametric amplifier. The dotted line is calculated using our quasi-(3+1)-D model, and the solid-dashed line is the spectrum of the output signal. The dashed portion, of the measured curve, which lies outside of a 2-nm-wide window around the signal wavelength, is designated “noise”. The striking feature is the broadband spectral content at wavelengths longer than the signal seed wavelength, and the reduction in this spectral content as the seed wavelength is increased (increasing  $\Delta k$ ).

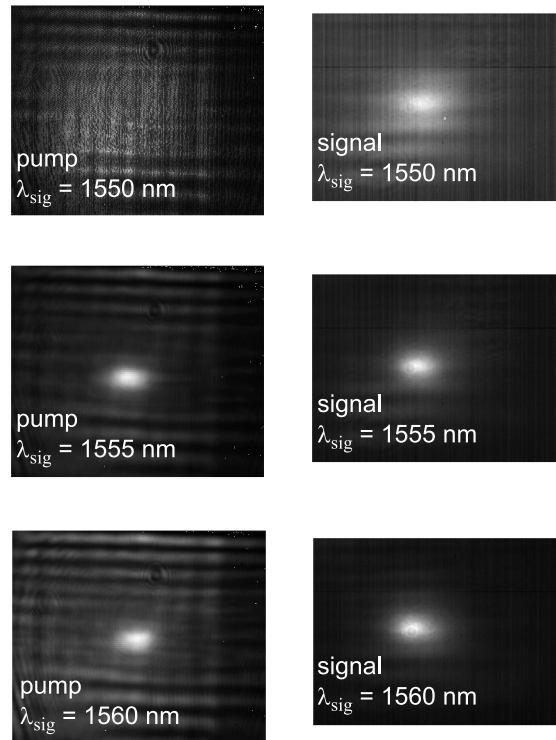


Figure 6.3: Spatial mode profiles for OPA soliton experiments at various signal wavelengths. The normalized wavevector mismatch, from top to bottom, is  $\Delta k Z_R = -2, 0,$  and  $2,$  respectively. Note the poor signal confinement and negligible pump confinement of the measured fluence profiles when the signal wavelength is  $1550$  nm. These images were captured at a pump energy of  $21 \mu\text{J},$  approximately  $1.3$  times the soliton threshold at  $\Delta k = 0.$

at high spatial frequencies.

To quantify the temporal breakup and subsequent spoiling of spatial confinement as the wavevector mismatch is varied, we measured the soliton excitation efficiency for different values of  $\Delta k$ . Simultaneously, we measured the signal spectrum and computed the noise content, defined as the fraction of total signal spectral energy measured more than 1 nm from the seed signal wavelength. Similarly, we define soliton content as the fraction of incident radiation that passes through an aperture placed in the image plane of the exit face of the PPLN crystal. The width of the aperture is approximately 1 mm in comparison to the magnified  $1/e^2$  intensity diameter of the output solitons of 880  $\mu\text{m}$  as measured in the image plane (magnified  $16\times$ ). Computation of the analogous numerical quantities were carried out from the numerical beam-propagation simulations so that a direct comparison could be made between the numerical model and experiment[113, 87]. Although our measurement and calculation of soliton content as described above does not necessarily indicate that light passing through this aperture is confined in a spatial soliton, it affords a direct comparison with our detection scheme. Since under linear propagation the light passing through this aperture would be a small fraction of the incident radiation, this method is a good indicator of nonlinear beam confinement.

The results of these measurements are shown in Fig. 6.4, which demonstrates agreement between measured and calculated excitation efficiency, and a marked departure from simulations calculated without parametric noise. These experiments were repeated for chirped QPM gratings, all with  $\Delta k = 0$  at the input of the PPLN crystal but with differing values of  $\Delta k$  at the output.

Similar agreement is found in chirped gratings (initial  $\Delta k = 0$  for all gratings) as in uniform QPM grating case, as shown in Fig. 6.5. In Chapter 5 we discussed results on chirped gratings in which the excitation efficiency was also observed to decrease slightly with decreasing final wavevector mismatch. Parametric noise was reported to overwhelm the input signal when the existence boundary ( $\Delta k Z_R \approx -2.5$ ) was reached, and parametric noise with an amplitude more than 10 dB below the seed signal level was thought to be insignificant. In this chapter, a more detailed study of the energy in the parametric noise signal reveals that although the spectral

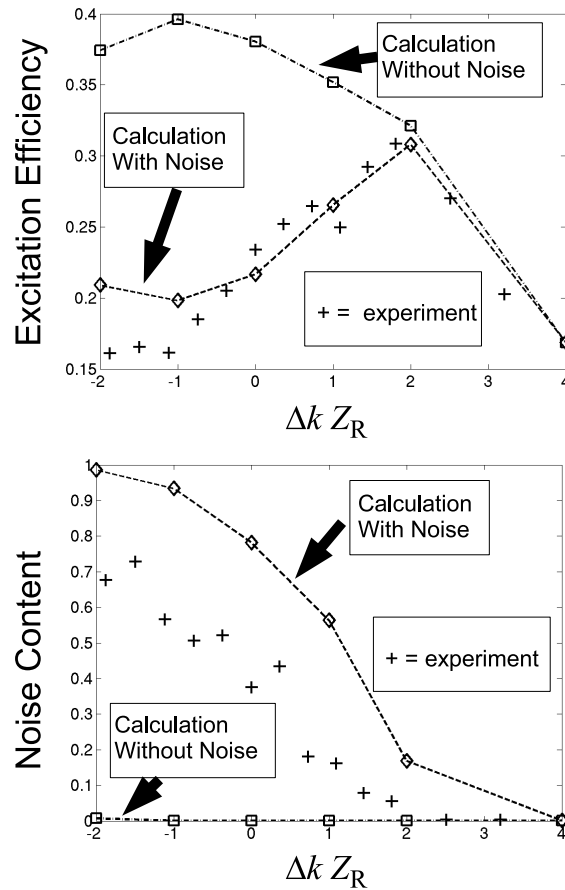


Figure 6.4: Measured & calculated excitation efficiency (top) and fractional noise content (bottom, defined as the spectral energy outside a 2-nm-wide window around the input signal wavelength), for OPA solitons excited in uniform QPM gratings versus the wavevector mismatch. Poor excitation efficiency is correlated with a substantial amount of parametric noise, and demonstrates a marked departure from the noiseless model.

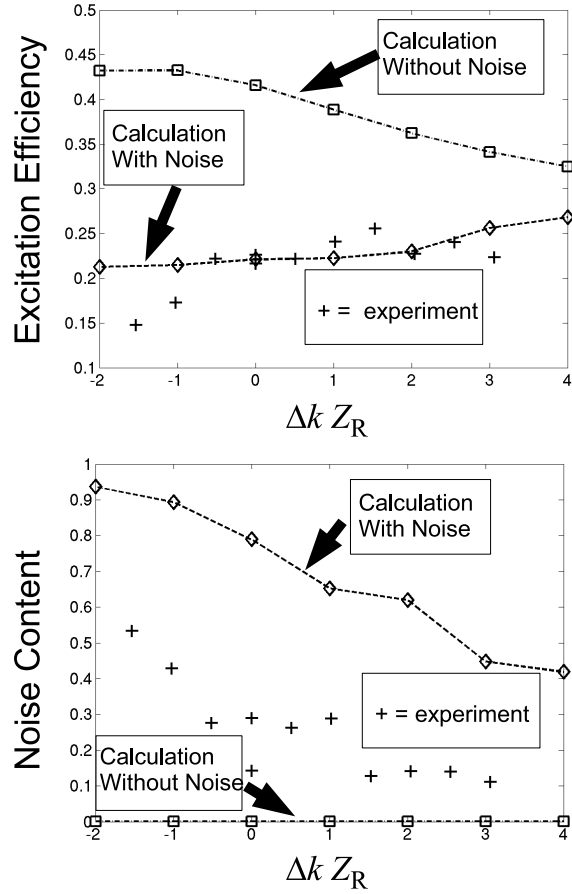


Figure 6.5: Measured excitation efficiency (top) and noise content (bottom) for OPA solitons excited in chirped QPM gratings versus the wavevector mismatch at the output of the QPM device. For these measurements,  $\Delta k = 0$  at the input of each PPLN device. Different chirped PPLN gratings were used with a fixed signal wavelength of 1555 nm.

intensity of parametric noise may be small compared with that of the seed signal, the effects of the growth of broadband parametric noise is likely the dominant factor in the observation of soliton excitation efficiency far below the value estimated by the noiseless model.

## 6.5 Scaling of noise-influenced soliton behavior with signal power

In the above experiments, solitons were excited in a high gain parametric amplifier such that the input signal power of 3 mW was more than 60 dB below the input pump power. The equivalent noise input power, as given by Eq. (6.10), in this experiment is estimated at 1.3  $\mu$ W. It is reasonable to assume that with increased signal power we might observe increased excitation efficiency and suppression of parametric noise. Using an erbium-doped fiber amplifier, we increased the launched signal power to 100 mW. A narrow-band tunable filter (3 dB bandwidth = 1 nm) was used to suppress broadband amplified spontaneous emission (ASE) noise from inside the fiber amplifier; and variable attenuation was used to reduce the signal power level while maintaining a constant level of saturation in the fiber amplifier. The ASE noise was measured to be more than 40 dB below the amplified signal. Soliton excitation efficiency and the noise content were measured as in the above experiments, and we once again compare with numerical simulation. This data is shown in Fig. 6.6. While there are quantitative differences between experiment and theory, the qualitative trends are clear: increased input signal results in an increase in the excitation efficiency, and a decrease in the noise content. Signals at  $\Delta k > 0$  tend to have less noise content than those at negative values of wavevector mismatch.

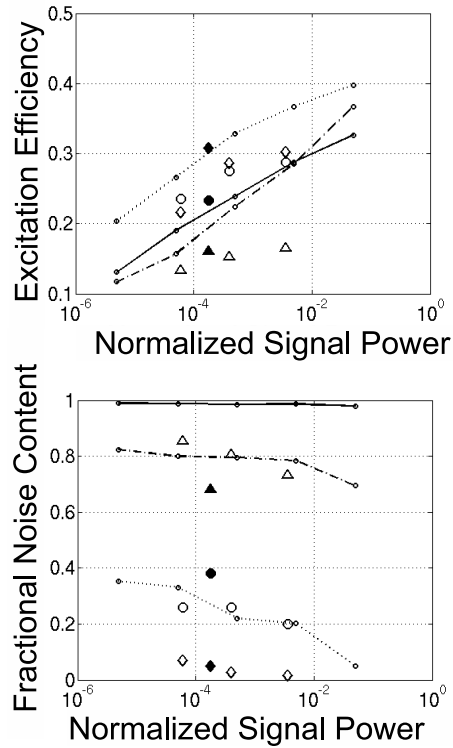


Figure 6.6: Dependence of excitation efficiency and noise content on input signal power. The lines represent the results of numerical simulation; solid lines for  $\Delta k Z_R = -2$ , dashed lines for  $\Delta k = 0$ , and dotted lines for  $\Delta k Z_R = 2$ . Measured data is represented by symbols; filled symbols represent experiments seeded by laser alone (no fiber amplifier), and open symbols represent data taken with the use of a fiber amplifier. Data taken at a seed signal wavelength of 1550 nm ( $\Delta k Z_R = -2$ ) is shown with triangles, at 1555 nm ( $\Delta k = 0$ ) with circles, and at 1560 nm ( $\Delta k Z_R = 2$ ) with diamonds.

## 6.6 Propagation of spatial solitons in the presence of noise

It is tempting, owing to the scaling with signal power in Section 6.5, to conclude that if we can excite solitons with enough signal power, that they will propagate robustly in the presence of parametric noise. To test this assertion, we performed a numerical simulation where we excite with high efficiency spatial solitons that have a temporal envelope. The field envelopes launched in this simulation consist of the stationary state radial envelopes  $a_i^0(r/r_0)$  multiplied by a super-Gaussian temporal envelope function:

$$a_i(\rho, \tau) = a_i^0(\rho) \exp\left(-[2\tau/\tau_p]^{2m}\right), \quad (6.11)$$

where  $m$  is the super-Gaussian order (we use  $m = 5$ ). The normalized time delay  $\tau$  is the same as used in Eqs. (6.1) through (6.2), such that the field-amplitude full-width pulse duration is  $\tau_p$ , which we choose to be equal to 100, the same as the normalized pulse duration used in Section 6.4. A super-Gaussian temporal envelope was chosen so that the temporal window of our calculation is restricted, but the field envelope goes smoothly to zero, thereby mitigating the effects of large field gradients and high frequencies associated with discontinuous field envelopes and finite sampling windows. This particular choice for a temporal envelope results in approximately flat temporal field envelopes with amplitudes equal to the ideal CW soliton field envelopes. The GVM and GVD coefficients used for these calculations are the same as those discussed in Section 6.4.

The pump, signal, and idler spatio-temporal field envelopes are launched with zero relative phase and propagated numerically using Eqs. (6.1) through (6.3). We choose the solutions  $a_i^0(\rho)$  that apply to the family of solitons which have equal numbers of signal and idler photons. Since the choice of input field is not matched to a spatial soliton at values of time delay near the pulse edges ( $|\tau| \approx \tau_p/2$ ), we expect a small amount of power to be radiated on propagation. This behavior does not depend strongly on parametric noise. In addition, we expect a small amount of spectral

broadening, even in the absence of parametric noise, owing to nonlinear phase shifts that apply along the temporal envelope of the interacting fields as a result of their cascaded nonlinear interaction.

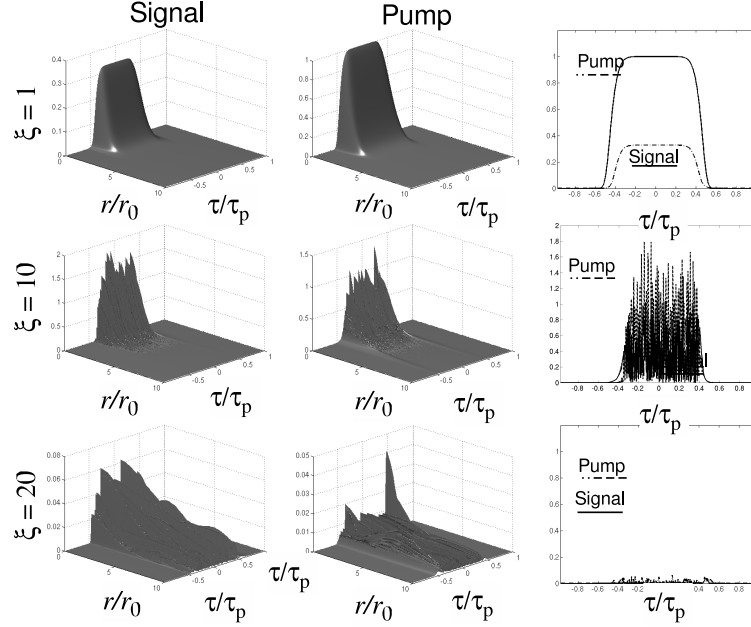


Figure 6.7: Propagation of near-stationary state fields at  $\Delta k = -2$  in the presence of parametric noise with an average input energy density  $\approx 90$  dB below the average energy density of the time-averaged soliton state. Surface plots show the spatio-temporal intensity profile of signal (left) and pump (center) fields. At right is the temporal intensity at beam center  $r = 0$ . Each row shows the field properties after propagation over 1 (top), 10 (middle), and 20 (bottom) diffraction lengths. The growth of parametric noise is concurrent with reduced spatial confinement.

Parametric noise used in these calculations has an average energy density approximately 90 dB lower than the average energy density of that contained in the sum total of pump, signal, and idler. This noise level may be compared to the equivalent noise power ( $\approx 1 \mu\text{W}$ ) for solitons in our experimental geometry ( $r_0 = 20 \mu\text{m}$ , corresponding to a soliton peak power of  $P_{tot} = 6 \text{ kW}$ ). The results of these simulations are shown in Figs. 6.7 and 6.8. In these figures, we plot the spatio-temporal intensity of

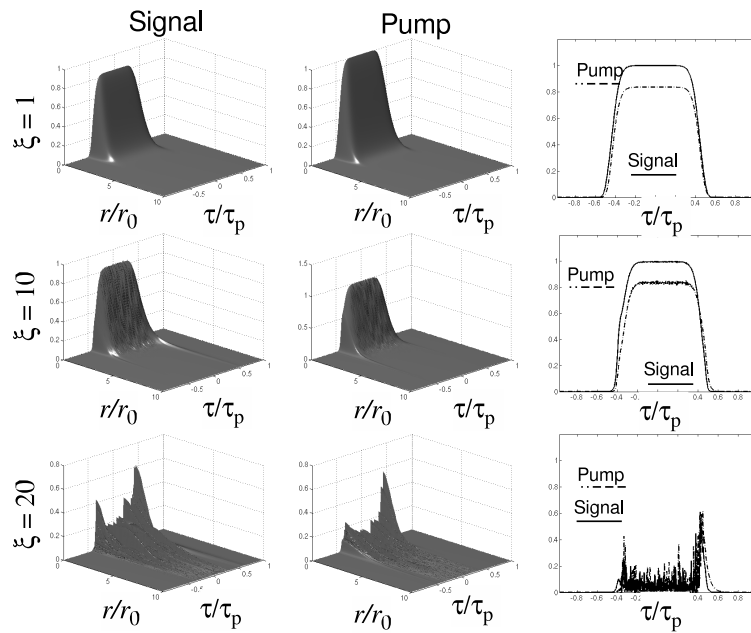


Figure 6.8: Propagation of near-stationary state fields at  $\Delta k = 0$  in the presence of parametric noise with an average input energy density  $\approx 90$  dB below the average energy density of the time-averaged soliton state. Surface plots show the spatio-temporal intensity profile of signal (left) and pump (center) fields. At right is the temporal intensity at beam center  $r = 0$ . Each row shows the field properties after propagation over 1 (top), 10 (middle), and 20 (bottom) diffraction lengths. The growth of parametric noise is substantially slower than in the case shown in Fig. 6.7, and spatial confinement is maintained over more than 10 diffraction lengths.

the pump and signal waves at different propagation distances ( $\xi$ ), as well as the temporal dependence at beam center ( $r = 0$ ). When  $\Delta k Z_R = -2$  (Fig. 6.7), the beam is still spatially confined after 10 diffraction lengths, but amplified noise is already apparent on the temporal envelope. After 15 diffraction lengths, the temporal noise has disrupted the spatial confinement, and energy is radiated away from the beam center. For comparison, Fig. 6.8 shows results for propagation when  $\Delta k Z_R = 0$ . In this case, spatial confinement is maintained over more than 10 diffraction lengths of propagation. At  $\xi = 10$ , noise on the temporal envelope has just barely appeared, but after a longer propagation distance noise appears and again disrupts spatial confinement.

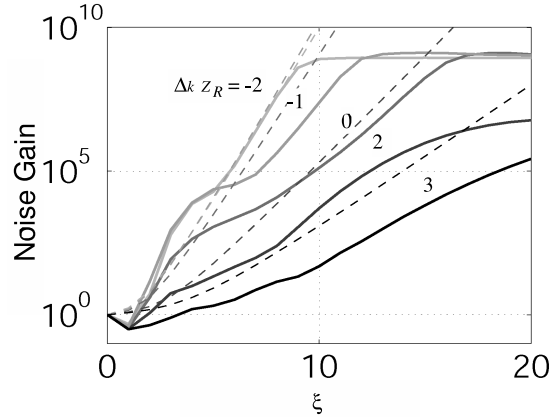


Figure 6.9: Gain of noise content versus normalized distance  $\xi$ . Different curves are shown for different values of the normalized wavevector mismatch, as labeled for solid lines. Dotted lines show the gain predicted by the time-averaged soliton pump field, where the highest gain corresponds to the most negative wavevector mismatch, as predicted by Fig. 2.4.

In Fig. 6.9, we plot the gain of parametric noise, defined as the noise content at  $\xi$  divided by the initial value at  $\xi = 0$ . For all values of  $\Delta k$ , parametric noise grows until it becomes comparable in power to the signal carried in the spatial soliton.

The dashed lines in Fig. 6.9 represent the estimated energy gain. Energy gain for a signal field is estimated by calculating the CW, near-field Gaussian-weighted intensity gain for phase-matched parametric amplification resulting from the input pump field and integrating over all points in space and time. The energy gain is

defined as

$$g(\xi) = \frac{\int_0^\infty \int_{-\infty}^\infty |a_s(\rho, \tau, \xi)|^2 2\pi\rho d\rho d\tau}{\int_0^\infty \int_{-\infty}^\infty |a_s(\rho, \tau, \xi = 0)|^2 2\pi\rho d\rho d\tau}, \quad (6.12)$$

for a small input signal field  $a_s(\rho, \tau, \xi = 0)$ . In the limit of a constant pump field in  $\xi$  with negligible dispersion and diffraction, is given as

$$g(\xi) = \frac{\int_0^\infty \int_{-\infty}^\infty |a_s(\rho, \tau, \xi = 0)|^2 \exp(2\Gamma(\rho, \tau)\xi) 2\pi\rho d\rho d\tau}{\int_0^\infty \int_{-\infty}^\infty |a_s(\rho, \tau, \xi = 0)|^2 2\pi\rho d\rho d\tau}, \quad (6.13)$$

where  $\Gamma(\rho, \tau)$  is the parametric gain coefficient, defined as

$$\Gamma(\rho, \tau) = \sqrt{\frac{|a_3(\rho, \tau)|^2}{\sigma_1\sigma_2}} \quad (6.14)$$

and  $a_3(\rho, \tau)$  is the pump field defined in Eq. (6.11). The estimated gain plotted in Fig. 6.9 (dotted lines) assumes a flat-top input signal field  $a_s(\rho, \tau, \xi = 0)$  with a space-time volume approximately equal to the soliton volume, such that  $a_s(\rho, \tau, \xi = 0) = \epsilon$  for  $r/r_0 < 2$  and  $|\tau/\tau_p| < 1$ , where  $\epsilon$  is a small number. Different curves reflect the different amount of pump energy carried in a spatial soliton at different values of  $\Delta k$  (see Fig. 2.4). Fig. 6.9 shows that this estimate is in excellent agreement with the observed gain of parametric noise when  $\Delta k Z_R = -2$ . For larger (more positive)  $\Delta k$ , the effective gain is reduced from the estimated amount. In Fig. 6.10 we plot the soliton content versus propagation distance.

This graph shows that when parametric noise becomes comparable in energy to the narrowband signal carried in the spatial soliton, spatial confinement is disrupted and energy is radiated away from beam center. This figure shows that we might expect serious disruption of spatial confinement for values of  $\Delta k < 0$  at a maximum propagation distance of  $\xi \approx 10$ . Simulation over long propagation distance (not shown) confirmed that even for  $\Delta k Z_R > 0$ , spatial confinement is not maintained indefinitely and parametric noise simply experiences lower gain at  $\Delta k > 0$ , thereby allowing for longer propagation distances with sustained spatial confinement until parametric noise reaches levels comparable to the soliton power.

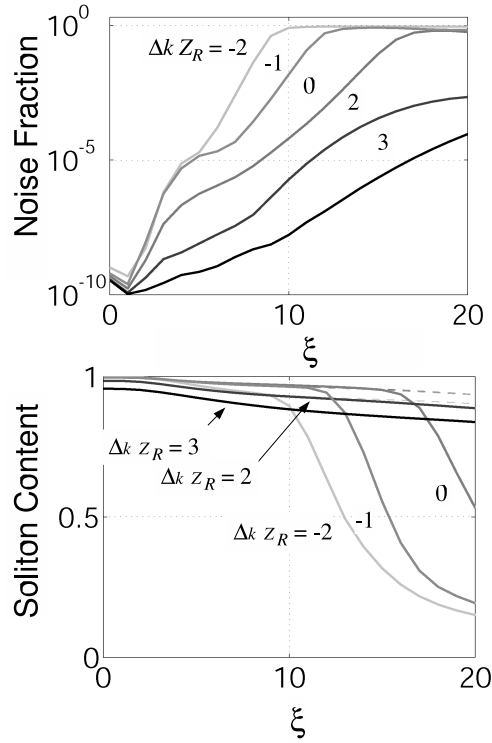


Figure 6.10: Top: Fraction of propagating signal field characterized as noise (total spectral energy more than 2 nm from the narrowband soliton signal) versus propagation distance. Bottom: Soliton content (determined as the fluence passing through an aperture twice the soliton radius) as a function of propagation distance for near-spatial-soliton fields propagating at several values of the wavevector mismatch. Data is shown for  $\Delta k Z_R = -2, -1, 0, 2,$  and  $3$ ; as labeled. Solid lines represent propagation with noise  $\approx 90$  dB reduced from the soliton energy density. Dotted lines represent propagation with no input noise, and are shown for comparison, demonstrating that spoiled spatial confinement in these simulations only occurs in the presence of parametric noise.

The estimated gain in Eq. (6.13) can be used with the parametric noise power in Eq. (6.10) to estimate the length over which quadratic spatial solitons may maintain spatial confinement. For example, the parametric noise power for quadratic solitons with pump and signal wavelengths of 1064 nm and 1550 nm, respectively, was shown to have an equivalent noise power of  $1.6 \mu\text{W}$ . Quadratic solitons with a spot size of  $r_0 = 20 \mu\text{m}$  have a total peak power of approximately 6 kW such that gain of 95 dB is necessary to amplify parametric noise to the level of the soliton power. Fig. 6.9 shows that when  $\Delta k Z_R = -2$ , 90 dB of gain is realized at  $\xi \approx 10$  or 5 cm with  $Z_R = 5$  mm. When  $\Delta k Z_R = 2$ , 90 dB of gain is not realized until  $\xi \approx 16$ , or 8 cm of propagation with  $Z_R = 5$  mm. Similar simulations performed with Gaussian pulses with a time-averaged field amplitude equal to the soliton field amplitude demonstrated faster growth of parametric noise than the super-Gaussian result, indicating that the shape of the temporal envelope may influence the growth of noise.

These simulations indicate that spatial solitons are unstable in the presence of parametric noise, and that the characteristic length for breakup depends on the wavevector mismatch. It is not necessarily surprising that this phenomenon has not been widely observed, as observations of soliton generation are often made in crystals 4-8 times the diffraction length for the low-power input beam size, and soliton behavior is most often demonstrated at phase-matching ( $\Delta k = 0$ ) [89, 84, 90, 91, 92, 85, 93, 94].

## 6.7 Implications for efficiency-enhanced soliton OPA

In Chapter 5 we discussed the idea of using chirped QPM gratings to tailor spatial solitons, thus improving the efficiency of a parametric amplifier. The net efficiency of this device was shown to be limited by low soliton content. In this chapter, experimental and numerical evidence is presented suggesting that the low soliton content reported in Chapter 5 is due to the presence of parametric noise. While Section 6.6 suggests that solitons cannot propagate indefinitely without being influenced by parametric noise, the results presented in Section 6.5 indicate that over limited propagation distances (10 soliton lengths in the reported data), increasing the input signal

level (and correspondingly decreasing the parametric gain) results in increased soliton content.

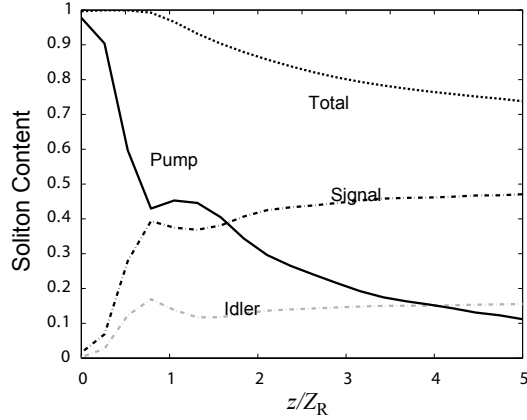


Figure 6.11: Simulation of low-gain, efficiency-enhanced soliton parametric amplifier with low noise. Plotted is the soliton content for each of the component waves as well as the soliton total power versus propagation distance for a representative simulation of a low-gain soliton parametric amplifier. The peak pump power is  $\bar{P}_3 = 440$ , with the normalization of Eq. 2.50. The signal input energy is 20 dB below the pump energy, and the average noise intensity is approximately 50 dB below the peak pump intensity. The chirped QPM grating is chirped from an initial value of  $\Delta k Z_R = -1$  to a final value of  $\Delta k Z_R = 4$ . The remaining simulation parameters (temporal duration, etc.) are identical as for the calculations in Section 6.4. The plot shows that with higher signal input and shorter propagation distance the total soliton content exceeds 70%, and the fraction of the total soliton content in the pump component is approximately 15%, indicating high conversion to signal and idler. These energy numbers improve with flattened temporal envelopes. The measured noise content for this simulation was less than 1%; much less than the noise content for the high-gain results in Fig. 6.5.

Fig. 6.11 shows an example simulation that indicates efficiency-enhanced soliton OPA is still possible in the presence of parametric noise, but may be limited to use in low gain applications (e.g., for use as a power amplifier). Although the utility of this device for simultaneously high-gain and high-efficiency OPA may be limited, the enhanced efficiency may be yet useful in applications for low-gain OPA where efficiency is most important (as compared to a high-gain, low-efficiency pre-amplifier).

Fig. 6.11 shows that injecting more signal power and using a shorter crystal enables 70% soliton content at the output of a chirped grating. Nearly 50% of the total input energy is available as the signal component of the output soliton, as compared with the ideal 68% for 100% soliton content and 100% conversion to signal-idler pairs. A negative wavevector mismatch at the input is used in this calculation to increase the soliton content, as suggested by Ref. [87]. (This technique was tested unsuccessfully in the laboratory in a high-gain amplifier, and is also limited to low-signal-gain applications by the amplification of noise.) The output signal soliton content may be increased with flattened (e.g., super-Gaussian) temporal envelopes, which results in both increased soliton content and increased conversion to signal-idler pairs.

The noise content at the output of this simulation was less than 1% despite the relatively high (50 dB less than the pump input energy) noise input level, indicating that with lower gain and a shorter crystal length, the effects of noise may indeed be suppressed. The plot in Fig. 6.11 represents an example of efficiency-enhanced soliton OPA in the presence of noise, but it may not represent the best achievable performance. Further study would be expected to reveal the design for an optimized soliton parametric amplifier, as well as bounded values of minimum gain and/or maximum interaction length for which QPM soliton tailoring is useful for parametric amplification.

## 6.8 Summary of Chapter 6

In summary, we have discussed the influence of parametric noise in spatial solitons excited in a seeded high-gain parametric amplifier. The presence of parametric noise is observed experimentally as broadband amplified signal light at wavelengths different than the seed signal wavelength. The amplification of noise is shown to have marked differences at positive and negative values of the wavevector mismatch (as defined relative to the seed signal). The amplitude of parametric noise is correlated with poor spatial confinement, departing from the behavior predicted by the noiseless model and influencing the soliton content. The spectral amplitude and bandwidth resulting from

numerical simulations which incorporate parametric noise into a quasi-(3+1)-D model are consistent with experimental observations, and demonstrate a much larger noise component for values of  $\Delta k < 0$  than for  $\Delta k \geq 0$ . Both experimental and numerical evidence in this chapter suggests that the departures from the noiseless model for spatial solitons reported in Chapter 5 may be explained by incorporating parametric noise into the description of soliton excitation and propagation.

Numerical simulations presented in Section 6.6 indicate that even under near-ideal excitation conditions, well matched to the CW spatial soliton solution, noise grows with propagation and eventually spoils the confinement of a well-formed spatial soliton. This is a strong indicator that quadratic spatial solitons have a limited propagation distance over which spatial confinement is maintained in the presence of parametric noise. Although the complicated physics of multi-color spatial solitons in the presence of parametric noise can at present only be fully explained through numerical simulation, simple estimates of parametric noise and gain may be used to predict the growth of parametric noise in a spatial soliton.

This chapter has focused on quadratic spatial solitons in a parametric amplifier in the presence of parametric noise (or spontaneous parametric downconversion). Numerical calculation has been compared to experiment at a pump wavelength of 1064 nm and signal wavelengths near 1550 nm. In PPLN, for these wavelengths, the dispersive effects are dominated by group-velocity mismatch between the signal and the pump waves. Although the bandwidth of parametric generation changes as the magnitude of this group-velocity mismatch parameter changes, the essential physics does not change in the limit that the net amount of temporal walkoff between interacting envelopes is small. This has been confirmed in numerical calculations. However, further study is certainly necessary before the observed physics can be generalized to situations where idler walkoff is important, or group-velocity dispersion plays an important role.

Amplified parametric noise should be expected not only in solitons excited by parametric amplification but in second-harmonic generation as well; and we have observed similar behavior in numerical simulation of SHG interactions. Similarly, experimental SHG data presented in Ref. [103] demonstrates a marked departure

from the noiseless model when  $\Delta k < 0$ , and improved agreement was obtained with a model including time-dependence and parametric noise.

# Chapter 7

## Summary

In this dissertation, we have described quasi-phase-matching as a technology with unique engineering capability, particularly when applied to the frequency conversion of short optical pulses. QPM techniques can be used to engineer the amplitude and phase response of nonlinear materials, and can be used to tailor frequency conversion processes in an effort to maximize efficiency. Chapters 3 through 5 discuss the concept and demonstration of specific examples of QPM engineering when applied to more specific problems in ultrafast nonlinear optics. In this chapter, we review these devices and the associated experiments. Of course, these examples are not an exhaustive list of the potential for QPM device engineering in ultrafast nonlinear optics, and here we also list engineering problems and potential solutions that may build on or supplement the examples in the previous chapters.

### 7.1 Summary of research contributions

In Chapter 3 we discussed the use of lateral and longitudinal patterning to obtain tunable frequency-domain phase response of devices for QPM-SHG pulse compression, as described in Chapter 2, and introduced in Refs. [32] and [49]. Lateral patterning in the form of a fanned QPM grating device demonstrated the capability for compression of FH pulses stretched between 50 and 90 times the transform-limited pulse duration of 140 fs. Not only does this design demonstrate a simple, compact, and monolithic

device for compensation of linear pulse chirp, but a slight modification of this design allows for tunable compensation of nonlinear pulse chirps.

In Chapter 4 we discussed the technique of using spectral angular dispersion to achieve broadband second-harmonic generation in a noncollinear geometry. We discussed experiments in PPLN, where this technique was used to achieve an SHG conversion bandwidth 13.6 times broader than that available in an identical-length crystal using a conventional collinear QPM geometry.

Although this technique has been applied using birefringent phase-matching, QPM engineering is unique in its ability to phase-match the interaction over a variety of chosen angles between the interacting waves. Chapter 4 also presented a rigorous theory for this technique, resulting in solutions for the generated fields at the output of the nonlinear crystal. We applied this theory to derive expressions for the energy conversion efficiency, and found that the conversion efficiency may be optimized through proper choice of the phase-matching angles and focusing conditions. The resulting optimized efficiency is approximately the same as the optimized efficiency when using alternative techniques for ultrafast SHG, and the true advantage of utilizing this geometry lies in the ability to achieve similar conversion efficiency at a reduced peak intensity, thereby reducing the intensity-dependent effects of parasitic nonlinearities and optical damage.

In the future, similar group-velocity mismatch compensation will likely find more useful application in optical parametric amplification. Noncollinear geometries in combination with spectral angular dispersion have already demonstrated increased phase-matching bandwidth [76, 77, 78, 79], but no rigorous theoretical analysis has yet been developed discussing the detailed tradeoffs involved. Such theory may not only allow for optimization of this geometry and focusing conditions, but may also provide more insight into advanced techniques of OPA with multiple beams [114, 115] particularly when applied to engineered QPM superstructures which can be designed with an angular spectrum of Fourier components [18].

In Chapter 5 we discussed the engineering of spatial solitons using chirped QPM structures for enhanced conversion efficiency in a high-gain parametric amplifier.

Chirped-period gratings were used to tailor the fractional power carried in the components (signal, idler, and pump) of multi-color spatial solitons in a parametric amplifier.

Ultimately, we discovered that the utility of this technique in a high-gain system has limitations introduced by the presence of parametric noise, discussed in detail in Chapter 6. In the experiments of Chapter 5, a seed signal approximately 30 dB above the level of equivalent vacuum noise was amplified more than 60 dB to launch a spatial soliton in a chirped-period grating, and limitations due to the effects of amplified quantum noise were observed. With more signal input power, or equivalently, lower parametric gain, it may be possible to find a suitable short-length QPM device that can achieve high conversion efficiency in an interaction shorter than the distance over which noise is amplified to levels comparable with the input pump power.

Perhaps more significant than the impact on the efficiency-enhanced soliton OPA device described in Chapter 5 is the realization that the propagation of spatial solitons may not be completely described by a CW (or noiseless, in the case of pulsed light) model, even though the component pulse envelopes may be much longer than the walkoff time between interacting fields. Experimental and numerical evidence in Chapter 6 indicates that broadband parametric noise grows under a variety of experimental and simulated conditions. The short temporal features characteristic of broadband parametric noise result in temporal walkoff over distances shorter than the soliton length such that propagation in this regime may not be described by a CW model. Spatial confinement predicted by the CW and quasi-CW noiseless models was disrupted for all cases we studied; including OPA and numerical simulation of SHG frequency mixing, as well as simulations using several different values of the group-velocity mismatch parameter which describes the dispersion of nonlinear materials.

Future work may determine more generally the influence of parametric noise, and will likely include theoretical investigations of the stability of spatial solitons in the presence of temporal noise as well as experimental verification of the presence of parametric noise in SHG solitons.

## 7.2 Future Directions

All of the projects in this dissertation have demonstrated the advantages of QPM domain patterning in single-pass frequency conversion experiments. The potential for QPM engineering in cavity-resonant interactions has been comparatively unexplored, although a few key results have demonstrated similar engineering advantages. Femtosecond optical parametric oscillators (OPO's) have been demonstrated previously using QPM crystals [116, 117, 118, 119, 31, 120, 121], and several have utilized aperiodic QPM materials for increased conversion efficiency[122, 123] or dispersion compensation[124]. Noncollinear geometries can be used as well to broaden the bandwidth in a cavity configuration[76], similar in principle to single-pass techniques discussed in Chapter 4.

While we have discussed in this dissertation only the engineering of the *non*-linear properties of nonlinear materials, QPM engineering can be combined with the engineering of linear waveguides in nonlinear materials to produce compact devices with increased conversion efficiency and/or functionality. Waveguide engineering provides for tight confinement of interacting fields over long interaction lengths, enabling extraordinarily high peak conversion efficiency[125]. Strong nonlinear mixing with short pulses has resulted in the measurement of very low threshold parametric generation [126]. When combined with longitudinal QPM patterning to achieve both broad bandwidth and long interaction lengths with tight confinement, PPLN waveguides have been utilized to characterize ultrashort pulses with very low energy corresponding to only a few hundred photons [127].

More sophisticated waveguide structures, including couplers, junctions, and filters, enable more complex engineering solutions. For example, a waveguide approach to group-velocity mismatch compensation has been demonstrated utilizing frequency-selective waveguide couplers to periodically delay a faster field envelope such that it effectively travels through a frequency conversion device with a velocity matched to the slower interacting wave [128]. Waveguide frequency mixers have already demonstrated impressive performance in fast time-division multiplexing [129]. The speed

and functionality in optical signal processing applications resulting from the combination of waveguide and QPM engineering is likely only to improve with time.

# Bibliography

- [1] T. Udem, J. Reichert, R. Holzwarth, and T. W. Hansch, “Absolute Optical Frequency Measurement of the Cesium  $D_1$  line with a mode-locked laser,” *Physical Review Letters* **82**(18), 3568–3571 (1999).
- [2] D. Huang, E. A. Swanson, C. P. Lin, J. S. Schuman, W. G. Stinson, W. Chang, M. R. Hee, T. Flotte, K. Gregory, C. A. Puliafito, and J. G. Fujimoto, “Optical Coherence Tomography,” *Science* **254**, 1178–1181 (1991).
- [3] K. Yamakawa and C. P. J. Barty, “Ultrafast, ultrahigh-peak and high-average power Ti:Sapphire laser system and its applications,” *IEEE J. of Selected Topics in Quantum Electronics* **6**(4), 658–675 (2000).
- [4] S. K. Sundaram and E. Mazur, “Inducing and probing non-thermal transitions in semiconductors using femtosecond laser pulses,” *Nature Materials* **1**, 217–225 (2002).
- [5] U. Keller, “Recent developments in compact ultrafast lasers,” *Nature* **424**, 831–838 (2003).
- [6] P. A. Franken, A. E. Hill, C. W. Peters, and G. Weinreich, “Generation of Optical Harmonics,” *Physical Review Letters* **7**(4), 118–120 (1961).
- [7] J. A. Armstrong, N. Bloembergen, J. Ducuing, and P. S. Pershan, “Interactions between Light Waves in a Nonlinear Dielectric,” *Physical Review* **127**(6), 1918–1939 (1962).

- [8] M. Harada, K. Muramatsu, and S. Kurimura, "Second harmonic generation by quasi-phase matching in 8 mm-long periodically-twinned quartz," in *Conference on Lasers and Electro Optics (San Francisco)*, p. CthKK6 (2004).
- [9] A. Arie, G. Rosenman, V. Mahal, A. Skliar, M. Oron, M. Katz, and D. Eger, "Green and ultraviolet quasi-phase-matched second harmonic generation in bulk periodically-poled KTiOPO<sub>4</sub>," *Optics Communications* **142**, 265–268 (1997).
- [10] H. Karlsson, F. Laurell, P. Henriksson, and G. Arvidsson, "Frequency doubling in periodically poled RbTiOAsO<sub>4</sub>," *Electronics Letters* **32**(6), 556 (1996).
- [11] L. A. Eyres, P. J. Tourreau, T. J. Pinguet, C. B. Ebert, J. S. Harris, M. M. Fejer, L. Becouarn, B. Gerard, and E. Lallier, "All-epitaxial fabrication of thick, orientation-patterned GaAs films for nonlinear optical frequency conversion," *Applied Physics Letters* **79**(7), 904–906 (2001).
- [12] J. P. Meyn, M. E. Klein, D. Woll, R. Wallenstein, and D. Rytz, "Periodically poled potassium niobate for second-harmonic generation at 463 nm," *Optics Letters* **24**(16), 1154–1156 (1999).
- [13] L. E. Myers, G. D. Miller, R. C. Eckardt, M. M. Fejer, R. L. Byer, and W. R. Bosenberg, "Quasi-phase-matched 1.064- $\mu$ m-pumped optical parametric oscillator in bulk periodically poled LiNbO<sub>3</sub>," *Optics Letters* **20**(1), 52–54 (1995).
- [14] M. M. Fejer, G. A. Magel, D. H. Jundt, and R. L. Byer, "Quasi-Phase-Matched Second Harmonic Generation: Tuning and Tolerances," *IEEE Journal of Quantum Electronics* **28**(11), 2631–2654 (1992).
- [15] L. E. Myers, R. C. Eckardt, M. M. Fejer, R. L. Byer, and W. R. Bosenberg, "Multigrating quasi-phase-matched optical parametric oscillator in periodically poled LiNbO<sub>3</sub>," *Optics Letters* **21**(8), 591–593 (1996).
- [16] P. E. Powers, T. J. Kulp, and S. E. Bisson, "Continuous tuning of a continuous-wave periodically poled lithium niobate optical parametric oscillator by use of a fan-out grating design," *Optics Letters* **23**(3), 159–161 (1998).

- [17] J. R. Kurz, A. M. Schober, D. S. Hum, A. J. Saltzman, and M. M. Fejer, “Nonlinear Physical Optics with Transversely Patterned Quasi-Phase-Matching Gratings,” *IEEE Journal of Selected topics in Quantum Electronics* **8**(3), 660–664 (2002).
- [18] V. Berger, “Nonlinear Photonic Crystals,” *Physical Review Letters* **81**(9), 4136–4139 (2000).
- [19] M. A. Arbore, O. Marco, and M. M. Fejer, “Pulse compression during second-harmonic generation in aperiodic quasi-phase-matching gratings,” *Optics Letters* **22**(12), 865–867 (1997).
- [20] P. Loza-Alvarez, D. T. Reid, P. Faller, M. Ebrahimzadeh, W. Sibbett, H. Karlsson, and F. Laurell, “Simultaneous femtosecond-pulse compression and second-harmonic generation in aperiodically poled  $\text{KTiOPO}_4$ ,” *Optics Letters* **24**(15), 1071–1073 (1999).
- [21] M. H. Chou, K. R. Parameswaran, M. M. Fejer, and I. Brener, “Multiple-channel wavelength conversion by use of engineered quasi-phase-matching structures in  $\text{LiNbO}_3$  waveguides,” *Optics Letters* **24**(16), 1157–1159 (1999).
- [22] K. Mizuuchi, K. Yamamoto, M. Kato, and H. Sato, “Broadening of the Phase-Matching Bandwidth in Quasi-Phase-Matched Second-Harmonic Generation,” *IEEE J. Quantum Electronics* **30**(7), 1596–1604 (1994).
- [23] G. Imeshev, M. A. Arbore, M. M. Fejer, A. Galvanauskas, M. Fermann, and D. Harter, “Ultrashort-pulse second-harmonic generation with longitudinally nonuniform quasi-phase-matching gratings: pulse compression and shaping,” *Journal of the Optical Society of America B* **17**(2), 304–318 (2000).
- [24] R. W. Boyd, *Nonlinear Optics* (Academic Press, 1992).
- [25] M. L. Bortz, M. Fujimura, and M. M. Fejer, “Increased acceptance bandwidth for quasi-phaseshifted second harmonic generation in  $\text{LiNbO}_3$  waveguides,” *Electronics Letters* **30**(1), 34–35 (1994).

- [26] S. Ashihara, T. Shimura, and K. Kuroda, “Group-velocity matched second-harmonic generation in tilted quasi-phase-matched gratings,” *Journal of the Optical Society of America B* **20**(5), 853–856 (2003).
- [27] G. Imeshev, M. M. Fejer, A. Galvanauskas, and D. Harter, “Generation of dual-wavelength pulses by frequency doubling with quasi-phase-matching gratings,” *Optics Letters* **26**(5), 268–270 (2001).
- [28] M. A. Arbore, A. Galvanauskas, D. Harter, M. H. Chou, and M. M. Fejer, “Engineerable compression of ultrashort pulses by use of second-harmonic generation in chirped-period-poled lithium niobate,” *Optics Letters* **22**(17), 1341–1343 (1997).
- [29] L. Gallman, G. Steinmeyer, U. Keller, G. Imeshev, and M. M. Fejer, “Generation of sub-6-fs blue pulses by frequency doubling with quasi-phase-matching gratings,” *Optics Letters* **26**(9), 614–616 (2001).
- [30] M. Charbonneau-Lefort, M. M. Fejer, and B. Afeyan, “Tandem chirped quasi-phase-matching grating optical parametric amplifier design for simultaneous group delay and gain control,” *Optics Letters* **30**(6), 634–636 (2005).
- [31] L. Lefort, K. Puech, S. D. Butterworth, Y. P. Svirko, and D. C. Hanna, “Generation of femtosecond pulses from order-of-magnitude pulse compression in a synchronously pumped optical parametric oscillator based on periodically poled lithium niobate,” *Optics Letters* **24**(1), 28–30 (1999).
- [32] G. Imeshev, “Tailoring of ultrafast frequency conversion with quasi-phase-matching gratings,” Ph.D. thesis, Stanford University (2000).
- [33] M. S. Webb, D. Eimerl, and S. P. Velsko, “Wavelength insensitive phase-matched second-harmonic generation in partially deuterated KDP,” *Journal of the Optical Society of America B* **9**(7), 1118–1127 (1992).

- [34] K. Hayata and M. Koshihara, "Group-velocity-matched second-harmonic generation: an efficient scheme for femtosecond ultraviolet pulse generation in periodically domain-inverted beta-BaB<sub>2</sub>O<sub>4</sub>," *Applied Physics Letters* **62**(18), 2188–2190 (1993).
- [35] N. E. Yu, J. H. Ro, M. Cha, S. Kurimura, and T. Taira, "Broadband quasi-phase-matched second-harmonic generation in MgO-doped periodically poled LiNbO<sub>3</sub> at the communications band," *Optics Letters* **26**, 1046–1048 (2002).
- [36] N. E. Yu, S. Kurimura, and K. Kitamura, "Broadband Second Harmonic Generation with Simultaneous Group-Velocity Matching and Quasi-Phase-Matching," *Japanese Journal of Applied Physics* **42**, L821–L823 (2003).
- [37] N. E. Yu, S. Kurimura, K. Kitamura, J. H. Ro, M. Cha, S. Ashihara, T. Shimura, K. Kuroda, and T. Taira, "Efficient frequency doubling of a femtosecond pulse with simultaneous group-velocity matching and quasi phase matching in periodically poled, MgO-doped lithium niobate," *Applied Physics Letters* **82**, 3388–3390 (2003).
- [38] H. Zhu, T. Wang, W. Zheng, P. Yuan, L. Qian, and D. Fan, "Efficient second harmonic generation of femtosecond laser at 1 micron," *Optics Express* **12**(10), 2150–2155 (2004).
- [39] V. D. Volosov, S. G. Karpenko, N. E. Kornienko, and V. L. Strizhevskii, "Method for compensating the phase-matching dispersion in nonlinear optics," *Sov. J. Quantum Electron.* **4**, 1090–1098 (1975).
- [40] V. D. Volosov and E. V. Goryachkina, "Compensation of phase-matching dispersion in generation of nonmonochromatic radiation harmonics. I. Doubling of neodymium-glass radiation frequency under free-oscillation conditions," *Sov. J. Quantum Electron.* **6**, 854–857 (1976).
- [41] S. Saikan, "Automatically tunable second-harmonic generation of dye lasers," *Optics Communications* **18**, 439–443 (1976).

- [42] A. V. Smith, “Group-velocity-matched three-wave mixing in birefringent crystals,” *Optics Letters* **26**, 719–721 (2001).
- [43] T. R. Zhang, H. R. Choo, and M. C. Downer, “Phase and group velocity matching for second harmonic generation of femtosecond pulses,” *Applied Optics* **29**(27), 3927–3933 (1990).
- [44] S. Saikan, D. Ouw, and F. P. Schafer, “Automatic phase-matched frequency-doubling system for the 240–350-nm region,” *Applied Optics* **18**(2), 193–196 (1979).
- [45] B. A. Richman, S. E. Bisson, R. Trebino, M. G. Mitchell, E. Sidick, and A. Jacobson, “Achromatic phase matching for tunable second-harmonic generation by use of a grism,” *Optics Letters* **22**, 1223–1225 (1997).
- [46] G. Szabo and Z. Bor, “Broadband frequency doubler for femtosecond pulses,” *Applied Physics B* **50**, 51–54 (1990).
- [47] P. Baum, S. Lochbrunner, and E. Riedle, “Tunable sub-10-fs ultraviolet pulses generated by achromatic frequency doubling,” *Optics Letters* **29**(14), 1686–1688 (2004).
- [48] M. Aoyama, T. Zhang, M. Tsukakoshi, and K. Yamakawa, “Noncollinear Second-Harmonic Generation with compensation of Phase Mismatch by Controlling Frequency Chirp and Tilted Pulse Fronts of Femtosecond Laser Pulses,” *Japanese Journal of Applied Physics* **39**, 3394–3399 (2000).
- [49] M. A. Arbore, “Generation and manipulation of infrared light using quasi-phases-matched devices: ultrashort-pulse, aperiodic-grating and guided-wave frequency conversion,” Ph.D. thesis, Stanford University (1997).
- [50] A. Dubietis, G. Jonušauskas, and A. Piskarskas, “Powerful femtosecond pulse generation by chirped and stretched pulse parametric amplification in BBO crystal,” *Optics Communications* **88**, 437–440 (1992).

- [51] D. Strickland and G. Mourou, “Compression of amplified chirped optical pulses,” *Optics Communications* **56**, 219–221 (1985).
- [52] R. A. Baumgartner and R. L. Byer, “Optical Parametric Amplification,” *IEEE Journal of Quantum Electronics* **15**(6), 432–444 (1979).
- [53] L. J. Waxer, V. Bagnoud, I. A. Begishev, M. J. Guardalben, J. Puth, and J. D. Zuegel, “High-conversion-efficiency optical parametric chirped-pulse amplification system using spatiotemporally shaped pump pulses,” *Optics Letters* **28**(14), 1245–1247 (2003).
- [54] I. Jovanovic, C. Ebberts, and C. P. J. Barty, “Hybrid chirped-pulse amplification,” *Optics Letters* **27**(18), 1622–1624 (2002).
- [55] I. Jovanovic, B. J. Comaskey, C. A. Ebberts, R. A. Bonner, D. M. Pennington, and E. C. Morse, “Optical Parametric chirped-pulse amplifier as an alternative to Ti:sapphire regenerative amplifiers,” *Applied Optics* **41**(15), 2923–2929 (2002).
- [56] A. Yariv, *Quantum Electronics* (John Wiley and Sons, Inc., 1989).
- [57] G. Imeshev, M. A. Arbore, S. Kasriel, and M. M. Fejer, “Pulse shaping and compression by second-harmonic generation with quasi-phase-matching gratings in the presence of arbitrary dispersion,” *Journal of the Optical Society of America B* **17**(8), 1420–1437 (2000).
- [58] G. Imeshev, M. M. Fejer, A. Galvanauskas, and D. Harter, “Pulse shaping by difference-frequency mixing with quasi-phase-matching gratings,” *Journal of the Optical Society of America B* **18**(4), 534–539 (2001).
- [59] A. V. Buryak, Y. S. Kivshar, and V. V. Steblina, “Self-trapping of light beams and parametric solitons in diffractive quadratic media,” *Physical Review A* **52**(2), 1670–1674 (1995).

- [60] V. V. Steblina, Y. S. Kivshar, M. Lisak, and B. A. Malomed, “Self-guided beams in a diffractive  $\chi^{(2)}$  medium: variational approach,” *Optics Communications* **118**, 345–352 (1995).
- [61] A. V. Buryak, Y. S. Kivshar, and S. Trillo, “Stability of Three-Wave Parametric Solitons in Diffractive Quadratic Media,” *Physical Review Letters* **77**(26), 5210–5213 (1996).
- [62] A. V. Buryak, Y. S. Kivshar, and S. Trillo, “Parametric spatial solitary waves due to type II second-harmonic generation,” *Journal of the Optical Society of America B* **14**(11), 3110 (1997).
- [63] V. M. Agranovich, S. A. Darmanyan, A. M. Kamchatnov, T. A. Leskova, and A. D. Boardman, “Variational approach to solitons in systems with cascaded  $\chi^{(2)}$  nonlinearity,” *Physical Review E* **55**(2), 1894–1898 (1997).
- [64] G. Assanto and G. I. Stegeman, “Simple physics of quadratic solitons,” *Optics Express* **10**, 388–396 (2002).
- [65] A. V. Buryak, P. D. Trapani, D. V. Skryabin, and S. Trillo, “Optical solitons due to quadratic nonlinearities: from basic physics to futuristic applications,” *Physics Reports* **370**, 63–235 (2002).
- [66] P. Loza-Alvarez, M. Ebrahimzadeh, W. Sibbet, D. T. Reid, D. Artigas, and M. Missey, “Femtosecond second-harmonic pulse compression in aperiodically poled lithium niobate: a systematic comparison of experiment and theory,” *Journal of the Optical Society of America B* **18**, 1212–1217 (2001).
- [67] K. Green, A. Galvanauskas, K. K. Wong, and D. Harter, “Cubic-phase mismatch compensation in femtosecond CPA systems using nonlinear-chirp-period poled  $\text{LiNbO}_3$ ,” in *Nonlinear Optics: Materials, Fundamentals and Applications*, pp. 113–115, O. T. Digest (Optical Society of America, Washington DC, 2000).

- [68] S. Russell, M. Missey, P. Powers, and K. Shepler, “Periodically poled lithium niobate with a 20-degree fan angle for continuous OPG tuning,” in *Conference on Lasers and Electro-Optics Technical Digest*, pp. 632–633 (2000).
- [69] E. B. Treacy, “Optical Pulse Compression With Diffraction Gratings,” *IEEE Journal of Quantum Electronics* **5**(9), 454–458 (1969).
- [70] J. D. McMullen, “Analysis of compression of frequency chirped optical pulses by a strongly dispersive grating pair,” *Applied Optics* **18**, 737–741 (1979).
- [71] D. H. Jundt, “Temperature-dependent Sellmeier equation for the index of refraction,  $n_e$ , in congruent lithium niobate,” *Optics Letters* **22**(20), 1553–1555 (1997).
- [72] O. E. Martinez, “Achromatic phase matching for second harmonic generation of femtosecond pulses,” *IEEE Journal of Quantum Electronics* **25**, 2464–2468 (1989).
- [73] S. A. Akhmanov, V. A. Vysloukh, and A. S. Chirkin, *Optics of Femtosecond Laser Pulses* (American Institute of Physics, 1992).
- [74] G. D. Boyd and D. A. Kleinman, “Parametric Interaction of Focused Gaussian Light Beams,” *Journal of Applied Physics* **39**(8), 3597–3639 (1968).
- [75] T. F. Johnson, “Beam Propagation ( $M^2$ ) measurement made as easy as it gets: the four-cuts method,” *Applied Optics* **37**(21), 4840–4850 (1998).
- [76] G. M. Gale, M. Cavallari, T. J. Driscoll, and F. Hache, “Sub-20-fs tunable pulses in the visible from an 82-MHz optical parametric oscillator,” *Optics Letters* **20**(14), 1562–1564 (1995).
- [77] G. M. Gale, F. Hache, and M. Cavallari, “Broad-bandwidth parametric amplification in the visible: femtosecond experiments and simulations,” *IEEE Journal of Selected Topics in Quantum Electronics* **4**(2), 224–229 (1998).

- [78] P. DiTrapani, A. Andreoni, C. Solcia, P. Foggi, R. Danielius, A. Dubietis, and A. Piskarskas, “Matching of group velocities in three-wave parametric interaction with femtosecond pulses and application to traveling-wave generators,” *Journal of the Optical Society of America B* **12**(11), 2237–2244 (1995).
- [79] P. DiTrapani, A. Andreoni, G. P. Banfi, C. Solcia, R. Danielius, A. Piskarskas, P. Foggi, M. Monguzzi, and C. Sozzi, “Group-velocity self-matching of femtosecond pulses in noncollinear parametric generation,” *Physical Review A* **51**(4), 3164–3168 (1995).
- [80] L. Torner, C. B. Clausen, and M. M. Fejer, “Adiabatic shaping of quadratic solitons,” *Optics Letters* **23**(12), 903 (1998).
- [81] S. Carrasco, J. P. Torres, L. Torner, and R. Schiek, “Engineerable generation of quadratic solitons in synthetic phase matching,” *Optics Letters* **25**(17), 1273–1275 (2000).
- [82] R. Schiek, R. Iwanow, T. Pertsch, G. I. Stegeman, G. Schreiber, and W. Sohler, “One-dimensional spatial soliton families in optimally engineered quasi-phase-matched lithium niobate waveguides,” *Optics Letters* **29**(6), 596–598 (2004).
- [83] S. Carrasco-Rodriguez, J. P. Torres, L. Torner, and M. M. Fejer, “Efficiency-enhanced soliton optical parametric amplifier,” *Journal of the Optical Society of America B* **19**(6), 1396–1400 (2002).
- [84] M. T. G. Canva, R. A. Fuerst, S. Babiou, G. I. Stegeman, and G. Assanto, “Quadratic spatial soliton generation by seeded downconversion of a strong harmonic pump beam,” *Optics Letters* **22**(22), 1683–1685 (1997).
- [85] P. DiTrapani, G. Valiulis, W. Chinaglia, and A. Andreoni, “Two-Dimensional Spatial Solitary Waves from Traveling-Wave Parametric Amplification of the Quantum Noise,” *Physical Review Letters* **80**(2), 265–268 (1998).
- [86] A. Galvanauskas, A. Hariharan, F. Raksi, K. K. Wong, D. Harter, G. Imeshev, and M. M. Fejer, “Generation of diffraction-limited femtosecond beams using

- spatially-multimode nanosecond pump sources in parametric chirped pulse amplification systems,” Conference on Lasers and Electro-Optics **CThB 4** (2000).
- [87] S. Carrasco, L. Torner, J. P. Torres, D. Artigas, E. Lopez-Lago, V. Couderc, and A. Barthelemy, “Quadratic Solitons: Existence Versus Excitation,” *IEEE Journal of Selected Topics in Quantum Electronics* **8**(3), 497–505 (2002).
- [88] H. Kim, L. Jankovic, G. Stegeman, S. Carrasco, L. Torner, D. Eger, and M. Katz, “Quadratic spatial solitons in periodically poled  $\text{KTiOPO}_4$ ,” *Optics Letters* **28**(8), 640–642 (2003).
- [89] W. E. Torruellas, Z. Wang, D. J. Hagan, E. W. VanStryland, and G. I. Stegeman, “Observation of Two-Dimensional Spatial Solitary Waves in a Quadratic Medium,” *Physical Review Letters* **74**(25), 5036–5039 (1995).
- [90] R. A. Fuerst, D. M. Babiou, B. Lawrence, W. E. Torruellas, G. I. Stegeman, S. Trillo, and S. Wabnitz, “Spatial Modulational Instability and Multisolitonlike Generation in a Quadratically Nonlinear Optical Medium,” *Physical Review Letters* **78**(14), 2756–2759 (1997).
- [91] R. A. Fuerst, M. T. G. Canva, D. Babiou, and G. I. Stegeman, “Properties of type II quadratic solitons excited by imbalanced fundamental waves,” *Optics Letters* **22**(23), 1748–1750 (1997).
- [92] R. A. Fuerst, M. T. G. Canva, G. I. Stegeman, G. Leo, and G. Assanto, “Robust generation, properties, and potential applications of quadratic spatial solitons generated by optical parametric amplification,” *Optical and Quantum Electronics* **30**, 907–921 (1998).
- [93] B. Bourliaguet, V. Couderc, A. Barthelemy, G. W. Ross, P. G. R. Smith, D. C. Hanna, and C. DeAngelis, “Observation of quadratic spatial solitons in periodically poled lithium niobate,” *Optics Letters* **24**(20), 1410–1412 (1999).
- [94] G. I. Stegeman, L. Jankovic, H. Kim, S. Polyakov, S. Carrasco, L. Torner, C. Bosshard, P. Gunter, M. Katz, and D. Eger, “Generation of, and interactions

- between, quadratic spatial solitons in non-critically-phase-matched crystals,” *Journal of Nonlinear Optical Physics & Materials* **12**(4), 447–466 (2003).
- [95] C. B. Clausen and L. Torner, “Spatial switching of quadratic solitons in engineered quasi-phase-matched structures,” *Optics Letters* **24**(1), 7–9 (1999).
- [96] F. Baronio and C. DeAngelis, “Nonlinear Modes, Resonant Trapping, and Soliton Emission in Engineered PPLN Structures,” *IEEE Journal of Quantum Electronics* **38**(10), 1309–1316 (2002).
- [97] I. V. Shadrivov and A. A. Zharov, “Dynamics of optical spatial solitons near the interface between two quadratically nonlinear media,” *Journal of the Optical Society of America B* **19**(3), 596–602 (2002).
- [98] D. V. Petrov, S. Carrasco, G. Molina-Terriza, and L. Torner, “Deflection of quadratic solitons at edge dislocations,” *Optics Letters* **28**(16), 1439–1441 (2003).
- [99] S. Carrasco, J. P. Torres, D. Artigas, and L. Torner, “Generation of multi-color spatial solitons with pulsed light,” *Optics Communications* **192**, 347–355 (2001).
- [100] M. J. Werner and P. D. Drummond, “Simulton solutions for the parametric amplifier,” *Journal of the Optical Society of America B* **10**(12), 2390–2393 (1993).
- [101] C. R. Menyuk, R. Schiek, and L. Torner, “Solitary waves due to  $\chi^{(2)} : \chi^{(2)}$  cascading,” *Journal of the Optical Society of America B* **11**(12), 2434–2443 (1994).
- [102] E. Lopez-Lago, C. Simons, V. Couderc, A. Barthelemy, D. Artigas, and L. Torner, “Efficiency of quadratic soliton generation,” *Optics Letters* **26**(16), 1277–1279 (2001).
- [103] S. Minardi, J. Yu, G. Blasi, A. Varanavicius, G. Valiulis, A. Berzanskis, A. Piskarskas, and P. DiTrapani, “Red Solitons: Evidence of Spatiotemporal

- Instability in  $\chi^{(2)}$  Spatial Soliton Dynamics,” *Physical Review Letters* **91**(12), 1–4 (2003).
- [104] Y. Guan, J. W. Haus, and P. Powers, “Broadband and off-axis optical parametric generation in periodically poled LiNbO<sub>3</sub>,” *Journal of the Optical Society of America B* **21**(6), 1225–1233 (2004).
- [105] R. L. Byer and S. E. Harris, “Power and Bandwidth of Spontaneous Parametric Emission,” *Physical Review* **168**(3), 1064–1068 (1968).
- [106] H. F. Chou, C. F. Lin, and G. C. Wang, “An Iterative Finite Difference Beam Propagation Method for Modeling Second-Order Nonlinear Effects in Optical Waveguides,” *Journal of Lightwave Technology* **16**(9), 1686–1693 (1998).
- [107] S. Mou, C. F. Lin, and H. F. Chou, “Quasi-3-D Beam-Propagation Method for Modeling Nonlinear Wavelength Conversion,” *Journal of Lightwave Technology* **19**(5), 772–779 (2001).
- [108] L. Jankovic, S. Polyakov, S. Stegeman, S. Carrasco, L. Torner, C. Bosshard, and P. Gunter, “Complex soliton-like pattern generation in Potassium Niobate due to noisy, high intensity, input beams,” *Optics Express* **11**(18), 2206–2210 (2003).
- [109] G. Valiulis, A. Dubietis, R. Danielius, D. Caironi, A. Visconti, and P. DiTrapani, “Temporal solitons in  $\chi^{(2)}$  materials with tilted pulses,” *Journal of the Optical Society of America B* **16**(5), 722–731 (1999).
- [110] X. Liu, L. J. Qian, and F. W. Wise, “Generation of Optical Spatiotemporal Solitons,” *Physical Review Letters* **82**(23), 4631–4634 (1999).
- [111] X. Liu, K. Beckwitt, and F. Wise, “Two-dimensional optical spatiotemporal solitons in quadratic media,” *Physical Review E* **62**(1), 1328–1340 (2000).
- [112] D. A. Kleinman, “Theory of Optical Parametric Noise,” *Physical Review* **174**(3), 1027–1041 (1968).

- [113] L. Torner, J. P. Torres, D. Artigas, D. Mihalache, and D. Mazilu, “Soliton Content with Quadratic Nonlinearities,” *Optics Communications* **164**, 153–159 (1999).
- [114] A. Dubietis, R. Danielius, G. Tamosauskas, and A. Piskarskas, “Combining effect in a multiple-beam-pumped optical parametric amplifier,” *Journal of the Optical Society of America B* (1998).
- [115] E. Zeromskis, A. Dubietis, G. Tamosauskas, and A. Piskarskas, “Gain bandwidth broadening of the continuum-seeded optical parametric amplifier by use of two pump beams,” *Optics Communications* **203**, 435–440 (2002).
- [116] K. C. Burr, C. L. Tang, M. A. Arbore, and M. M. Fejer, “High-repetition-rate femtosecond optical parametric oscillator based on periodically poled lithium niobate,” *Applied Physics Letters* **70**(25), 3341–3343 (1997).
- [117] K. C. Burr, C. L. Tang, M. A. Arbore, and M. M. Fejer, “Broadly tunable mid-infrared femtosecond optical parametric oscillator using all-solid-state-pumped periodically poled lithium niobate,” *Optics Letters* **22**(19), 1458–1460 (1997).
- [118] S. D. Butterworth, P. G. R. Smith, and D. C. Hanna, “Picosecond Ti:Sapphire-pumped optical parametric oscillator based on periodically poled LiNbO<sub>3</sub>,” *Optics Letters* **22**(9), 618–620 (1997).
- [119] T. Kartaloglu, K. G. Koprulu, O. Aytur, M. Sundheimer, and W. Risk, “Femtosecond optical parametric oscillator based on periodically poled KTiOPO<sub>4</sub>,” *Optics Letters* **23**(1), 61–63 (1998).
- [120] Z. E. Penman, C. McGowan, P. Loza-Alvarez, D. T. Reid, M. Ebrahimzadeh, W. Sibbett, and D. H. Jundt, “Femtosecond optical parametric oscillators based on periodically poled lithium niobate,” *Journal of Modern Optics* **45**(6), 1285–1294 (1998).
- [121] D. T. Reid, Z. Penman, M. Ebrahimzadeh, and W. Sibbett, “Broadly tunable infrared femtosecond optical parametric oscillator based on periodically poled RbTiOAsO<sub>4</sub>,” *Optics Letters* **22**(18), 1397–1399 (1997).

- [122] D. Artigas and D. T. Reid, “Efficient femtosecond optical parametric oscillators based on aperiodically poled nonlinear crystals,” *Optics Letters* **27**(10), 851–853 (2002).
- [123] K. A. Tillman, D. T. Reid, D. Artigas, J. Hellstrom, V. Pasiskevicius, and F. Laurell, “Low-threshold femtosecond optical parametric oscillator based on chirped-pulse frequency conversion,” *Optics Letters* **28**(7), 543–545 (2003).
- [124] T. Beddard, M. Ebrahimzadeh, T. D. Reid, and W. Sibbet, “Five-optical-cycle pulse generation in the mid infrared from an optical parametric oscillator based on aperiodically poled lithium niobate,” *Optics Letters* **25**(14), 1052–1054 (2000).
- [125] K. R. Parameswaran, J. R. Kurz, R. V. Roussev, and M. M. Fejer, “Observation of 99% pump depletion in single-pass second-harmonic generation in a periodically poled lithium niobate waveguide,” *Optics Letters* **27**(1), 43–45 (2002).
- [126] X. Xie, A. M. Schober, C. Langrock, R. V. Roussev, J. R. Kurz, and M. M. Fejer, “Picojoule threshold, picosecond optical parametric generation in reverse proton-exchanged lithium niobate waveguides,” *Journal of the Optical Society of America B* **21**(7), 1397–1399 (2004).
- [127] S. D. Yang, A. M. Weiner, K. R. Parameswaran, and M. M. Fejer, “400-photon-per-pulse ultrashort pulse autocorrelation measurement with aperiodically poled lithium niobate waveguides at  $1.55\ \mu\text{m}$ ,” *Optics Letters* **29**(17), 2070–2072 (2004).
- [128] J. Huang, J. Kurz, C. Langrock, A. M. Schober, and M. M. Fejer, “Quasi group-velocity matching using integrated-optic structures,” *Optics Letters* **29**(21), 2482–2484 (2004).
- [129] T. Ohara, H. Takara, I. Shake, K. Mori, S. Kawanishi, S. Mino, T. Yamada, M. Ishii, T. Kitoh, T. Kitagawa, K. R. Parameswaran, and M. M. Fejer, “160 Gbit/s optical-time-division multiplexing with PPLN hybrid integrated planar lightwave circuit,” *IEEE Photonics Technology Letters* **15**(2), 302–304 (2003).